Walther-Meissner
Institut

Bayerische Akademie
der Wissenschaften

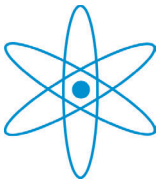

Technische Universität München
Walther-Meissner-Institut
Lehrstuhl für Technische Physik E23
Prof. Dr. Rudolf Gross

Novel ferromagnetic semiconductors: Preparation and characterization of bulk-and thin film samples of Cu-doped ZnO

DIPLOMARBEIT

Amilcar Bedoya Pinto

Table of Contents

Introduction

The future trend in electronics is to exploit the electron spin and introduce new concepts in design and device development. In classical electronics, where only the charge is used, semiconductors have been found to be the most appropriate materials for conduction due to the existance of a bandgap in its electronical structure, which enables to control the charge transport. This technology is now approaching its limits and is unlikely to answer the demands of minaturization and the multifunctional tasks needed in the emerging IT-based technologies. The integrated circuits and the high frecuency devices made of semiconductors, used for information processing, make only use of the charge of the electrons. The storage of information is done by magnetic recording using the electron spin in ferromagnetic materials. But tomorrows infromation technology may see magnetism (spin) and semiconductivity (charge) combined in one device that exploits both charge and spin to process and store the information. This could not be realized so far, because the semiconductors currently used in integrated circuits, transistors and lasers, such as Si or GaAs, are nonmagnetic. Therefore, using the electron spin as an additional degree of freedom will bring advantages in the wide spread existing semiconductor technology.

One of the approaches to drive a semiconductor ferromagnetic is to introduce magnetic ions like Mn, Co and Fe into non-magnetic semiconductors. In these ferromagnetic semiconductors, a part of the lattice consists of substitutional magnetic atoms. Since the typical concentration of the magnetic substituents is low (1-10%), they are called dilute magnetic semiconductors (DMS) [1]. The aim in this emerging spintronic field is to achieve DMS where the electrons have a tunable high grade of spin polarization. Then, a wide field of new electronic devices such as spin valves, transistors, spin light emitting diodes, non-volatile memories and ultra-fast optical switches would be possible. The potential advantages of spintronic devices will be higher speed, greater efficiency, and better stability, in addition to the low energy required to flip a spin [2].

Moreover, it is absolutely necessary for this diverse applications that the DMS show ferromagnetism at room temperature. Following a theroretical prediction by Dietl *et al.*[3], which considers ZnO and GaN as the most promising host semiconductors for

the realization of room-temperature DMS, the quest for the room temperature semiconductor gained momentum. Since then, several researchers have reported observation of room-temperature ferromagnetism in doped semiconductors [4, 5, 6, 7, 8, 9]. A considerable attention has been paid to semiconductors doped with ferromagnetic metals (Co,Fe and Ni). In these type of systems, the fundamental issue of much concern is that the ferromagnetic ordering could be a result of metal clusters or precipitates.

An universal picture regarding the actual mechanism of ferromagnetic ordering in DMS has not been established yet. However, there are currently two models which describe the intrinsic nature of ferromagnetism in DMS. Considering the case of ZnO, which is the material studied in the present work, Dietl *et al*. proposed a model where ferromagnetic ordering is mediated through spin-polarized carriers, and predicting that room-temperature ferromagnetism could be achieved for Mn-doped p-type ZnO [3]. On the other hand, and since the most experimental studies found that doped ZnO was rather n-type (electrons as carriers), Coey *et al*. presented recently a generalized model for n-type oxide based DMS, attributing ferromagnetic ordering to the existence of a donor-derived spin-split impurity band [10]. Both models will be discussed extensively in the next chapter.

As stated before, one of the biggest problems while doping a semiconductor with ferromagnetic metals, is the possible formation of metal clusters, precipitates and secondary magnetic phases. In that case, the origin of ferromagnetism would be unclear, whether coming from the actual inclusion of the magnetic ions in the host lattice, or from the extrinsic sources mentioned above. To avoid controversies from the very beginning, the doping with an element which is not ferromagnetic itself, will be a better choice. A possible candidate could be Cu. As a member of the transition metal group, Cu substitution can be considered as magnetic doping if Cu substitutes Zn^{2+} in the hexagonal structure of ZnO. The electronic structure of Cu^{2+} is $[Ar]3d^9$, which means an unpaired spin in the d-level which could contribute to ferromagnetic ordering. Additional advantages of Cu-doping are, on the one hand, a good solubility in the ZnO host matrix in the dilute level, fact that guarantees a fast and reliable bulk material processing; and the similar atomic radius to the element Zn, which enables the Cu-substitution without a major distortion in the host ZnO hexagonal lattice structure.

The main aim of the present thesis would be to confirm the intrinsic nature of ferromagnetism in DMS, by showing that ferromagnetic ordering in Cu-doped ZnO is indeed possible. Both bulk materials and thin films will be prepared and characterized for this purpose. The challenge is to find out if and under which conditions room-temperature ferromagnetism may arise in the studied system.

1. Dilute Magnetic Semiconductors

Recent work in spintronics focuses on achieving practical ferromagnetic ordering temperatures ($\geq$300K) in technologically useful semiconductors. While the progress in synthesizing and controlling magnetic properties of III-arsenide semiconductors (GaAs, InAs) has been astonishing, the reported ferromagnetic transition temperatures (known as Curie-Temperature T_c) are still too low ($\approx$172 K) to have a significant practical impact.

A key theoretical development that focused on wide gap semiconductors, as being the most promising for achieving high Curie-temperatures, was the work of Dietl *et al* [3].They employed the Zener model of ferromagnetism to predict T_c values for several semiconductors doped with transition metals such as Co,Mn or Fe, denoted as dilute magnetic semiconductors (DMS).

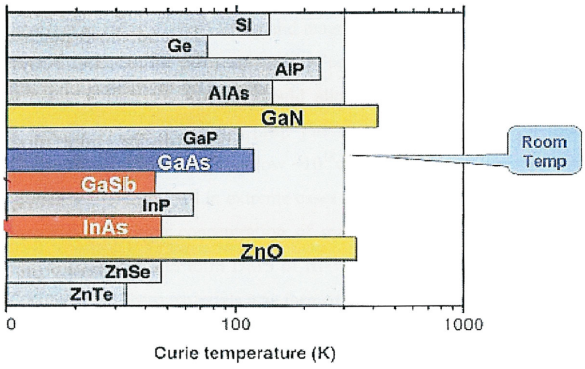

Figure 1.1: Predicted T_c for several dilute magnetic semiconductors, taken from [3].

This prediction initiated intense research to realize a room temperature DMS based on wide band gap semiconductors. Tremendous progress has been made since then both in the realization of high quality epitaxial films and in the theory of ferromagnetism in DMS.

In this chapter, the physical properties of semiconductors, focusing on ZnO as a specific member of the oxide semiconductor group, as well as the mechanisms of ferromagnetism applicable to DMS will be described, in order to be able to understand

and interpret the experimental results presented in Chapter 4.

1.1 Semiconductors

1.1.1 Elementary properties

In many textbooks on solid-state physics, a semiconductor is usually defined rather loosely as a material with electrical resistivity lying in the range of 10^{-2} - $10^{9}\Omega$cm, precisely between metals and insulators. But it is not only a matter of numbers: the most significant characteristic of semiconductors is the existence of a considerable energy gap (eV-range) in its electronical structure and its strongly temperature-dependent conductivity. At the absolute zero, it is an insulator, while the conductivity increases with increasing temperature, in contrast to metals.
According to the band structure theory of solids [11], the interaction of the electrons with the crystal atoms is taken into account, namely with the periodic potential V_{atom} in the hamiltonian

$$H = \frac{\hbar^2 k^2}{2m} + V_{atom} \tag{1.1}$$

The solution of the Schrodinger-equation for an electron wavefunction considering the hamiltonian presented in eq.(1.1), will lead to a quantization of energy states, and the type of crystal potential (either for nearly-free or tight-bound electrons) will define the exact shape of the band structure [12]. The quantized electron energy states are filled up to the so called Fermi-level or Fermi-energy (E_F).

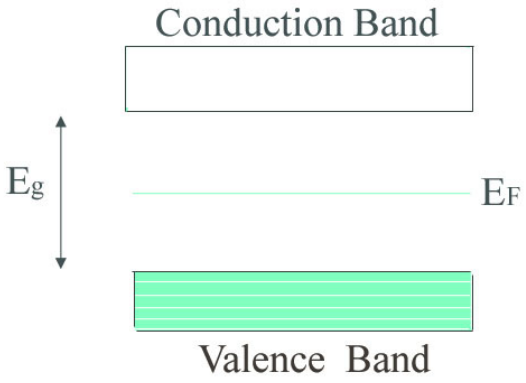

Figure 1.2: Usual representation of the band structure in semiconductors, showing the filled valence band and the empty conduction band. The Fermi-level lies close to the middle of the energy gap in the case of *intrinsic* (pure) semiconductors.

In semiconductors, at T=0K, all the filled energy states up to E_F are seen as a whole band, which is called the valence band. The first empty energy state beyond E_F and all the successive unoccupied states form the conduction band. Between the last filled state and the first empty state, there is a significant energy difference: there is a so called „energy gap“ between valence and conduction band, with the Fermi-level residing in the gap (see Fig.1.2). Impurities present in the crystal, however, may introduce energy levels which do not belong neither to the valence nor to the conduction band, and since the Fermi level has to lie upon the last filled state, it will be shifted. This phenomena will be discussed later on.
In metals, on the other hand, the Fermi-level lies in the conduction band, which means that there are populated and unpopulated energy states within the same band. The electrons are able to contribute to electrical transport, without having to overcome an energy gap like in semiconductors. The position of the Fermi-level determines the transport properties of crystalline solids: in the case of metals, is the responsible for their good conductivity. This band stucture model is therefore useful to provide a deeper insight in the mechanism of conduction in solids.
Considering semiconductors at low temperatures ($\rightarrow 0K$), they become insulators, since it is impossible for the electrons in the valence band to „jump“ to the conduction band, due to the lack of thermal energy. By increasing the temperature, more and more electrons will be thermally activated and overcome the energy gap. Each electron which is excited from the valence band to the conduction band, will leave a *hole* in the valence band. In the semiconductor language, a *hole* is a pseudo-particle which represents the absence of an electron, and it carries a positive charge.

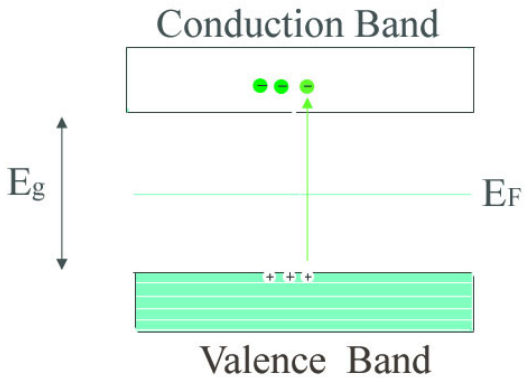

Figure 1.3: Thermal activation of electrons. Each electron will leave a *hole* in the valence band.

In the case of a pure semiconductor, which means a perfect crystal lattice structure without defects (e.g atomic vacancies) and the absence of atomic impurities diffused

in the structure, there will be no other energy states apart from the ones in valence- and conduction band, and the Fermi-level will be located close to the middle of the band gap. In this case, the semiconductor is called *intrinsic*, with the particular relation

$$n = p \tag{1.2}$$

where n represent the electron concentration in the conduction band and p the analogue hole concentration in the valence band. In real cases, however, the semiconductors are not perfect crystallined solids, or there are intentional or unintentional introduced impurities present in their structure. The defects or impurities act as scattering centers, scattering the free electrons because they may break the periodicity of the crystal potential, especially if they are not substituing the host atoms in the lattice. This kind of impurities are also called *interstitials*, because they lie between the atoms of the host structure. In addition, impurities and defects play the essential role of modyfing the electron concentration in semiconductors and hence the electrical transport, especially in the case of intentionally introduce impurity atoms, known as *doping* (see next section). If the impurity atoms have approximately the same size as the ones from the host structure, it is very likely that a replacement takes place instead (*substitutional* impurities).

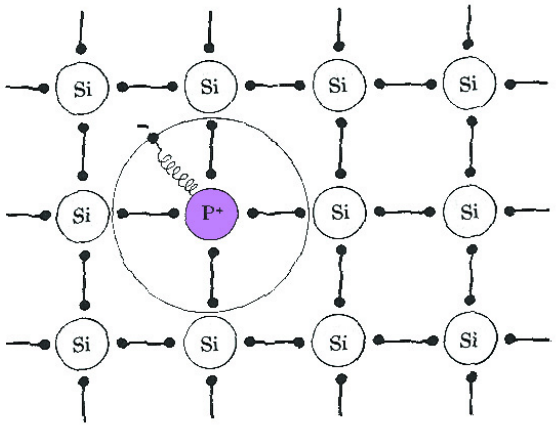

Figure 1.4: An example of a phosphorus atom as a substitutional impurity in a silicon lattice. It provides the system with an additional electron: phosphorous plays the role of a *donor*.

Depending on the valence of the substituent, either an excess, or a deficiency of electrons (holes) will be induced in the system. Atoms which can give an extra electron to the crystal on ionization are called *donors*; if they provide rather holes they are called *acceptors*. These additional electrons (or holes) which are still bound to its

atom orbit, could be also driven into the conduction band, thus influencing the electron (hole) concentration. The energy needed to unbind an electron from impurity atoms in a semiconductor and bring it to the conduction band, varies in the range of 1-100 meV [13]. According to this energy, the impurity atoms are classified into *shallow* and *deep* donors, indicating the position of their energy states relative to the conduction band. The same terminology applies to acceptors. If the -intentionally or unintentionally- introduced impurities or crystal defects are donors, the semiconductor is called $n-doped$, while a $p-doped$ semiconductor has acceptors instead. This notation is mainly used when evaluating the electrical transport properties of semiconductors (Section 1.1.2): a n-doped semiconductor implies that electrons are the majority carriers in the system, while *holes* mediate carrier transport in the case of p-doping.

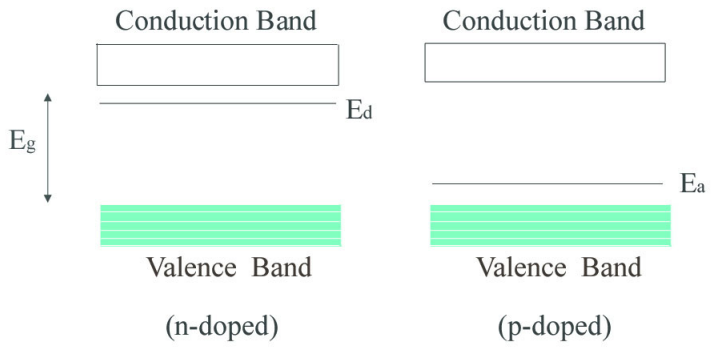

Figure 1.5: Bandstructure of n- and p-doped semiconductors. The donor level E_d lies close to the lower edge of the conduction band, while the acceptor level E_a lies close to the upper edge of the valence band.

Substitutional impurities, donors or acceptors, when diluted within the semiconductor lattice, give rise to discrete energy levels within the bandgap. But if the concentration of carriers (e.g donors) becomes large enough in real space for their orbits to interact, the electrons from the donors will be delocalized within the crystal. The crystal is then a conductor at any temperature, and an insulator-metal transition is thus observed as a function of concentration. In the case of silicon, the most studied semiconductor, this transition is observed at $N_{donor} \geq 3,7 \cdot 10^{24} m^{-3}$. Above this critical carrier concentration, the presence of many donors leads to a broadening of the level E_d, which is no longer separated from the conduction band, the delocalized donors form an „impurity band“.
Since the temperature dependence of the conductivity is one of the most characteristic

features of semiconductors, a detailed description will be given in the next section.

1.1.2 Transport phenomena in intrinsic and doped semiconductors

Knowing the band structure of semiconductors, at least in the region close to the band gap, as well as the localized quantum states caused by the presence of shallow impurities, the calculation of the electrical conductivity of the semiconductor now requires to find the number of mobile charges (electrons or holes) and their nature, at thermal equilibrium. For this purpose, the calculation of the occupation probabilities of the accessible energy levels are needed. The electrons have spin-1/2 and are fermions, therefore the system state only contains one electron per single-particle quantum state. For a given wave vector, there are two quantum states with different spins which can be occupied simultaneously (up- and down spin). Thus, the most appropriate statistical distribution to describe the occupation probability of electrons for a given energy state E will be

$$f_e = \frac{1}{1 + \exp(\frac{E - E_F}{k_B T})} \tag{1.3}$$

known as the Fermi-Dirac distribution, where E_F denotes the Fermi-energy and k_B the Boltzmann constant. Analogue, the probability of occupation by a hole is

$$f_h = 1 - f_e = \frac{1}{1 + \exp(\frac{E_F - E}{k_B T})} \tag{1.4}$$

The carrier density of states (n) gives the population of carriers at a particular energy. For example, n_c will be the density of states of electrons at the conduction band, which are able to contribute to electrical transport. According to the band structure model, if the constant energy surfaces are spheres, and if there is only one energy minimum at the vicinity of the band-gap, the value of $n_c(E)$ for the two spin orientations and unit volume is given by

$$n_c(E) = 4\pi(2m_e^*)^{3/2}(1/h^3)(E - E_c)^{1/2} \tag{1.5}$$

being E_c the energy at the conduction band border, m_e^* the effective electron mass and h the planck constant. Combining population number and occupation probability of carriers, it is possible to calculate the real electron number at a given energy E. The number of electrons n in the conduction band, is therefore

$$n = \int_{CB} n_c(E) f(E) dE \tag{1.6}$$

As a solution of the integral, the expression obtained depends mainly on the temperature of the system

$$n(T) = n_0 T^{3/2} \exp(\frac{-(E_c - E_s)}{2k_B T}) \tag{1.7}$$

where E_c is the energy at the conduction band border and E_s could be substituted by E_v (valence band border) in the case of an *intrinsic* and E_d (donor impurity band border) in the case of a $n-doped$ semiconductor. It is worth to mention, however, that the constant n_0 in equation (1.7) contains the electron effective mass m_e^*, which considers the influence of the crystal potential on the travelling electron, thus having different values for each semiconductor.
The calculation of the hole carrier concentration in the p-doped case is analogous, taking into consideration the valence band border energy E_v, the acceptor level E_a, and the hole effective mass m_h^* instead.
Another consequence of temperature, when considering n- or p-doped semiconductors, is that the ionization of impurities will come to a saturation. Assuming the simple case of uncompensated n-type semiconductors, which means there are no acceptors which could be potentially ionized ($n_a^- = 0$), electrical neutrality will lead to

$$n + n_a^- = p + n_d^+ \overset{n_a^- = 0}{\longrightarrow} n = p + n_d^+ \tag{1.8}$$

where n_d^+ and n_a^- represent the number of ionized donors/acceptors. After separating ionized donors n_d^+ into total donors N_d minus neutral donors n_d^0, and using the electron occupation probability (1.3) for each case, following relation will remain:

$$(n-p)n = \frac{N_c}{2}(N_d - n + p) \cdot exp(\frac{E_d - E_c}{k_B T}) \tag{1.9}$$

where N_c is equal to the expression

$$n_0 \cdot T^{3/2} = 2(\frac{2\pi m_e^* k_B T}{h^2})^{3/2} \tag{1.10}$$

in equation (1.7), sometimes called the effective or equivalent density of states of the conduction band.
For a good interpretation of equation (1.9) in n-type semiconductors, it is suitable to consider three different temperature ranges:

- (a) At zero temperature is $n = 0$ and $p = 0$, the semiconductor is an insulator. Therefore, the Fermi-level must lie above the donor levels. At very low temperatures the ionization of the donors is weak and the hole concentration is negligible (the Fermi energy is very high in the band). Neglecting n and p compared to the total donor concentration N_d (equation (1.9)) becomes

$$n(T) = (\frac{N_c N_d}{2})^{1/2} \cdot \exp(\frac{E_d - E_c}{2k_B T}) \tag{1.11}$$

The electron number increases, with an activation energy equal to half the binding energy of the donor. The Fermi level still lies between the donor level and the conduction band.

- (b) At intermediate temperatures, the exponential of eq.(1.9) is of order 1 and the hole number is still negligible. The relation (1.9) could be written as

$$(N_d - n) = \frac{2n^2}{N_c \cdot \exp(\frac{E_d - Ec}{k_B T})} \tag{1.12}$$

The density of states of the conduction band $N_c(T) \propto T^{3/2}$ will be much larger than N_d, due to its temperature dependance, so the solution $n = N_d$ (constant function) will be a good approximation. That means, all the donors have been ionized, and we reach the saturation regime. The thermal energy is still too low for activating electrons from the valence band. During the process of saturation, the Fermi-energy will decrease and shift deeper within the band, lying lower than the donor energy level.

- (c) At high temperatures, the intrinsic regime will be recovered, since all the donors have already been ionized, and the thermal energy of the electrons is clearly greater. The electron concentration n will vary then as $\exp(E_g/2k_B T)$, the equation will be analogous as in case (a) but with $\Delta E = E_g$. The Fermi-level will lie in the middle of the band gap.

The effect of temperature on the carrier concentration n_E plays a crucial role for the electrical conductivity of a semiconductor, defined as

$$\sigma = \sigma_e + \sigma_h = n\mu_e e + p\mu_h e \tag{1.13}$$

In this expression, n and p are the electron and hole concentrations, respectively; and $\mu_{e(h)}$ is called the electron (hole) mobility. It is important to determine the majority carriers of the studied system. Since the typical values of the carrier concentration are in the order $\approx 10^{17} - 10^{23}$ for doped semiconductors, the term in the sum where the majority carriers appear will prevail. So we will have three different cases:

- (a) for n-doping:

$$\sigma = n\mu_e e + p\mu_h e \overset{n>>p}{\rightarrow} n\mu_e e \tag{1.14}$$

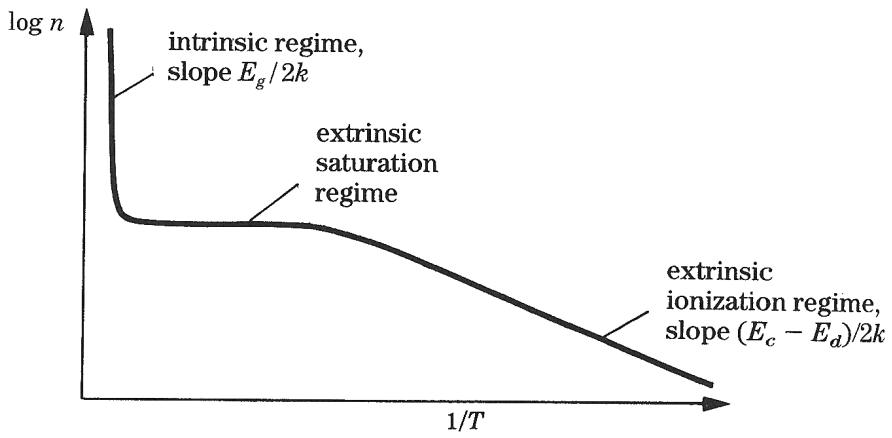

Figure 1.6: Variation of the logarithm of the concentration as a function of the inverse temperature for an n-type semiconductor.

- (b) for p-doping:

$$\sigma = n\mu_e e + p\mu_h e \overset{p>>n}{\rightarrow} p\mu_e e \tag{1.15}$$

- (c) and in the intrinsic case, the relation (1.13) will remain unchanged, due to the equal concentrations of electrons and holes (n=p).

In all the cases, the *mobility* is another parameter which may influence the electrical transport. A good carrier mobility, in common words, could be explained as the capability of carriers to travel from one point to another efficiently, with less collisions or disturbances. To have a deeper look on the role of the *mobility*, the different collision mechanisms of carriers should be considered.

- Scattering by lattice vibrations (subindex:L), also called *phonons*. The amplitude of the vibrations increases with temperature and it is expected that the collision probability also increases with T. As a result, the time τ between two collisions and hence the mobility will decrease with

$$\mu_L \propto \tau \propto T^{-3/2} \tag{1.16}$$

- Collisions with ionized impurities (subindex:I) and the effect of the Coulomb-field. It could be shown that the temperature dependance of the mobility in this case is in the form[13]:

$$\mu_I \propto T^{\frac{3}{2}} \tag{1.17}$$

If the temperature is increased, the motion of the atoms in the crystal will become more rapid and the distance which they move from their central positions becomes greater. In addition to this, the thermal velocity of the electron will increase. These two changes will have opposite effects on τ_I and τ_L. (Note that the time τ between collisions is proportional to the mobility.) The frequency of lattice collisions will clearly increase since the atoms are oscillating more rapidly and sweeping out a greater volume. Due to this fact, τ_L decreases with temperature. On the other hand, the value of τ_I increases with temperature since the greater the thermal energy of the carrier the less it is affected by the deflectic coulombic force of the impurity atom.

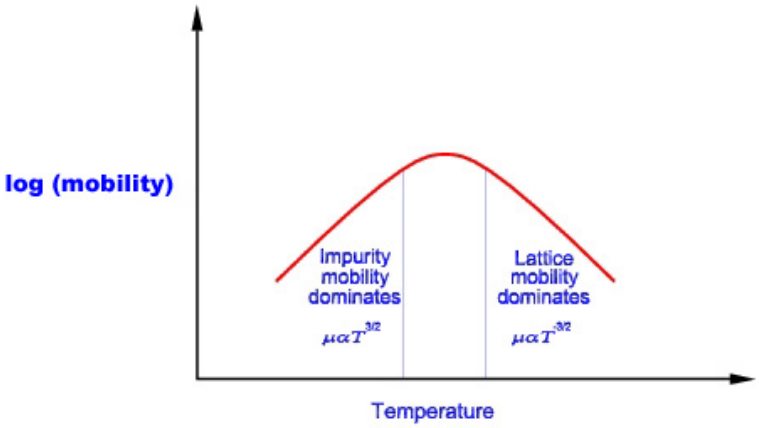

Figure 1.7: Variation of the carrier mobility with temperature.

At low temperatures, μ_{total} is dominated by the impurity component and increases with increasing temperature, until, as temperature rises, lattice collisions become dominant and the mobility will begin to fall again.

As we have summarized the temperature dependences of the mobilities and carrier concentration, it is clear that the mobilities do not have a strong variation with temperature. Hence the variation of σ will be influenced dominantly by the $n(T)$ behaviour, which follows an exponential relation with $\exp(\frac{-\Delta E}{k_B T})$. This explains the very strong increase in conductivity with temperature and provides a method of measuring the energy gaps in semiconductors. In contrast to metals, where the number of carriers is constant, the conductivity of semiconductors increases with temperature mainly through the increased number of carriers.

1.1.3 Hall-Effect in semiconductors

In the presence of a magnetic field, the free carriers which contribute to electrical transport experience a deviation in their trajectory, due to the Lorentz-force

$$\vec{F} = q \cdot \vec{v} \times \vec{B} \tag{1.18}$$

which is maximal when the external magnetic field $\vec{B}$ is applied perpendicular to the carriers' direction of motion (given by the carrier velocity $\vec{v}$) and vanishes when $\vec{B}$ is applied parallel to it. The absolute value of q is the elementary charge $|q| = e = 1,602 \cdot 10^{-19}$ and its sign depends on the type of carrier ((-) for electrons, (+) for holes). If the carrier current is flowing in the x-direction, with a magnetic field applied in z-direction, the Lorentz-force will bend the trayectories of the carriers and thus produce an electrical field in y-direction, called also $Hall\text{-}field$. This phenomena is not as simple as it seems from the first impression, since the carriers will be exposed, during their trayectory, to different collisions mechanisms, described in section 1.1.2. Therefore, a complete description of the kinetics of the electrons (equation of motion) has to be considered.
Assuming that the transport mechanism in a semiconductor is governed by only one type of carriers (e.g electrons), the system can be treated in the one-band model. Considering the linearized Boltzmann equation as the most suitable equation of motion for the description of travelling electrons which are exposed to collisions, in the presence of an electrical field $\vec{E}$ and a magnetic field $\vec{B}$, the following relation will be obtained [14]:

$$\vec{E} = \rho_0 \vec{j} + \frac{e\tau}{m} \rho_0 (\vec{B} \times \vec{j}) \tag{1.19}$$

where $\vec{j}$ represent the current density of the electrons, τ is the time between collisions (see section 1.1.2) and ρ_0 is the resistivity of the semiconductor in the absence of a magnetic field. From eq.(1.19) it can be clearly concluded that the electrical field $\vec{E}$ needed to produce the electron current has to be divided in two components. The one parallel to the magnetic field $\vec{B}$ is given through the relation

$$E_{parallel} = \rho_0 J \tag{1.20}$$

which is equivalent to $\vec{J} = \sigma_0 \vec{E}_{parallel}$, corresponding to Ohms law. In the parallel configuration, the resistivity has not been influenced by the magnetic field, which means that there is no magnetoresistive effect according to this one-band model. In the transversal component, the so-called $Hall\text{-}field$

$$E_H = \frac{e\tau}{m} \rho_0 B J \tag{1.21}$$

there is indeed a change in the resistivity. Comparing eq.(1.21) with Ohms law, the hall resistivity is nothing else but the proportionality factors between E_H and J

$$\rho_{xy} = \frac{E_H}{J} = \frac{e\tau}{m}\rho_0 B \tag{1.22}$$

and, using the definition of the conducitvity in absence of a magnetic field and considering only electrons as carriers, namely $\sigma_0 = \rho^{-1} = \frac{ne^2\tau}{m}$, to eliminate the relaxation time, a very useful relation can be thus obtained:

$$\rho_{xy}(B) = \frac{B}{ne} \tag{1.23}$$

The field dependence of the hall resistivity can be measured experimentally. As it can be seen from the equation, it will be a linear proportionality between ρ_{xy} and B, assuming that the carrier concentration n in the semiconductor is constant at a determined temperature. The carrier concentration is obtained through the slope of the linear function $\rho_{xy}(B)$ and the type of carrier determined through its sign. That is why the factor $(1/ne)$ is of great importance and is usually called $Hall-constant$. With the relation $\sigma = ne\mu$, the Hall-mobility can be expressed in terms of the hall constant:

$$R_H = \frac{1}{ne} \tag{1.24}$$

$$\mu_H = \frac{\sigma}{ne} = \sigma R_H \tag{1.25}$$

This calculations in the one-band model have indeed their limitations. As soon as there are holes which are also contributing to the electrical transport, the model has to be extended. The holes will be also affected by the external magnetic field, though having a different mobility, mass and obviously charge. Because of the latter, the holes will create a Hall-field in the oppposite direction, thus compensating the field created by the electrons. It is worth to mention that this compensation is not symmetric. Even the ideal case of an n-and p-doped semiconductor with equal number of donors and acceptors would not decrease the Hall-field to zero, due to the different masses and mobilities. In Hall-effect measurements, these compensation effects may be the first suspects, if, for example, the measured Hall-voltage has a very low value despite a higher expected carrier concentration. The experimental interpretation of the Hall-Effect in a semiconductor is therefore not an easy issue, and it should be submitted to a careful analysis.

1.1.4 Zinc-oxide: Properties and applications

ZnO usually crystallizes in the hexagonal (wurtzite) structure with lattice parameters a=0.325nm and c=0.521nm. It is a direct band gap semiconductor with $E_g = 3.4$ eV at room temperature. The optical properties of ZnO, studied using photoluminesence, absorption and photoconductivity, reflect the intrinsic direct band gap and a strongly bound exciton state [15]. A summary of the basic parameters of ZnO is shown in Table 1.1.

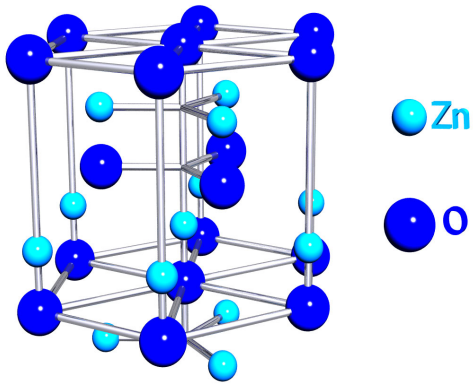

Figure 1.8: Wurtzite structure of ZnO.

To realize any type of device technology based on ZnO, it is important to have control over the concentration of intentionally introduced impurities, called dopants, which are responsible for the electrical transport of ZnO (see Section 1.1.2). The dopants determine whether the current is carried by electrons or holes (n or p-type). As a common occurence in wide-gap semiconductors, it is difficult to achieve bipolar doping (n- and p-type)[15].
The dopants are also called shallow level impurities because they introduce energy levels close to one of the allowed energy bands in the material. Electron doping in nominally undoped ZnO has been attributed to Zn interstitials (atoms sitting in the open regions around lattice sites), or oxygen vacancies. A recent report [16], however, demonstrates that oxygen vacancies are deep donors, with an energy of 1 eV below the conduction band. The intrinsic defect levels that lead to n-type doping lie approximately 0.01-0.05 eV below the conduction band (Zn-interstitials: $\approx$ 30meV). p-type doping, however, is rather difficult to achieve. There is only one recent report which descibes a recipe with high reproducibility [17].
ZnO based DMS have high potential for functionalities utilizing its wide band gap.

Property	**Value**
Lattice parameters at 300K	
a_0/c_0	1.602 (1.633 for ideal hexagonal structure)
Density	5,606 g/cm^3
Stable phase at 300K	wurtzite
Melting point	1975°C
Linear expansion coeffcient(/C°)	a_0:6.5×10^{-6}, c_0: 3.0× 10^{-6}
Static dielectric constant	8.656
Intrinsic carrier concentration	$\leq 10^6$cm^{-3}
Electron effective mass	0.24
Electron Hall mobility at 300K	
for low n-type conductivity	≈200 cm^2/V·s
Hole effective mass	0.59
Hole Hall mobility at 300K	
for low p-type conductivity	5 - 50 cm^2/V·s

Table 1.1: Properties of wurtzite ZnO

Besides, it is a well-known piezoelectric and electro-optic material, and can be easily deposited in thin film form. It has wide applications in electronic devices, such as transparent conductors, varistors (variable resistors), ultra violet laser sources and ultraviolet detectors [18]. Regarding the materials processing point of view, both doped-and undoped bulk-ZnO are relatively easy to process and result in a stochiometrical very stable compound.

1.2 Mechanisms of ferromagnetic ordering in DMS

As stated in the introduction, one of the most important aspects in the theory of DMS is to understand the origin of ferromagnetism in those systems. There are plenty of experimental reports that even underline the achievement of room-temperature ferromagnetism. However, this property has been found to be very sensitive to the choice of suitable parameters for processing bulk materials or growing thin films [4, 9, 19, 20, 7]. The range of measured Curie-temperatures varies therefore from 300 up to 900K [10]. But all this experimental work could not be summarized in one universal theory model. Nevertheless, there are two models which describe the origin of room-temperature ferromagnetism in DMS, which will be discussed in this chapter. As a prerequisite to understand the theoretical models, the basic concepts of ferromagnetism and the different exchange mechanisms will be described first.

1.2.1 Ferromagnetism and exchange interactions

When the orientation of the magnetic moments of electrons can be only controlled through external agents, such as an applied magnetic field, the material is called a paramagnet. At zero field, the existent magnetic moments are randomly aligned, and do not interact with each other. This lack of collective interaction among the individual moments makes the external field to be the only reason for of the creation of an ordered system.

If the magnetic moments are not existent in the intrinsic material, but induced through an external field, an immediate consequence will be the decrease of the field intensity. This phenomena is called diamagnetism. (A perfect diamagnet will be a superconductor, which is able to reduce the external field intensity to such point, that the applied field will be expulsed from the material.)

Ferromagnetic materials, on the contrary, possess a spontaneous magnetization, that means, their magnetic nature does not depend primarily on external agents, like a magnetic field in the case of para- and diamagnetism. The magnetic moments are already aligned in a determined direction, which implies that there is a mechanism that is responsible for this long-ranged ordering. There is a possibility, however, to disturb and even destroy ferromagnetism. Applying high energies to the system (e.g thermal) could indeed provoke the collapse of this magnetic, long-ranged ordering, and the material becomes paramagnetic with randomly oriented magnetic moments. The transition point, where a ferromagnetic material loses its unique properties, can be described in terms of a critical temperature T_c (also called Curie-Temperature). By reversing the process (e.g cooling below T_c), the spontaneous magnetization reappears with equal intensity, assuming of course that there have been no structural or chemical changes during the heating.

Another astonishing property of ferromagnetic materials, in the absence of an external field, is that they may show no macroscopically observable magnetization, although they are spontaneously magnetized. The reason for that is the presence of ferromagnetic *domains*, which are spontaneously magnetized regions separated by so-called domain walls or $Bloch - walls$. The magnetization vectors of the domains are arranged in such a way that their vector sum is zero, in order to reduce the magnetostatic energy that would be associated with the leakage of magnetic flux into the surrounding air space (process from (a) to (d) in Fig.1.9) As a golden rule in dynamical processes, the system will find its equilibrium in the state of minimal energy. The division into domains will therefore not continue indefinitely, it will stop until the energy expended in forming a new domain wall is greater than the corresponding reduction in magnetostatic energy.

In a domain wall, the magnetization direction changes gradually from one domain (↑)

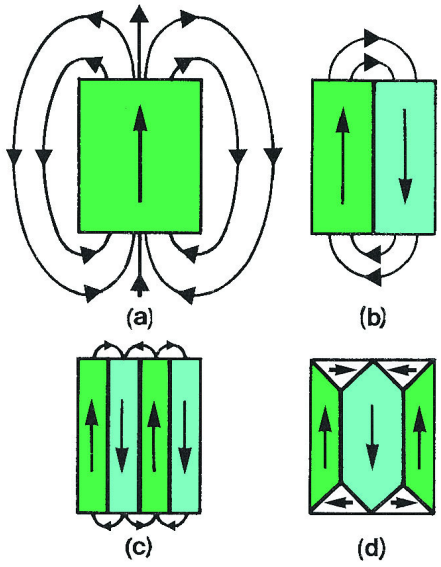

Figure 1.9: Building of magnetic domains in a ferromagnet.

to the adjacent one (↓) within the domain width δ, as described in Fig 1.10. If the domain wall is located between domains that are aligned antiparallel, it is called a 180° wall; a 90° domain wall will appear between perpendicularly aligned domains.

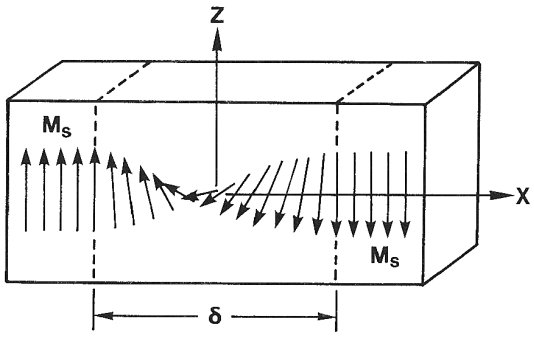

Figure 1.10: Magnetic structure of a 180° domain wall. M_s is the magnetization, δ is the domain wall width.

An appreciation of domain structures will enable a better understanding of the mechanisms of magnetization and hysteresis behaviour in ferromagnetic materials. Considering a material with very simple domain structure, see Fig 1.11, when an external field H is applied, the domain whose magnetization vector is closest to the field direction will grow at the expense of that which is less favorably oriented. Thus the process of magnetization is one of domain growth and displacement of domain walls,

which are ultimately thrown out of the material. The final stage of magnetization involves the rotation of the domain magnetization vectors away from the *easy axis* of magnetization (if we assume the existence of magneto-crystalline anisotropy), and hence requires larger applied fields, so that the rate of change of magnetization with applied field is considerably reduced, as seen in Fig 1.11. The *easy axis* is the preferred direction, in which the magnetic moments of a material tend to align, or, in other words, where the alignment of magnetic moments build the state of lowest energy. Due to the existance of an easy axis for anisotropic magnetic materials, the direction in which the external field is applied is of extreme importance.

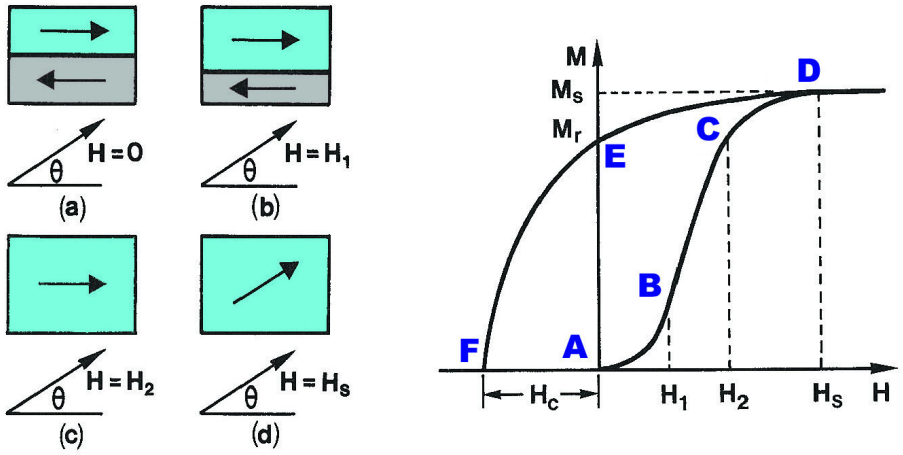

Figure 1.11: Changes in domain structure with increasing applied field. The direction of the field H will determine which domain will prevail (stages (a),(b) and (c)). At the stage (d) nothing else will happen, since magnetic saturation is reached. The changes in magnetization through domain displacement ((a),(b),(c),(d)) is plotted in a hysteresis curve (points A,B,C,D), respectively.

When the external applied field has already managed to modify the magnetic structure to a single domain, and, furthermore, align the magnetic moments pointing in its direction, it will come to a saturation. A further increase in the magnetic field will not produce any change in magnetization. The dynamics of magnetic ordering before reaching the first saturation (see Fig.1.11) are described by the so-called virgin curve, starting from the origin through the points B and C to reach saturation at point D. If, after saturation, the field is decreased to zero, the original magnetization curve is not retraced; instead, the magnetization remains at higher level than expected for the particular field value and gives rise to the phenomenon of magnetic *hysteresis*. There is not enough energy to reverse the process (d) to (a) (see Fig.1.11) and build domain structures again; the system will keep the scenario (c) since it represent the state of

lowest energy. There is a remanent magnetization M_r, which can be lowered to zero by applying a reverse field H_c, known as the coercive field or the *coercivity*. This reverse field will favour the formation of domain structures, until the macroscopical magnetization will be reduced to zero (path E→F in Fig.1.11). Increasing further the reverse field $-H$, an analogous behaviour will be expected as in the positive case: the hysteretic $M - H$ curve will be symmetric to the origin, see Fig.1.12.

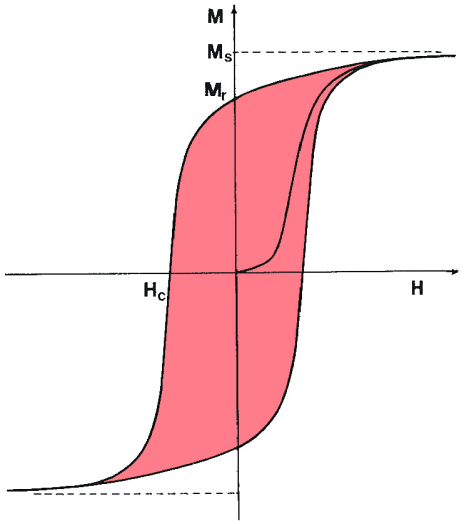

Figure 1.12: Hysteresis loop of a ferromagnetic material, with saturation magnetization M_s, remanence M_r and coercivity H_c. The area within the hysteresis loop represent the magnetic energy saved in the system.

During the magnetization process, the applied field moves the domain wall through the material against various microstructural and crystallographic obstacles. The magnitude of the field required to do this determines whether the material is classified as magnetically *hard* or *soft*. If there are many pinned defects in the crystal, or misformation in the crystal structure, greater energy and hence a higher magnetic field would be required in order to produce a change in the magnetization. As a consequence, the coercivity will increase. This is the case of a *hard* magnetic material; and the magnetic energy saved in the system, which has to be delivered by external agents to produce any change in the magnetic structure, is given by

$$E_m = \oint_{area} MdB \tag{1.26}$$

which graphically represents the area within the hysteresis loop (Fig 1.12). The magnetization of soft magnetic materials, on the contrary, can be modified applying less energy. As a consequence, the coercive field and hence the area under curve will have a lower value.

Regarding the exchange mechanisms which enable the alignment of magnetic moments in ferromagnets, the first idea which could come up would be the classical dipole-dipole interaction between atomic magnetic moments m_1 and m_2, given by following relation

$$E_{dipol} = \frac{\mu_0}{4\pi r^3}(\vec{m_1} \cdot \vec{m_2} - \frac{3}{r^2}(\vec{m_1} \cdot \vec{r})(\vec{m_2} \cdot \vec{r})) \tag{1.27}$$

where $\vec{r}$ and r are the relative distances of the atoms. But this interaction is very weak and a even low thermal energy will be enough to neutralize its effect. However, this classical Dipole-Dipole exchange interaction may play a non-negligible role in the ultra-low temperature regime [21].

A model, which is based on the direct interaction between neighbouring atoms was proposed by Heisenberg. It is classified as a direct interaction because the electron orbits of neighbouring atoms come to an overlap. The contribution of this overlap to the exchange interaction is quantified by the exchange coupling constant J. Is the coupling constant J negative, then antiferromagnetic ordering is favoured due to the reduction of energy in antiparallel configuration, while for positive J the parallel spin alignment will create a stable ferromagnetic state. The Heisenberg-Hamiltonian is given by

$$H_{1,2} = -2J_{1,2}\vec{S_1} \cdot \vec{S_2} \tag{1.28}$$

where S_1 and S_2 are the spin moments of two neighbouring atoms, and $J_{1,2}$ their coupling constant.

Since the electronic orbits of the atoms have to overlap to fulfill the premises of this model, this direct interaction is short-ranged. However, a mean field approximation has been used to expand this model. The interaction of one spin moment with its surroundings is considered by the introduction of a mean field B_a. In other words, all the surrounding spin moments are represented through an homogeneous, macroscopic magnetic field B_a, assuming that all the atoms interact with each other via the same coupling constant J. Thus, the interaction of one atom with its n-neighbours will be given by the following relation

$$H_i = -2J \sum_{j=1}^{n} \vec{S_j} \cdot \vec{S_i} \tag{1.29}$$

Taking into account the magnetization of n_0 atoms per volume unit, and approximating their spin moments $\vec{S_j}$ through a time mean value $\left\langle \vec{S_j} \right\rangle$, the relation between magnetization and spin can be written as

$$\vec{M} = -\frac{n_0}{n} \cdot g\mu_B \sum_{j=1}^{n} \left\langle \vec{S_j} \right\rangle \tag{1.30}$$

where μ_B is the bohr magneton and g is called the Lande-factor [11]. Using equation 1.30 to insert the sum of the mean value of the spins $\vec{S_j}$, the hamiltonian in 1.29 can be written as

$$H_i = -\left(-g\mu_B\vec{S_i}\right)\cdot\frac{2nJ}{n_0g^2\mu_B^2}\vec{M} \tag{1.31}$$

Equation (1.31) can be interpreted as the potential energy from a magnetic dipole $-g\mu_B\vec{S_i}$ under the action of a magnetic field of the form

$$\vec{B}_{mean} = \frac{2nJ}{n_0g^2\mu_B^2}\vec{M} \tag{1.32}$$

This is nothing but the representation of the mean or molecular field, which is proportional to the magnetization. The macroscopical magnetization $M = \left|\vec{M}\right|$ of a ferromagnetic material in the mean field approximation, cannot be analytically, but graphically determined [11].

Besides the direct spin coupling interaction postulated by Heisenberg, there are also indirect exchange interactions which play an important role for collective mechanisms of long-ranged magnetic ordering. Super-exchange , for example, is mediated through the virtual displacement of an electron and its respective spin from one atom to the other. Hence it is a virtual process: the electron and its spin moves constantly from one atom to the other and back, filling the respective energy states for a short moment. In the simple case of two neighbouring atoms, the state of lowest energy will be achieved when the electron spins are aligned antiparallelly, enabling the „virtual hopping“ from one orbital (or energy state) to the other. If the spins are aligned parallel to each other, the spins will not move from their positions due to the Pauli-principle of exclusion, when there are no other energy levels available. That is why superexchange has been attributed to be a predominantly antiferromagnetic interaction.

It is also possible that super-exchange is mediated through a third atom, lying between the two atoms in question. The probability of a ferromagnetic coupling is low, since the electrons of the interacting atoms have to be either in different energy states (case (a) in Fig 1.13) or the third atom which acts as „link“ has to provide one electron from a different energy state to decrease the energy of the system (case (b) in Fig.1.13).

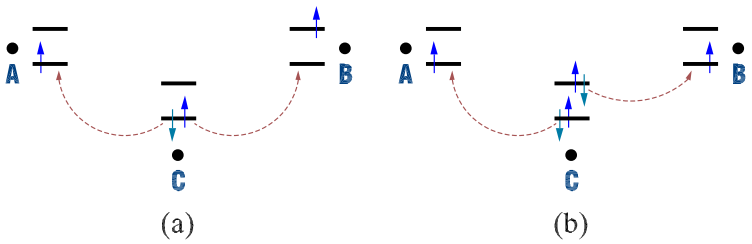

Figure 1.13: Possibility of ferromagnetic coupling via Super-exchange through a third atom C, lying between lattices sites A and B. Note that the probability of existance of this scenarios is rather low, due to the very specific configurations to be fulfilled.

When the interacting atoms are not isovalent, a free extra electron will be even favoured to change its position from one atom to the other, because the ion which has less valence will have one unfilled orbital in its electronic structure, thus enabling the real „hopping“ of an electron without the need to overcome any additional energy, and producing a stronger coupling. This phenomena is called double-exchange, and since the real transfer of electrons is the cause of ferromagnetic coupling, it is linked with a good electrical conductivity. Like in superexchange, this exchange interaction could not only be directly between the two magnetic ions, but also mediated through a third atom. Fig 1.14 describes a double exchange process between two Mn-ions through an O^{2^-}-ion. If this is the case of a periodical configuration of a crystal structure, the electron transfer will continue indefinitely, thus producing a long-ranged ferromagnetic coupling (Zener-model, see section 1.2.2).

Another exchange mechanism which bases in carriers as mediators for ferromagnetic long-ranged ordering, is the after Ruderman,Kittel,Kasuya und Yosida so-called RKKY-interaction. This model has been originally used to describe ferromagnetic coupling in metals, since one of the important premises for the RKKY-interaction to take place, is a sufficient amount of free carriers. The carriers located around the atoms will align their spins antiparallely to the localized magnetic moment of the atom body, thus shielding it magnetically to the surroundings. The same game will take place if there are more carriers surrounding the atom body and the first shell of polarized carriers: a polarization arises at the border of the first shell, and the second shell of carriers will align their spins antiparallely, trying to shield the first one. Due

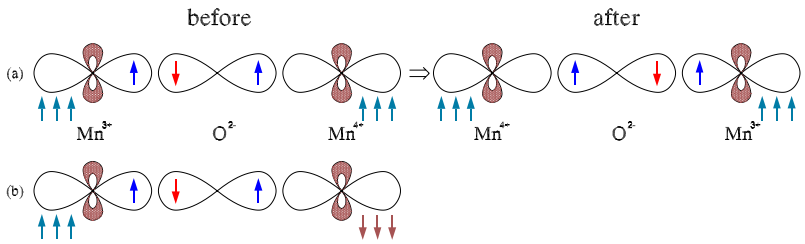

Figure 1.14: Double-exchange between Mn^{3+} and Mn^{4+} ions through an oxygen ion.

to this principle, the RKKY-interaction shows an oscillating behaviour, and the type of coupling (either ferro-or antiferromagnetic) will strongly depend on the distance between the interacting atoms. Fig 1.15 shows an example of ferromagnetic coupling through RKKY-interaction.

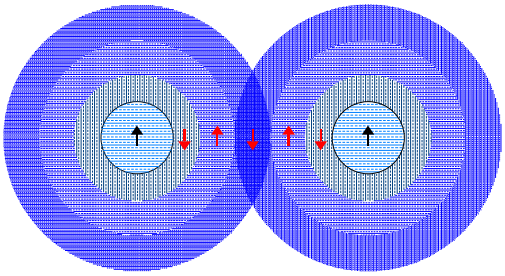

Figure 1.15: Ferromagnetic coupling between two atoms through antiparallel alignment of carrier shells. Depending on the distance between the atom centers, the spins will couple either ferromagnetic or antiferromagnetic.

1.2.2 Zener-Model

The model called after Clarence Zener, postulated in the early 50s, was originally used to explain the origin of ferromagnetism in doped manganese compounds with

perowskite structure. The model was a long time out of use and nearly forgotten, until Dietl *et al*. brought it back into life recently, in order to explain room-temperature ferromagnetism in dilute magnetic semiconductors.

The original Zener-model was proposed after experimental findings, which clearly showed an empirical correlation between electrical conduction and ferromagnetism of $(La_{1-x}A_x)MnO_3$ compounds. It was interpreted as the interaction of the incomplete d-orbits of the transition metals by virtue of conducting electrons.

Following Hunds rule, all unpaired electrons within each atom or ion will be aligned parallely, since this is the configuration where the system adopt its lowest energy. The electrons from the incomplete d-orbits will be able to move from atom to atom only if the atoms in question are not isovalent(e.g Mn^{3+}/Mn^{4+}), which implies the presence of a hole. Another requirement for the electron to move freely from one atom to the other, and, without changing its spin direction, is that all the spins of the incomplete d-orbits are aligned in the same way. This indirect coupling is a double-exchange process, and it will lower the energy of the system when the spins of the d-orbits are all parallel. According to this theory, ferromagnetism will never arise in the absence of conduction electrons, that is why that mechanism is called also „carrier-induced ferromagnetism“.

Considering dilute magnetic semiconductors, the necessary presence of holes will imply that the semiconductor must be p-doped and with enough hole concentration to ensure a long-range interaction. The alignment of the spins of the magnetic dopants will cause a spin-splitting of the valence band due to the strong p-d hybridization. This spin-splitting in the valence band will reduce the energy of the free carriers (holes), and at lower temperatures, where the contribution of the thermal energy is negligible, the energy of the system will arise mainly due to the spin-polarization. The magnetic atoms diluted in the host semiconductor will form pairs around a localized hole, coupling ferromagnetically through the double-exchange mechanism. Since the double-exchange is strong but short ranged, the low concentration of dopants in dilute magnetic semiconductors will not be enough to ensure a long-range ordering. The long-ranged interaction will be mediated by bound magnetic polarons (BMP), which preferentially form around the localized holes with ferromagnetically coupled TM(transition metal)-pairs, in the case of group III-V DMS. On the other hand, for group II-V DMS, the formation of polarons is not preferentially around pairs, in fact, they can encompass several TM-spins for a given concentration [3]. If the hole concentration is low, the magnetic polarons will not overlap, thus disabling the ferromagnetic coupling all over the crystal and enabling the formation of spin clusters, instead. Summarizing, elements which play the role of a magnetic ion and an acceptor at the same time, are perfect dopants which give rise to ferromagnetic ordering in

DMS, according to this theory.

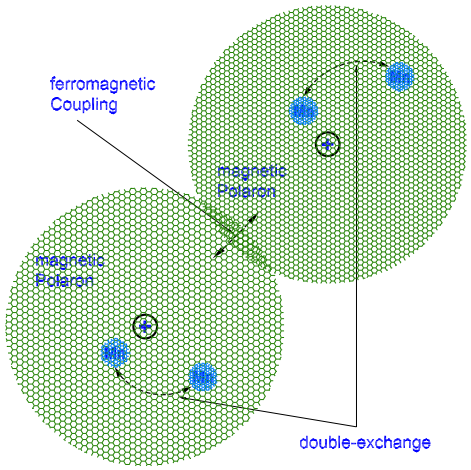

Figure 1.16: Exchange interaction through magnetic polarons in a hole-rich III-V DMS. To gain the coulomb-energy, the magnetic polarons will preferentially form around TM-pairs with a localized hole, which couple ferromagnetically through double-exchange.

The predicted Curie-Temperature exceeding room temperature for semiconductor such as GaN and ZnO, as seen in Fig.1.1, was estimated using Mn as TM-dopant with 5 percent atomic concentration, and a high hole concentration ($3.5\times10^{20}cm^{-3}$). A difference arises, however, when using the Zener-Model for III-V and II-V group semiconductors. In the case of Mn-doped II-V compounds like ZnO, the super-exchange mechanism will lead to an antiferromagnetic coupling between neighbouring Mn-atoms, thus competing with the ferromagnetic interaction. In practice, the contribution of the antiferromagnetic component due to superexchange is very low to cause a remarkable change in the macroscopic magnetization of DMS.

1.2.3 Spin-split impurity band model

As described in section 1.1.4, to realize p-type ZnO is a very difficult task. Diverse experimental reports in the last years claim to have achieved ferromagnetism at room-temperature in dilute magnetic semiconductors[4, 5, 6, 7, 8, 9, 20, 19]]. In the case of oxide-based DMS, a common feature of the systems is the n-type conductivity with a high dielectric constant: ferromagnetism could be found even in insulators. Considering these characteristics, the Zener-Model cannot be used to explain this interesting set of experimental findings, first, because of the lack of p-type conductivity, and second, because of the absence of mixed-valence magnetic dopants able to

interact via double-exchange. Besides, conventional interactions like super-exchange or double-exchange alone cannot produce long-ranged magnetic ordering with that low magnetic cation concentration.

An alternative model recently proposed by Coey *et al.*[10], tries to explain the origin of ferromagnetism in dilute ferromagnetic oxides with n-type conductivity. Electrons from shallow donors, as majority carriers, will be confined in an hydrogenic orbital of radius r_h, forming bound magnetic polarons. The formation of polarons is asocciated, as usual in many-body systems, with the principle of lowest energy. The magnetic moment of the donor electrons will modify its surrounding magnetic moments in such a way, that each electron will be magnetically shielded, minimizing the global energy (like in domain structures, when the net magnetic moment to the surroundings is equal zero). Within the polaron radius, all the magnetic moments will be aligned in the same way, forming an ordered, extended magnetic structure.

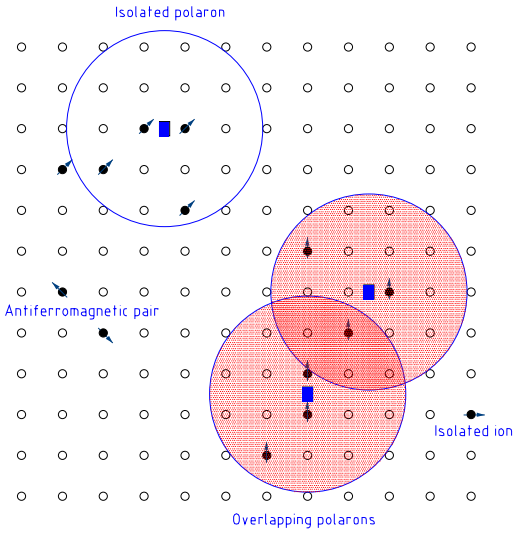

Figure 1.17: Formation of magnetic polarons, bound to a donor defect. It is clearly shown how the magnetic ions are aligned in the same direction only if they are within the action range of a polaron, as well as how magnetic polarons overlap and interact with each other. The donor defects are labeled in blue.

If the donor concentration is large enough, the magnetic polarons formed around the donor defects will overlap to create a spin-split impurity band. This overlap will create a larger polaron area where all the moments will point in the same direction, as seen in Fig.1.17, thus mediating the parallel, ferromagnetic coupling of the 3d-moments of the magnetic ions. Isolated magnetic polarons will also align the moments parallely within their radius, creating a ferromagnetic structure; but the absence of the overlap

will not enable a long-ranged interaction. Magnetic ion pairs, which are not in the vicinity of a donor-defect able to form magnetic polarons, may couple either ferro- or antiferromagnetically, depending just on their own exchange-interaction.

From this principle, it could be concluded that the strength of ferromagnetic coupling will depend crucially on the donor-defect concentration and the 3d-magnetic cation concentration. At a very high magnetic cation concentration but moderate donor concentration, there will be magnetic ions which are not under the action range of magnetic polarons. They could form a closed path and interact with each other over long distances, stimulating either ferri- or antiferromagnetic ordering. If the donor concentration is low, the magnetic polarons will not have the chance to overlap, thus forming isolated magnetic clusters. An overdose of donors with low magnetic cation concentration will create a spin-glass state [10].

As long as the donor concentration is sufficient and the magnetic cation concentration is not too high, due to the above described reasons, ferromagnetism will be the most stable state of a dilute magnetic semiconductor, according to this model. Since experimental reports claim the achievement of room-temperature ferromagnetism, there remains an open question from the model to be solved: the relation of the Curie-Temperature with the different parameters involved in the formation of this impurity band, or in other words, which circumstances and conditions will lead to ferromagnetic ordering above room temperature. For this purpose, the band structure and the energy levels of a doped semiconductor have to be considered.

Coey *et al*. used a two-sublattice mean-field approximation to estimate the Curie-temperature of dilute magnetic semiconductors. Applying this model for Co-doped ZnO, a Curie-Temperature of only 18 K could be estimated. A possibility to achieve a significant increase in T_c, however, is to increase the donor electron density in the vicinity of magnetic impurities, since a better „distribution“ of polarons over the magnetic cations will enhance the strength of ferromagnetic coupling. In order to distribute the necessary amount of donor electrons over the magnetic impurities, which implies a charge transfer, the unoccupied 3d-states of the magnetic cations have to hybridize with the donor-derived impurity band at the Fermi-level. A stronger hybridization will mediate better charge transfer, and hence, a more convenient donor distribution and a higher Curie-Temperature will be achieved.

The donor-derived impurity band is supposed to lie energetically close to the conduction band edge. The band structure of TM(transition metal)-doped ZnO is illustrated schematically in Fig 1.18, where the valence band is mainly built through the 2p-orbitals of oxygen atoms, while the 4s-orbitals from Zn-atoms will form the conduction band. The location of the 3d-states of the transition metals and hence

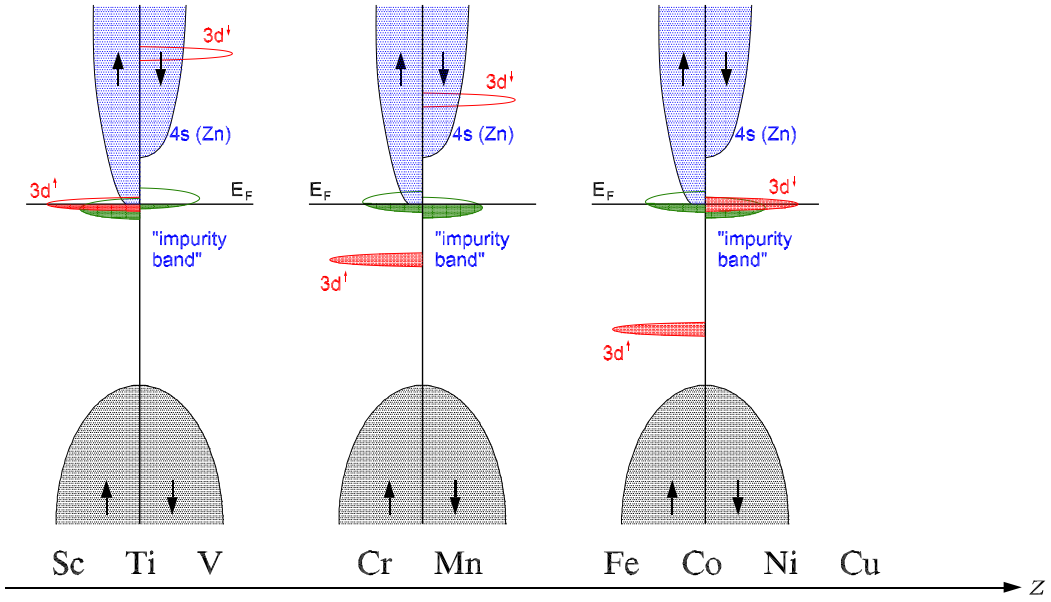

Figure 1.18: Schematic band structure of an oxide-based DMS, with 3d-impurities and a donor impurity band.

the possibility of an hybridization with the donor-derived „impurity band“ will obviously depend on which element is used for doping. From Sc to Cu, the spin-split 3d-states will shift down in the energy scale with increasing atomic number Z. According to this model, a stronger hybridization at the Fermi-level and thus a higher Curie-Temperature will be expected in two regions: one near the beginning of the series where the $3d^{\uparrow}$ states cross the Fermi-level in the impurity band, and one towards the end where the $3d^{\downarrow}$ states cross E_F (first and third scenario of Fig.1.18). Since the exact position in the energy scale of the spin-split 3d-states for each element is difficult to determine, as well as the width and the energy level of the impurity band, this model has its limitations for a quantitative description. In the case of Cu, for example, it is not clear how far the empty $3d^{\downarrow}$-states lie under the conduction band. Therefore, the possibility of an hybridization with the impurity band is not neglected. Experimental reports, however, confirm the trend shown in this model, since the highest reported magnetic moments were found at Co,V,Ni and Fe.

2. Experimental methods and techniques

2.1 Pulsed Laser Deposition

The pulsed laser deposition (PLD) is one of the most used techniques for depositing thin films. In the process of laser ablation, short and high-energetic laser pulses (ns) are used to evaporate matter from a target surface. As a result, a supersonic jet of particles, called also „plume“, due to its form (see Fig 2.2), is ejected from the target surface and expands away from the target with a strong forward-directed velocity distribution. The ablated particles condense on a substrate placed opposite to the target. The ablation process takes place in a vacuum chamber- either in vacuum or in the presence of some background gas. The laser pulses are guided to the vacuum chamber by means of optical devices, such as mirrors and lenses, which in addition focuse the beam to the target, optimizing the energy density of the laser pulses. While the laser pulses are hitting on its surface, the target is usually rotated with a constant speed to achieve an homogeneous ablation process. The possiblity of a multitarget rotating wheel in the vacuum chamber enables more efficient and complex processes. Multilayers and alloy films can be grown from elementary targets by moving them alternately into the laser focal point.

The high energy density used in a typical PLD process is able to ablate almost every material; and by controlling the process parameters, high-quality films can be grown reliably in a short period of time compared to other growth techniques (MBE,Sputtering). Another known advantage of the PLD technique is the accurate stochiometric transfer from target to film. There are several kinds of lasers, which are commercially available, and the choice of Excimer lasers (KrF, ArF, XeCl) are widely used to deposit complex oxide films because of the larger absorption coefficient and small reflectivity of materials at their operating wavelengths[22]. Frequency tripled Nd:YAG lasers are also effective from the same point of view.

For the present work, a Continuum (model NY81-C) frequency tripled Nd:YAG laser was used, with a working wavelength of 355nm, operating with a pulse repetition rate ranging from 2 to 10Hz, and a tunable energy fluence with its maximum at 6 J/cm^2. The substrate, mounted on a heating block opposite to the target, could be heated

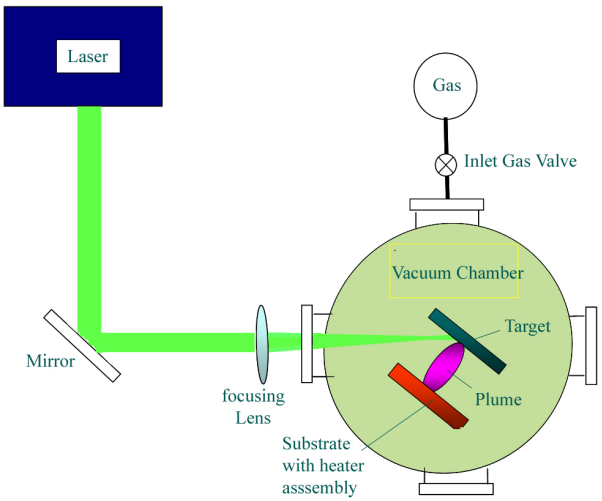

Figure 2.1: Schematic view of the PLD apparatus, at the Royal Institute of Technology.

from room-temperature up to 900C. The temperature could be kept constant by means of an automated temperature controller, capable to program and control several ramps and dwells with user-defined heating and cooling rates. The thermal coupling between heater and substrate is achieved through appropriate amount of conductive silver in the back side of the substrate. Moreover, several gases (O_2, N_2, H_2, Ar) can be introduced in the deposition chamber if the presence of any background gas is required for the film growth. The flow and the pressure of each gas was controlled by means of gas inlet valves and pressure flow controllers. However, base pressures in the range $p \leq 10^{-4}$mbar could not be achieved due to the lack of a (U)HV-system. The targets used are relatively small, not greater than 25mm in diameter and have the form of a „pellet“. The schematic view of the configuration of the PLD apparatus used in the present work, is sketched in Fig(2.1).
Although the pulsed laser deposition process is conceptually simple, controlling the dynamics of the film growth is not an easy issue, because of the large number of interacting parameters that govern the growth process and hence the film properties, such as:

- the laser parameters (working wavelength, fluence, pulse duration, and repetition rate);
- the substrate type, orientation and temperature;
- the structural and chemical composition of the target material;
- the chamber pressure and the chemical composition of the buffer gas;

- and the geometry of the experiment (incident angle of the laser, incident angle of the plume, distance between target and substrate)

Being able to control the parameters for a given system, the advantages of the PLD technique can be profited. In practice, parameters like laser settings and experiment geometry have to be optimized for a given system and be kept constant, while another parameters like substrate temperature, chamber pressure and background gas can be varied in order to investigate their influence on the film growth. A detailed discussion of the role of growth parameters will follow in Chapter 4.

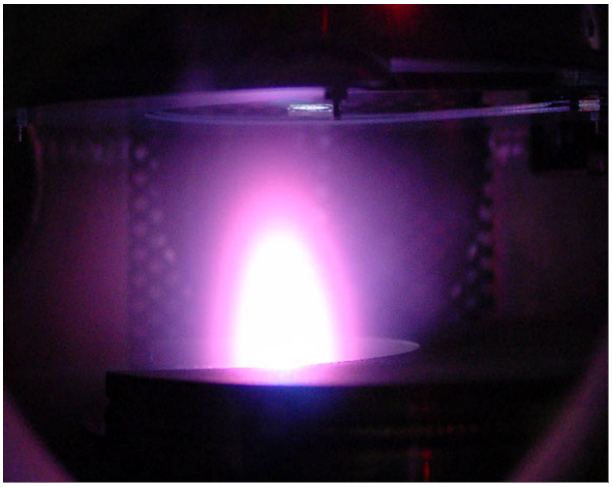

Figure 2.2: Plasma plume in an ablation process.

2.2 X-ray Diffraction

X-ray diffraction (XRD) is a versatile, non-destructive analytical technique for identification and quantitative determination of the various crystalline forms known as *phases* present in bulk- and thin film samples. Identification is achieved by comparing the X-ray diffraction pattern obtained from an unknown sample with an internationally recognized database containing reference patterns for more than 70,000 phases. For each phase present in the sample, a quantitative structural analysis can be performed.

The structure of a crystal lattice can be represented as a regular array of atoms. These are arranged to form a series of parallel planes separated from each other by the distance d, which varies according to the nature of each material. Any crystal plane oriented in different direction has different d- spacing. When a monochromatic x-ray beam with wavelength λ is incident on the lattice planes in the crystal at an angle θ ,

diffraction occurs only when the distance travelled by x-rays reflected from successive planes differs by a complete number n of wavelengths (Fig.2.3). This phenomena of constructive interference is summarized by the so-called Bragg condition given by

$$n\lambda = 2d\sin\theta \tag{2.1}$$

By varying θ, the Bragg's law can be satisfied by different d-spacing in a polycrystalline material. Plotting angle position and intensity of the resultant diffraction peaks produces a pattern, which is characteristic of the sample. For a sample containing many phases, the XRD pattern is formed by superposition of individual patterns.

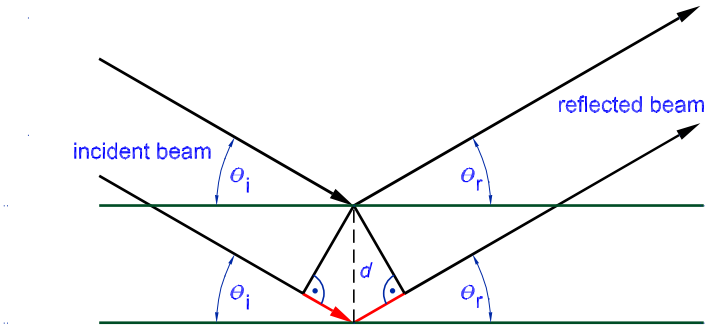

Figure 2.3: Schematic view of the geometry of Bragg-reflexion. Incident angle θ_i and reflection angle θ_r are equal.

The Bragg-condition, however, limits the range of wavelenghts which can be used, since the wavelength has to be shorter than the double d-spacing in order to detect the constructive interference within the crystal planes. For a lattice constant value of d=0,5nm, the wavelength has to be shorter than 1nm. Due to this reason, only x- or γ-radiation can be used to analyse structures of crystalline solids.

The three basic components of an x-ray diffractometer are: x-ray source, specimen (diffraction plane), and x-ray detector. The source emits typically Cu-K_α radiation in commercial x-ray diffractometers. Since in this radiation both Cu-$K_{\alpha1}$ and Cu-$K_{\alpha2}$ lines are present and could generate double reflections, the Cu-$K_{\alpha2}$ is filtered by means of a monocromator. The angle between the plane of the specimen and the x-ray source is called ω, and the one between the projection of the x-ray source and the detector is 2θ.

The structure of the samples in bulk and thin film form prepared in this project,

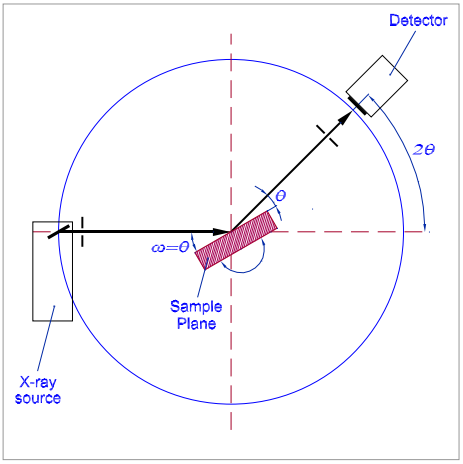

Figure 2.4: Basic configuration of a 2-circle diffractometer.

was analized with a 2-circle diffractometer of the company Panalytical, and a 4-circle diffractometer (Bruker AXS-Discover D8). Since the 4-circle diffractometer has 4 angles (ω,2θ,χ,ϕ) which can be varied independently, any plane in the 3-dimensional crystal lattice can be reached and analized. The following measurements have been performed with the available equipment:

- ω - 2θ scan, used for the identification of phases, as well as for the calculation of the lattice constants for a given orientation. To find out at which angle ω=θ the Bragg-condition is fulfilled, the detector will rotate 2x faster than the source around the fixed sample plane, so that the relation θ-2θ remains constant during the whole scan.

- Rocking-curve, a special scan mode in the ω - 2θ configuration. Holding the 2θ angle in a fixed position, the incident angle ω will be swept usually in the range $[+1, -1]$ degrees around θ. The purpose is to find out if there is a misalignment (tilting) of the crystal planes , fact that would lead to the fulfillment of the Bragg-condition for other angles which differ from θ. This structural mismatch is called *mosaicity*. A very sharp Rocking-Curve implies homogeneously aligned crystal planes; a broad one means that the Bragg-condition has been fulfilled for other angles around θ and hence a mismatch in the crystal planes. The value which describes the *mosaicity* of a crystal quantitatively, is thus the FWHM (Full Width at Half Maximum) of the Rocking-curve.

- ϕ-scan: Having four angles as degrees of freedom in a four-circle diffractometer, any plane with arbitary orientation can be reached. The so-called ϕ-scan rotates

the plane up to 360° degrees around its normal axis, at fixed angles θ,2θ and χ. This measurement could be used to check the type of crystal structure expected for the material (cubic, tethragonal,hexagonal). For that purpose, an in-plane reflection has to be searched to proceed with the ϕ-scan. For an hexagonal structure, the intensity peaks, where the Bragg-condition is fulfilled, will be expected near 0°, 60°, 120°, 180° and so on.

Another measurement which is performed with the same equipment and which is very useful for thin film analysis, is the X-ray Reflectometry. Due to its versatility to determine important quantities such as thickness, roughness and film density in one measurement, it will be described separately in the next section.

2.3 X-ray reflectometry

Since the determination of most physical properties of materials require the exact sample dimensions, determination of film thickness with high precision is very crucial for thin film technology (heterostructures, tunnel junctions). The main advantage of X-ray-reflectometry (XRR), is thus to be a non-contact and non-destructive technique for thickness determination between 15-200nm with a precision of about 0,3nm. An important premise is, however, that substrate and film have different reflective indexes. In addition to thickness determination, this technique is also employed for determination of film density and roughness.
The XRR method involves monitoring the intensity of the x-ray beam reflected by a sample at grazing angles. A monochromatic x-ray beam of wavelength λ irradiates the sample at a grazing angle ω and the reflected intensity at an angle 2θ is recorded by the detector. The mode of operation is thus ω-2θ (see section 2.2). The reflection at the surface and interfaces is due to the different densities in the different layers (substrate-film or film-film, interface), which corresponds to different reflective indexes in the classical optics. For incident angles θ below a critical angle θ_c, total external reflection occurs. This transition will thus depend on the density of the sample. Above θ_c, the reflection waves from the different interfaces interfere and give rise to inteference fringes. The period of the interference fringes and the fall in the intensity are related to the thickness and the roughness of the layer interfaces, respectively. The reflection phenomena can be analyzed using the classical theory (Fresnel equations). The relation used to estimate the thickness is given by

$$d = \frac{\lambda}{2} \frac{1}{\sqrt{\theta_{m+1}^2 - \theta_c^2} - \sqrt{\theta_m^2 - \theta_c^2}} \approx \frac{\lambda}{2} \frac{1}{\theta_{m+1} - \theta_m} \tag{2.2}$$

where m and (m+1) represent the order of neighbouring maxima/minima, λ is the

irradiated wavelength and θ_c the critical angle for total reflection. The last term is valid only for $\theta_m \gg \theta_c$. For measurements exhibiting interference fringes in a bigger angular range, the thickness is even determined with a precision of 0,1nm.

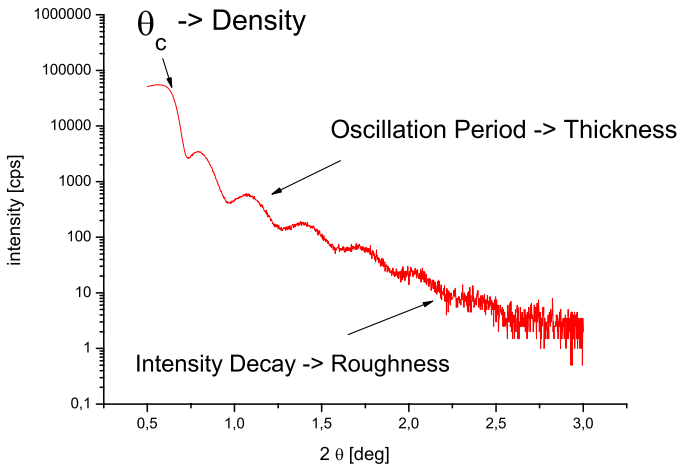

Figure 2.5: Example of a XRR-measurement, showing how the physical properties of thin films can be obtained from the intensity pattern.

Regarding roughness determination, both surface and interface roughness can be estimated. Roughness gives rise to diffuse scattering, resulting to a less intensity in the specularly reflected beam. General scattering formalisms have been developed that calculate the scattered fields for both specular and non-specular scattering. In one of the formalisms, Nevot and Croce considered roughness by assuming non-homogeneous thickness, with a gaussian distribution with a mean d and a standard deviation σ. Correcting the Fresnel coefficients of reflection with the factor $\exp(-\frac{d}{2\sigma^2})$, the influence of the roughness on the reflected intensity could be determined: the sooner the interference fringes dissappear, the higher the roughness.
Since the calculation of both thickness and film roughness is involved with statistic methods, it was performed with the software Leptos. The typical range for these measurements are between 0,5° and 5° in 2θ.

2.4 Scanning Electron Microscopy

The Scanning Electron Microscope (SEM) is a valuable technique for the inspection, examination and evaluation of materials. The sample to be examined is placed on a specimen stage inside a vacuum enclosure of the SEM station and is irradiated with a finely focused beam of electrons. The electron beam, with energies typically in

the range from a few hundred eV to about 30 KeV, can be static or swept over the specimen surface. The resulting signals that are produced when the scanning electron beam impinges on the surface of the specimen include secondary emission electrons, primary backscattered electrons, and X-rays.

Secondary electrons are specimen electrons that obtain energy by inelastic collisions with beam electrons. They are defined as electrons emitted from the specimen with energy less than 50eV, and are predominently produced by the interactions between energetic beam electrons and weakly bonded conduction-band electrons in metals or the valence electrons of insulators and semiconductors. There is a great difference between the amount of energy contained by beam electrons compared to the specimen electrons and because of this, only a small amount of kinetic energy can be transferred to the secondary electrons. Elastic scattering occurs between the negative electron and the positive nucleus (Rutherford scattering). Sometimes the angle is such that the electron comes back out of the sample. Therefore, the elastic scattered primary beam electrons are called backscattered electrons. The signal of secondary and backscattered electrons vary as the result of differences in the surface topography as the scanning electron beam is swept across the specimen surface. The x-ray radiation is produced deeper in the specimen, therefore it is not used for topography analysis.

The secondary emission of electrons from the specimen surface is usually confined to an area near the beam impact zone that permits images to be obtained at high resolution. These images, as seen on a cathode ray tube, provide a three dimensional appearance due to the large depth of field of the SEM as well as the shadow relief of the secondary electrons contrast. In a typical SEM, a resolution of 10nm can be attainable, and a depth of field (focus) can reach 300 times that of an optical microscope.

Since the primary beam electrons displace the inner shell electrons of atoms in a specimen, the electrons of the outer shells will try to fill the vacancies, which results in x-ray radiation being emitted. Because every atom in the periodic table has a unique electronic configuration, the X-rays produced carry a unique atomic signature in the form of a characteristic energy. The method which makes use of this particular relation to determine the actual composition of the specimen is called EDX (Energy Dispersive X-ray analysis). The EDX method employs a solid state detector to measure the distribution of the x-ray energies, thereby allowing one to identify and quantify elemental species. Rastering of the beam across the surface enables to track the locations of sample x-rays, and hence, 2-dimensional chemical maps can be constructed.

For the elemental analysis of the thin film samples in the present work, energy dispersive X-ray analysis was performed on a Germanium (Ge) detector (LINK Gem Oxford) in a JEOL JSM-840 SEM. The detector was able to identify elements from $_5$B to $_{92}$U. At a typical acceleration voltage of 20kV, the x-ray radiation was produced between 100-500nm deep in the sample. Due to this fact, the accuracy of the compositional analysis will depend on the sample thickness.

2.5 Vibrating Sample Magnetometer (VSM)

The VSM technique is used to measure the change of magnetization of materials as a function of an external field, which enables to identify their magnetic nature. As explained in section (1.2.1), para-, dia- and ferromagnetic materials will have a different reaction to the applied field. In ferromagnetic samples, a hysteresis loop is expected.

The principle of the VSM is, as its name reveals, based on the mechanical vibration of a magnetic sample in an homogeneous magnetic field, which will produce a change in the magnetic flux in the neighbourhood of the sample. The sample is vibrating sinusoidally at a small fixed amplitude with respect to stationary pick-up coils (see Fig.2.6). According to Faradays law, an electromagnetic field will be induced, proportional to the rate of the flux change, as

$$V(t) \propto \frac{d\Phi}{dt} \tag{2.3}$$

The resulting field change $\partial B(t)$ at a point $\vec{r}$ inside the detection coils induces a voltage. The field $\vec{B}$ is given by the dipolar approximation, assuming small dimensions of the magnetized sample in comparison to its distance from the detection coils

$$\vec{B}(r) = \frac{\mu_0}{4\pi}\left(\frac{\vec{m}}{r^3} - \frac{3(\vec{m}\cdot\vec{r})\vec{r}}{r^3}\right) \tag{2.4}$$

where $\vec{m}$ is the magnetic moment of the -through the external field- magnetized sample. Measuring the induced voltage at the pick-up coils will therefore lead to the determination of the magnetization of the sample. The signal from the pick-up coils is fed to a phase sensitive detector, which takes as a reference signal the frequency obtained from the electro-mechanical sample drive assembly, so that the magnetometer is only sensitive to signals which are coherent with the sample vibration. The lock-in amplifier signal handling technique considerably enhances the signal-to noise ratio. Assembling a cryostat to the system, temperature dependence of the magnetization can be measured. The samples suitable for this measurement set-up, range from bulk materials (powder and pellets), thin films to even fluids. For powders and fluids, a capsule is used to avoid the diffusion of the material.

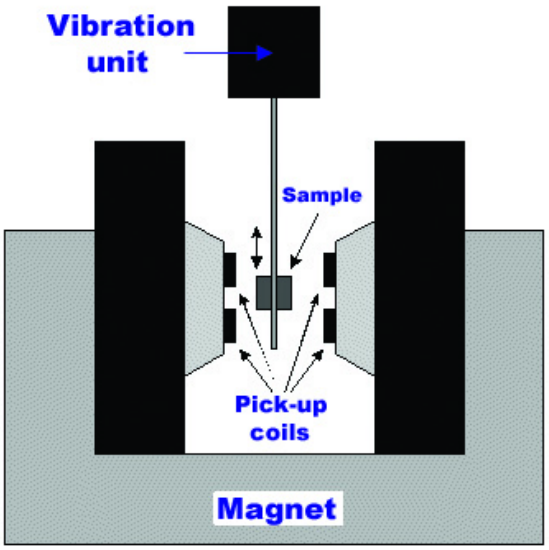

Figure 2.6: Schematics of a VSM-Magnetometer.

The measurement of the field dependence of the magnetization for bulk- ZnO:Cu materials, was performed with the VSM EG & G Princeton (Model 155-S), with a Lake Shore current source and an electromagnet able to deliver fields up to 1 Tesla. The VSM was able to detect magnetic moments down to 10^{-5} emu. Since only room-temperature measurements were performed, a cryostat assembly was not needed.

2.6 SQUID

The SQUID (Superconducting Quantum Interference Device) magnetometer is the most sensitive device available for measuring magnetic moments. The measurement is performed by moving the sample through superconducting detection coils, which are located at the center of the superconducting magnet outside the sample chamber (Fig.2.7). Any change in the magnetic flux in the detection coils produces a change in the persistent current in the detection circuit. To be able to detect changes in magnetic flux with high sensitivity, a superconducting ring with one or two Josephson-contacts [23], also called „weak link“, is build in the detection circuit.
In the presence of a magnetic field, the magnetic flux Φ through a superconducting ring without „weak link“ will be quantized in terms of the elementary $fluxon$ $\Phi_0 = \frac{\hbar}{2e} = 2 \cdot 10^{-15}\mathrm{Tm}^{-2}$. This flux quantization will not happen if a josephson-contact is included in the circuit. The flux through the ring Φ_i will be the difference between the flux Φ_a produced by the external magnetic field, and the flux originated through the -according to Lenz law- induced current, as

$$\Phi_i = \Phi_a - LI_0 \sin 2\pi \frac{\Phi_i}{\Phi_0} \tag{2.5}$$

where I_0 represents the maximal or critical current of the Josephson-contact, and L the inductance of the ring. The current $I = I_0 \sin(2\pi \frac{\Phi_i}{\Phi_0})$ can be derived from the first Josephson-equation [11]. Detecting this current enables the use of a SQUID as a magnetometer.

Since the SQUID functions as highly linear current-to-voltage convertor, the variations in the current produce corresponding variations in the SQUID output voltage which are thus proportional to the magnetic moment of the sample. In a fully calibrated system, measurements of the voltage variation as the sample is moved through the detection coils provide a highly accurate measurement of the sample's magnetic moment. The system can be accurately calibrated using a small piece of material having a known mass and magnetic susceptibility.

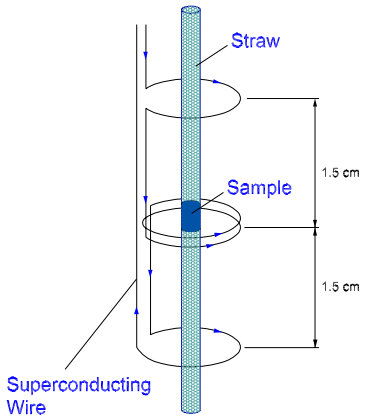

Figure 2.7: Sample position in a second-order derivative coil configuration.

The Quantum Design MPMS2 instrument used for the current sample characterization can be operated using fields up to 1 Tesla and measurements can be performed ranging from 1.7 to 320K. The system makes use of a second order derivative coil configuration to eliminate effects of stray fields. The sample chamber is at low pressure of helium gas, which provides thermal contact with a flow of gas outside the sample chamber pipe that is used to change and stabilize the temperature. Over 4.5 K flow impedance and a gas heater take care of the temperature control. The temperature is homogenized around the sample space by copper wires.

In order to measure the temperature dependence of magnetization M(T), two different kinds of measurements can be performed . In the zero-field-cooled mode (ZFC),

the sample is cooled down to 5K in absence of a magnetic field, but, while warming up to room temperature, a constant magnetic field is applied. On the other hand, in the field-cooled mode (FC), the sample is first cooled from room temperature down to 5K in the same magnetic field applied for the warm up scan, performed straight after the cooling. For the hysteretic loop M(H), the samples were subjected to a magnetic field cycling between +1 Tesla and -1 Tesla and the magnetization was measured at a particular temperature (typically for DMS magnetic characterization: 5 and 300K). In addition, a second SQUID-magnetometer (MPMS-XL) was used to measure the magnetic moments of the samples in a higher field range [-7T,+7T]. The temperature dependence of the magnetization M(T) was measured after quenching the field from 7T to 0T, which provides information about how the *remanent* magnetization develops with temperature in a ferromagnetic material.

2.7 Magnetotransport

Magnetotransport measurements were performed in order to analyze the temperature- and field dependence of thin film samples. A hall-structure was patterned in the surface of the film and contacted to the system electronics, before being placed in the cryostat and exposed to the measurement. The structured hall-bar enables the measurement of the hall-effect (Sec.4.2.5).

2.7.1 Sample treatment

The preparation of thin films for magnetotransport measurements, required four different process stages in the following order:

- Optical litography
- Ion beam etching
- Second optical litography process
- Sputtering with subsequently Lift-Off technique

The optical litography is a technique to provide a mask structure in a resist layer on the surface of the sample, via UV-light irradiation. For this purpose, an slide-projector technique was used to project the mask on the film surface. The light beam passing through the mask slide was focused through an optical microscope on the film surface. Before exposing the sample to the light, a thin layer of photo-resistive material (Photolack AZ5214i) was deposited on the film surface and distributed homogeneously by means of a centrifuge, to be finally heated at 107 C with a hotplate

to ensure a good sticking. The resist layer will chemically react to the UV-light, so that the exposed areas will be exempt from the resist layer after developing. The remaining areas with resist-layer will act as a protection of the sample surface while performing the next step of the structuring, the etching process. The masks used for the first and the second litography processes are shown in Fig.2.8. In the first process, the mask (a) will provide the structure with a hall-bar (vertical black bar in the middle of the sample), as well as rectangular-shaped areas connected to the hall-bar. The insulation of the contacts is achieved through the white areas in (a).

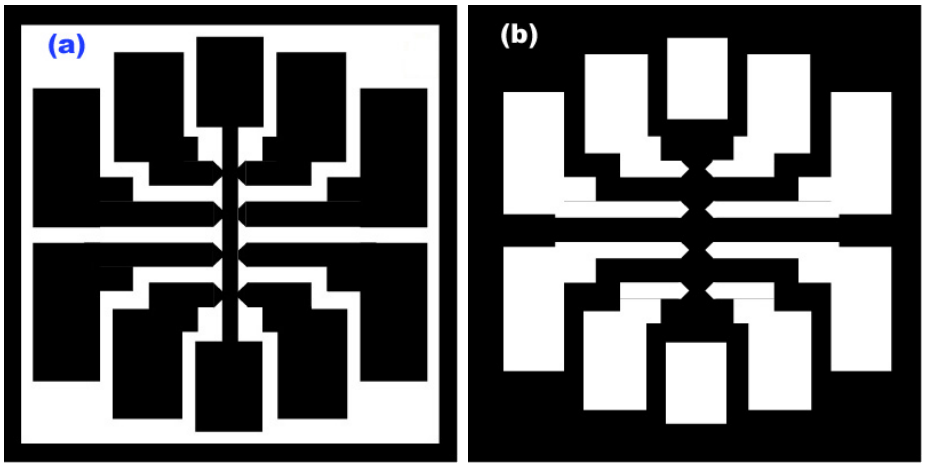

Figure 2.8: Masks used for the optical lithography process.

The ion-etching technique makes the use of an argon beam to etch the areas which were pre-selected via the optical litography. Since the resist layer is much thicker (1,5μm) than the sample thickness, the sample areas which are not protected by the resist will be etched completely by the argon beam, down to the substrate. After removing the resist-layer which act as protector in the etching process by immersing the sample in acetone, the sample area will be represented by the black areas in mask (a) in Fig.2.8, whereas the white areas will correspond to the substrate. The second litography process will be used to select the area where the contacts should be placed. For this purpose, mask (b) is used, and the optical litography process described aboved is repeated. The next step is to provide the sample with gold contacts, in order to minimize the contact resistance between the conducting wires and the film surface. A gold layer, 60nm thick, is deposited all over the surface by means of sputtering. The Lift-off process, the last step needed for the achievement of the aimed hall-structure, involves the immersion of the sputtered sample in an acetone bath for around 45min and its subsequently exposure to short pulses in an ultrasound bath. During the immersion of the sputtered sample in aceton, the gold layer deposited directly on the

sample surface will stick, while the gold layer deposited on the resist will „lift off“, as the resist disolves with time. After running this four steps systematically, the hall-bar with twelve gold contacts, is finally ready to proceed with the contact wiring. An optical microscope picture of a ready structure is shown in Fig.2.9.

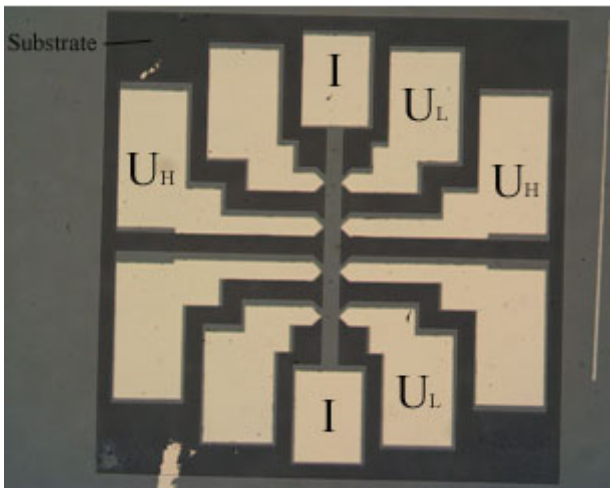

Figure 2.9: Optical microscope picture of a hall-bar, ready to be contacted. The rectangles at the top and the bottom of the bar are the contacts for the current feeding; the eight additional ones are used to pick up the voltage.

The dimensions of the hall-bar are 350μm x 45μm. Apart from the current contacts located at the top and the bottom of the bar, only four contacts are needed to pick up the voltage: two for the voltage U_L parallel to the current, and two for the voltage U_H perpendicular to the current (hall-configuration). As described in the photolithographical and etching process, the contacts will be insulated through the darkest regions in the picture (Fig.2.9), corresponding to the substrate. Therefore, the choice of an insulating substrate for this measurement should be strongly taken into consideration.

2.7.2 Measurement Set-Up

Before proceeding to the aimed magneto-transport measurements, the hall-structures described in the last section, have to be mounted and contacted in the measuring stick which is inserted in the cryostat. A copper carrier is used to place up to four samples with the respective amount of contact pads needed for the measurement. Each sample need typically six bond pads, two to drive the current across the hall-bar, and four to measure the parallel- and hall-voltage. The contact between sample surface and bond pads was achieve by means of a bonder (FK Delvotec), which connected both surfaces through thin aluminium wires (d=30μm). At the other side of the bond frames, bond

pads with a bigger area were used to sold copper wires, which actually connect the bond pads with the channels which lead to the current sources and voltmeters. The set-up is sketched in Fig.2.10.

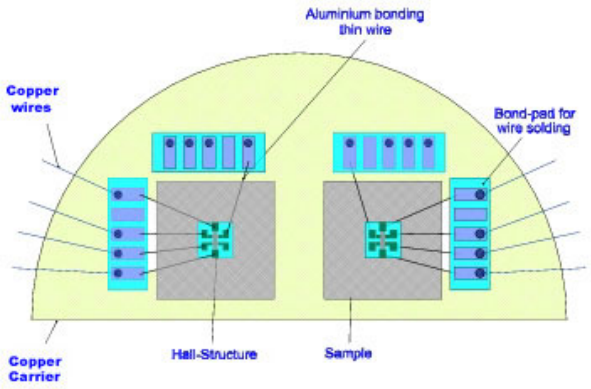

Figure 2.10: Contact and wiring scheme of the Hall-structures, before being mounted in the cryostat.

The measurements were performed in a cryostat of the company Oxford. The superconducting magnets present in the system could deliver a field up to 17T, while the temperature range could be varied in both directions from 1,4K to 400K. For voltage detection and current delivery, a Keithley 2010 Multimeter and a Keithley 2400 current source were available. The temperature and field control, as well as the measurement itself, could be programmed and monitored via PC-software (Labview).

3. Sample Preparation

In this chapter, the preparation of bulk materials and thin films of Cu-doped ZnO is described, as well as an overview of the samples submitted to characterization.

3.1 Polycrystalline Bulk-Materials

The bulk materials were prepared by standard solid-solid reaction method. Appropriate amount of precursors (ZnO and CuO - Alfa Aesar) were mixed and ground properly in order to obtain sub-micron sized precursors. The mixture was then calcined in air for 8h. The obtained calcined powder was pressed to form dense pellets and sintered at temperatures ranging from 500°C to 800°C in air atmosphere. The obtained pellets were further characterized in order to find out their physical, structural, and magnetic properties, before being ablated for thin film production.
Bulk ZnO:Cu pellets with Cu- atomic concentration of 2, 4, and 6% have been prepared. The sintering temperature of the material has an influence on following aspects:

- the diffusion of the Cu-dopant in the host semiconductor ZnO;
- the formation of secondary phases;
- the final density of the pellet.

The role of the sintering temperature on the structural and magnetic properties has been investigated, at bulk materials with different Cu-concentrations. The results are discussed in the next chapter.

3.2 Thin Films

In the present work, the sample preparation and characterization focused on $Zn_{0.98}Cu_{0.02}$ O thin films, which were grown by means of the Pulsed Laser Deposition (PLD) technique (Section 2.1). Before placing substrate and target in the vacuum chamber, one has to be sure that they are free of any kind of impurities. The target surface has to be polished and the substrate has to be subjected to a very careful cleaning process in ultrasonic bath, divided into three steps:

- 30 min in a soap solution of special detergent for thin film work (Decon) in DI-water
- 15 min in acetone
- 15 min in isopropanol, to get rid of the acetone leftovers

After the cleaning process, the substrate is dried by means of high purity nitrogen gas, before being placed in the vacuum chamber. The substrate is mounted onto the heating block, using conductive silver as an interface for good thermal coupling as well to hold a stable position of the substrate during deposition.
All the film samples were grown on R-cut Al_2O_3 (sapphire) substrates, with crystallographical c-axis orientation, a surface area of 4 × 5 mm, and a thickness of 0,5mm. Sapphire crystallizes in wurtzite structure, property that qualifies it as a substrate candidate for the growth of ZnO thin films. There is, however, a lattice mismatch regarding the a axis corresponding to the values of ZnO, which will have influence on the crystalline properties of the thin film samples. This issue will be discussed in the next chapter, when presenting the structural analysis of the thin films by means of X-ray diffraction (Section 4.2.1). An overview of the properties of ZnO and Al_2O_3 is shown in Table 3.1.

	ZnO	**Sapphire**
Stable phase	wurtzite	wurtzite
Lattice constant a at 300K (nm)	0.325	0.475
Lattice constant c at 300K (nm)	0.531	1.297
Melting point	1975°C	2040°C
Thermal expansion coefficient(/C°)	3.0×10^{-6}	5.8×10^{-6}
Density (g/cm^3)	5.606	3.98

Table 3.1: Properties of ZnO vs Al_2O_3

The present work will concentrate on ten thin film samples, from which four of them were reproduced but with a greater thickness (series „R“), as seen in Table 3.2. The role of substrate temperature, background gas type, and pressure during the film growth were particulary investigated. Laser parameters were kept constant for the preparation of all the samples: the laser energy was kept at 200mJ/pulse, yielding an energy fluence of 2 J/cm^2, and with a pulse frequency of 5Hz. Other common features of the sample series are the use of the same target, with 2% copper concentration, and the substrate charge.

Sample	$\mathbf{T}_{sub}$ [°C]	**Pressure** [mbar]	**Background gas**
AR 1	450	1 x 10^{-2}	Ar
AR 4	300	1 x 10^{-2}	Ar
AR 1R	450	1 x 10^{-2}	Ar
AR 4R	300	1 x 10^{-2}	Ar
OX 1	450	1 x 10^{-2}	O_2
OX 3	300	1 x 10^{-2}	O_2
OX 1R	450	1 x 10^{-2}	O_2
OX 3R	300	1 x 10^{-2}	O_2
OX 5	500	5 x 10^{-2}	O_2
OX 7	650	5 x 10^{-2}	O_2

Table 3.2: Overview of samples which have been characterized in the present work.

4. Experimental Results and Discussion

The present work will concentrate mainly on the characterization of Cu-doped ZnO thin film samples. However, the characterization of bulk materials should be also taken into consideration, especially if the thin films are grown by means of the PLD-technique. Unlike other growth techniques, where the doping of dilute magnetic semiconductors does not happen until the in-situ reaction of the precusors in the growth chamber (MBE,Sputtering), the PLD-technique deals with the transfer of materials from a target to a substrate (Section 2.1), and hence the doping process has to be already considered in the target preparation. Therefore, the characterization of bulk samples will provide useful information which could help to have a better understanding of the ZnO:Cu system.

4.1 Polycrystalline bulk materials

The characterization was performed by means of X-ray diffraction and vibrating sample magnetometry (VSM). Since the bulk materials were pelletized and further used as targets for the thin film preparation, it is of advantage to be aware of the physical properties of the „sources“ for film preparation. First of all, the density of the target will play a crucial role on the production of thin films by means of PLD. It should be sufficiently high to ensure a homogeneous transfer of particles between target and film. Less dense targets will thus not stand typical laser energies and promote the formation of particulates during film growth. Regarding the sample preparation, the parameter which has a dominant influence on the physical properties of the bulk materials, is indeed the sintering temperature. Apart from tuning the density, the sintering temperature, which typically lies above 500°C, will control the rate of diffusion of the Cu-dopants in the host ZnO, due to the thermal energy given to the system. Thus, the proper choice of sintering temperatures will enable the preparation of Cu-doped ZnO targets with an homogeneous dopant distribution. In the following sections, the role of the sintering temperature and Cu-concentration on the structural and magnetic properties of the bulk materials will be discussed.

4.1.1 X-ray Diffraction

From the structural point of view, a preferred crystalline orientation will not be expected. The aim of x-ray diffraction characterization is thus to identify the phases which are present in the bulk material. Since the Cu-doping is achieved by adding CuO and mixing it with the ZnO powder, unreacted CuO precursors could be present after the diffusion process. Starting with the lowest Cu-concentration which has been investigated (2%), the XRD-patterns show still unreacted CuO $(11\bar{2}1)$ at low sintering temperatures. Increasing the sintering temperature to 700°C will favour the diffusion and more Cu-atoms will be introduced in the ZnO matrix. Fig. 4.1 shows the ω-2θ-scans of ZnO:Cu bulk pellets processed at different sintering temperatures.

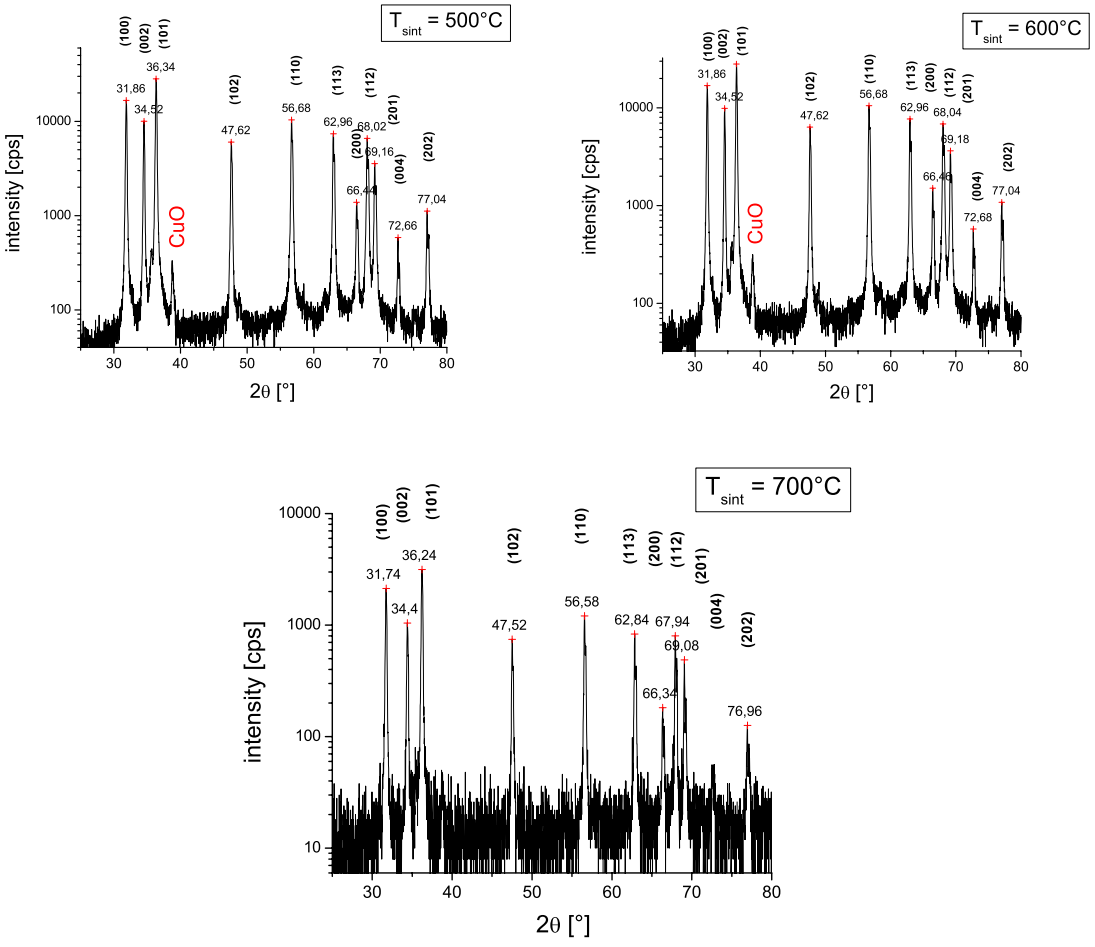

Figure 4.1: X-ray diffraction patterns of bulk Cu-doped ZnO (2%). The labeled peaks belong to ZnO. A small CuO peak is observed at 500 and 600°C sintering temperature.

At a nominal concentration of 2% Cu, the best results were obtained at T_{sint}= 700°C. Following this result, the preparation of the next set of pellets (4%) was done using

high sintering temperatures, since a higher Cu-concentration may increase the risk of having more unreacted CuO. However, CuO was not only detected at low process temperatures, as observed in Fig.4.2.

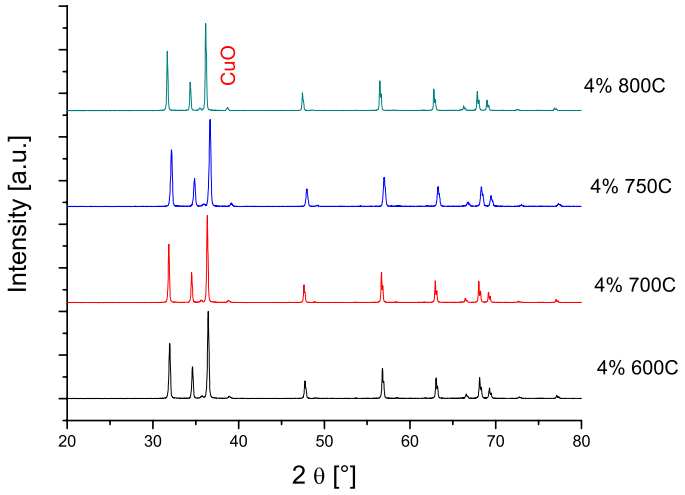

Figure 4.2: X-ray diffraction patterns of bulk ZnO:Cu (4%). Note that the $(11\bar{2}1)$-CuO peak is observed even at high sintering temperatures.

A last set of pellets with 6% Cu was prepared and submitted to XRD-characterization. Similar results as in the case of 4% doping were obtained, since unreacted CuO was present in the samples. However, the peak intensity of the unreacted CuO is weaker at higher sintering temperatures, which means that T_{sint} still favours the diffusion and inclusion of the Cu-dopants in the host ZnO matrix, as observed in Fig.4.3.

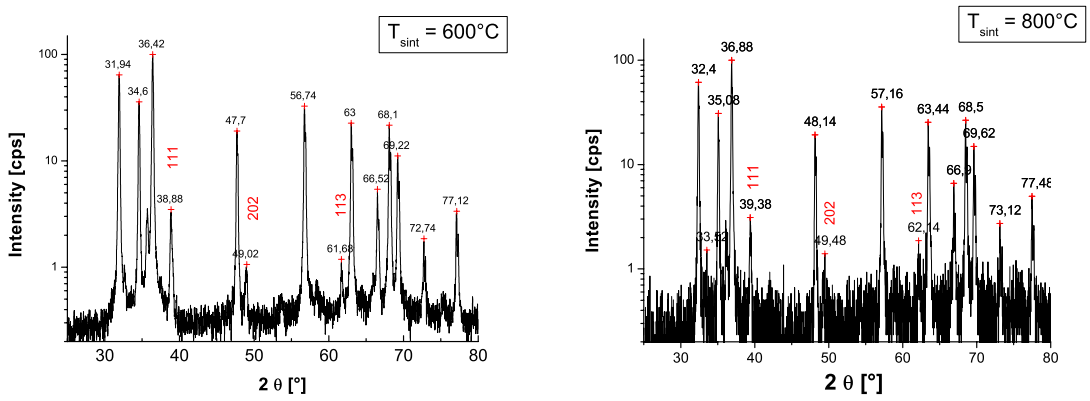

Figure 4.3: X-ray diffraction patterns of ZnO:Cu pellets with 6% Cu-concentration. CuO peaks are highlighted in red.

As a result, the solubility of Cu in the ZnO matrix was not as high as expected, since there was evidence of unreacted CuO for 4% and 6% nominal doping. The samples sintered at higher temperatures tend to have less unreacted precursors. An optimal result could be found at T_{sint} $\geq$700°C and at a nominal concentration of 2 atomic percent copper.

4.1.2 VSM-Magnetometry

Another interesting aspect when characterizing bulk DMS materials, is to investigate if they show room-temperature ferromagnetism already in the bulk form. Again, the role of sintering temperature, the most important parameter when processing bulk materials by the solid-solid reaction technique, should be studied. For that purpose, the field dependence of the magnetization was measured up to a field of H=7000Oe $\cong$ 0,7T. All the measurements were performed at room temperature. At 2 % Cu-concentration, a ferromagnetic hysteresis was evidenced, as observed in Fig.4.4.
The saturation moment in the samples with 2% Cu-concentration was estimated to be around 0,025 μ_B/Cu^{2+} at 0,7 Tesla, after substracting a diamagnetic contribution of the form

$$M_{dia} = -c \cdot H \tag{4.1}$$

which comes from ZnO, known to be a diamagnet[22]. Both coercivity and remanence were found to be clearly higher at 500°C sintering temperature, while the saturation moment did not show much change. Fig.4.5 shows the evidence of ferromagnetic hysteresis at room temperature.

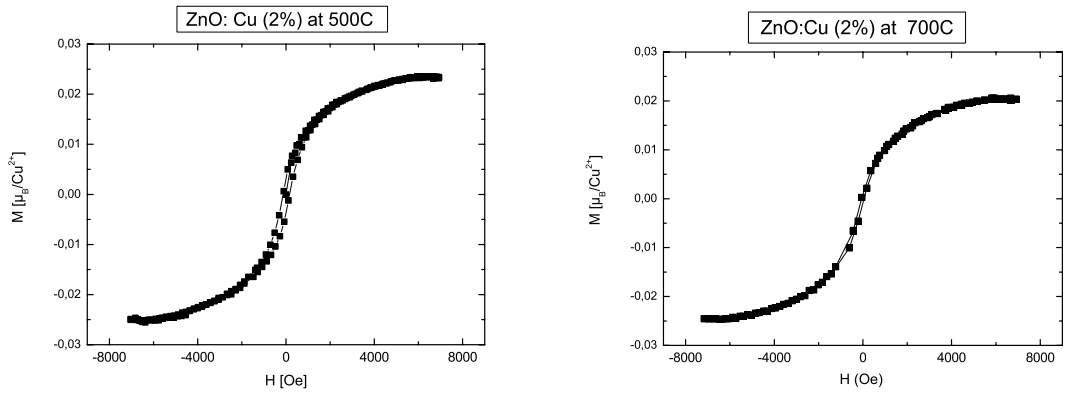

Figure 4.4: M(H) hysteresis loop of ZnO:Cu(2%) in the bulk form, at room temperature. The saturation at low fields and the hysteretic behaviour suggest ferromagnetic ordering, both at 500°C and 700°C sintering temperature.

The low moment values obtained were detectable with the VSM-technique with a good resolution, since the amount of material was quite large (≈2g). It is worth to mention that the VSM used for these measurements is able to detect absolute magnetic moments of 1 x 10^{-5}emu with good resolution. That means, the analysis of thin films of dilute magnetic semiconductors with VSM-magnetometry (≈ 1 x 10^{-4}g for a 1μm thick film) is not adequate.

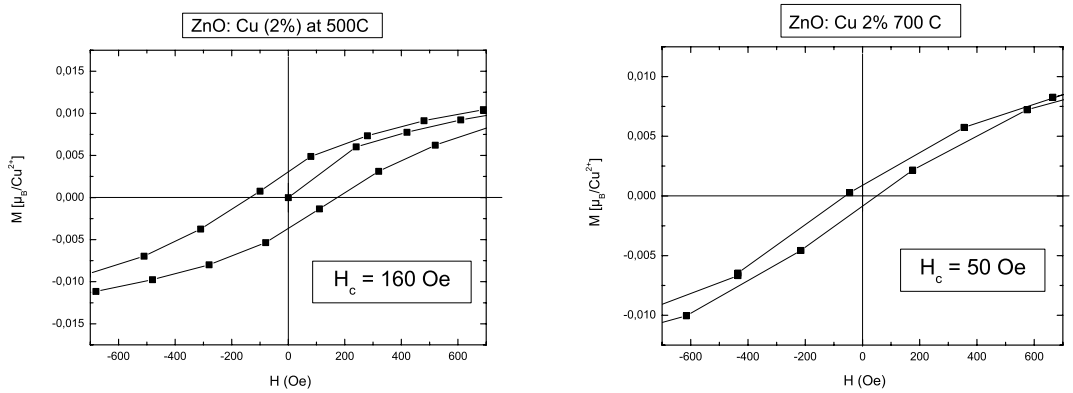

Figure 4.5: M(H) behaviour at low fields, showing the decrease of remanence and coercivity with increasing sintering temperature.

The characterization of the 4% batch, processed at high temperarures, showed a decrease of the coercivity with increasing sintering temperature. The saturation moments did not show a major change, as depicted in Fig.4.6. A ferromagnetic hysteresis

could be still evidenced at the sample sintered at 700°C.

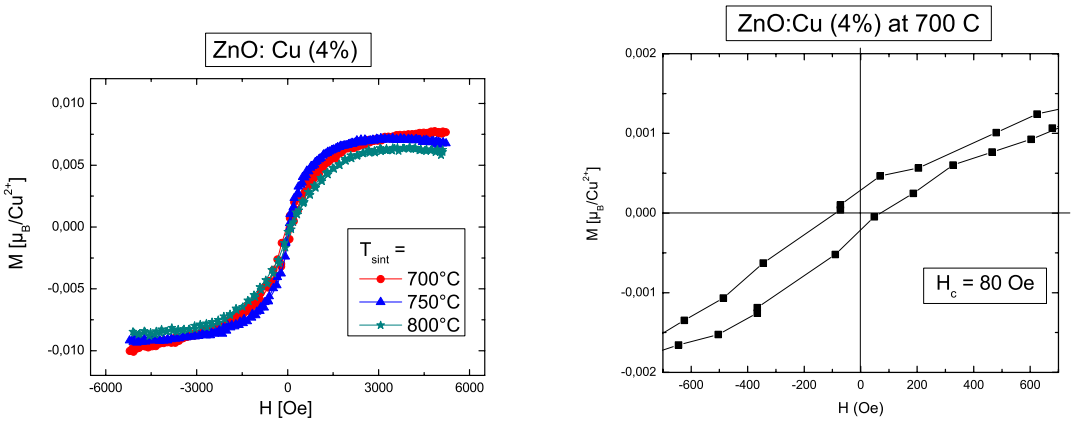

Figure 4.6: Room tempertaure M(H) behaviour of the ZnO:Cu(4%) batch. The hysteresis at low fields for the sample with T_{sint}=700°C is evidenced.

The remanence and the coercivity at the 700°C sintered sample with 4% Cu-concentration is slightly higher than the one with 2% Cu, but still in the same order of magnitude. The fact, that high sintering temperatures decrease the coercivity and the remanence, was confirmed by measuring the 6% batch. Again, a ferromagnetic hysteresis was evidenced at T_{sint}=600°C but not at 800°C. The M(H) loops are depicted in Fig.4.7.

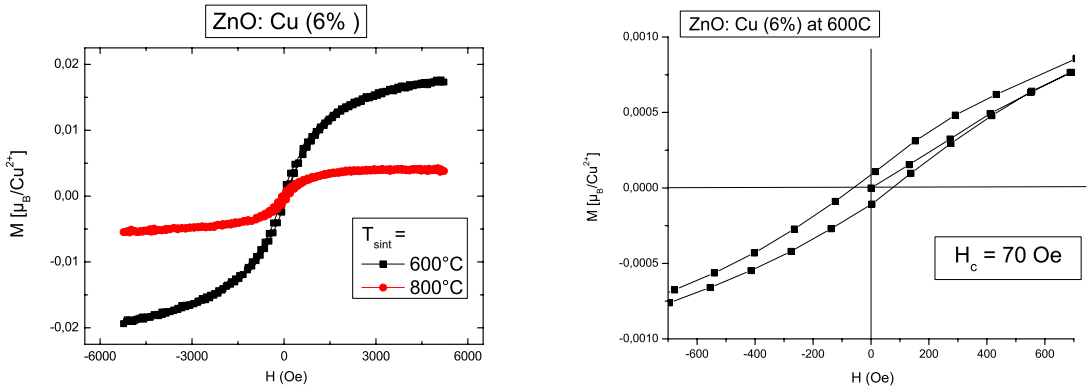

Figure 4.7: M(H) measurements of the ZnO:Cu(6%) batch, at room temperature, confirming the role of the sintering temperature on the coercivity of the bulk materials.

There are no reports up to now, which deal with the magnetic characterization of polycrystalline Cu-doped ZnO materials. However, the fact that the appearence of ferromagnetism in bulk DMS materials is highly sensitive to the process parameters, is

a known issue [4, 7]. According to the presented results, the best magnetic properties were found at relative low sintering temperatures. However, the presence of unreacted CuO, even at 2%, was detected in the pellets processed at those temperatures (500°C,600°C). CuO is known to be antiferromagnetic [22], so that a possible weak contribution will only arise if the moments are not aligned exactly in an antiparallel way (canted antiferromagnetism). Still, the samples which show room-temperature ferromagnetism and no secondary phases, will be a better choice. Another point to take into consideration is the pellet density, which has to be sufficient to stand high-power laser pulses without enabling the formation of particulates which could deteriorate the film growth. The density scales with the sintering temperature, as shown in Fig. 4.8. Taking into account all these facts, the optimal sintering temperature has been found to be T_{sint}=700°C, yielding a good density and showing still a ferromagnetic hysteresis at room-temperature.

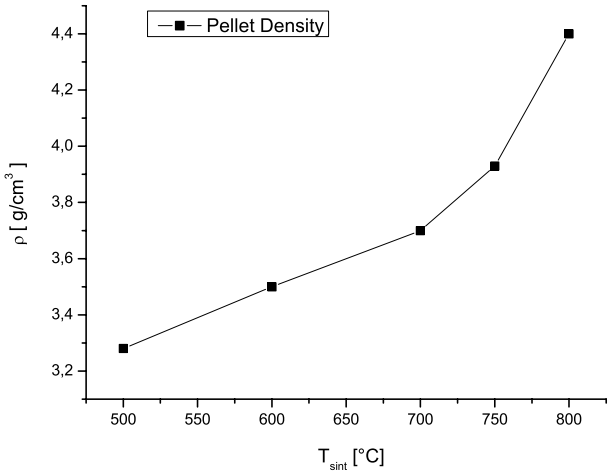

Figure 4.8: Role of T_{sint} on the density of the bulk ZnO:Cu targets.

Summarizing, room-temperature ferromagnetism was observed at Cu-doped ZnO bulk samples by means of VSM-Magnetometry, after appropriate choice of the preparation conditions. The solubility of the Cu-dopants in the host ZnO matrix was optimal at low copper concentrations (2%), and at high sintering temperatures. The density of the pellets was also improved by increasing the sintering temperature. However, processing the materials at high temperatures supress the ferromagnetic properties, producing a decrease in coercivity and remanence. According to these results, the optimal conditions for preparation of bulk ZnO:Cu targets was found at 2% Cu-concentration and 700°C sintering temperature. These parameters were taken to

prepare PLD-targets for thin film deposition. Under these process conditions, the absence of secondary phases could be evidenced, which implies that the observed room-temperature ferromagnetism is only due to the incorporation of Cu-precursors in the ZnO host matrix, since both ZnO and Cu are not ferromagnetic materials.

4.2 Thin Films

4.2.1 X-ray Diffraction

The structure of the ZnO:Cu thin films has been analyzed by means of x-ray diffraction. ω-2θ scans have been performed to identify the present phases and to determine the orientation of the crystal structure. Rocking curves have been measured in order to quantify the mosaicity of the samples. The latter is an important characterization step especially in this case, when substrate and film have a lattice mismatch in the structure (see Tab.3.1). Phi-scans have been also performed to check if the ZnO:Cu thin films crystallize in hexagonal structure.

Before starting with the characterization, the samples have been submitted to a plane alignment, taking the substrate plane as reference. This prior alignment is absolutely necessary, since the substrate surface plane is usually canted in relation to the horizontal diffraction plane. For this purpose, a rocking-curve around the substrate reflection, in this case the (0006) peak of sapphire, has been measured to find its exact location. The literature value of the peak was taken as a reference, in order to find out an eventual offset.

All the samples prepared in this work, regardless of their deposition conditions, show a crystallographic c-axis orientation, where the (0006)-reflection of the substrate and the (0002)-reflection of the film could be well identified. Fig 4.9 shows a typical ω-2θ-scan of a Cu-doped ZnO film grown on sapphire.

Another common feature is that all the Cu-doped ZnO thin films show the absence of secondary phases like metallic Cu, or copper oxides compounds like CuO or Cu_20. However, the location of the main ZnO reflection (0002) and hence the c-axis parameter varies from sample to sample, depending on the growth conditions. Table 4.1 show the obtained c-axis parameters through the bragg-equation (2.1). Since all the samples have been grown using the same target, it is expected that the copper concentration in the films (2 atomic percent) is nearly equal. Assuming that a similar amount of Cu-atoms will subsitute the Zn-atoms in the host lattice, so that the effect of the copper substitution on the c-axis parameter will be the same, the copper concentration will be not responsible for the discrepancies in the c-axis values from sample to sample. Copper has a covalent radius of 138pm, and an ionic radius of 87pm in its Cu^{2+}-state. Both radii are greater than the host Zn values (125pm/73pm), so

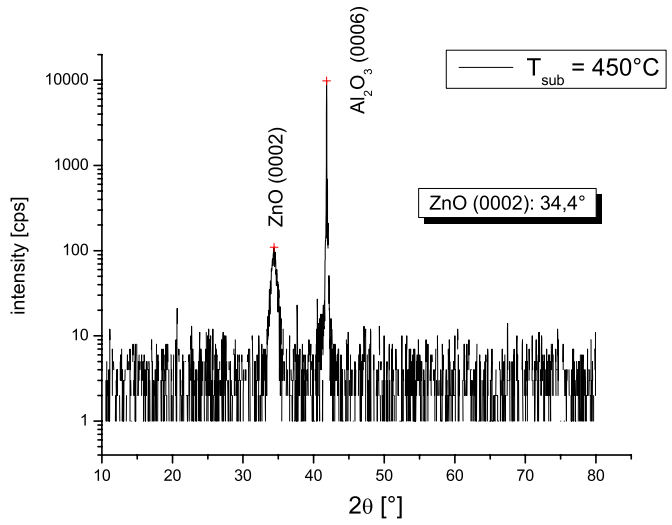

Figure 4.9: ω-2θ scan of sample AR1, deposited at T_{sub}=450°C. Both film and substrate peaks could be well identified.

that the lattice will suffer an enlargment along its axes. The c-axis constant calculations suggest an inclusion of the Cu^{2+}-atoms in the host lattice, since all the measured c-axis constants lie above the one from pure ZnO (0.5206nm). However, as observed in the c-axis parameter values the distortion will be very weak, since the doping is in the dilute level.

Sample	(0002)-peak [2θ]	c-axis parameter [nm]	T_{sub}[°C]
AR 1	34,40	0.5208	450
OX 1	34,33	0.5218	450
AR 1R	34,39	0.5209	450
OX 1R	34,38	0.5211	450
AR 4	34,13	0.5248	300
OX 3	34,21	0.5236	300
AR 4R	34,14	0.5246	300
OX 3R	34,20	0.5237	300

Table 4.1: Location of (0002)-peaks and c-axis parameters of Cu-doped ZnO thin films. Note that the samples could be divided in two groups, one having the c-axis around 0.524 and the other around 0.521nm. The common feature of each group is the substrate temperature T_{sub}.

Interestingly, the substrate temperature seems to have a crucial influence on the c-axis constant, independently of other process parameters like background gas and

pressure. At 300°C, the largest stretching factor of the c-axis constant is $\Delta c = \frac{c-c_0}{c_0} = 1,52$, while for 450°C the c-axis constants lie very close to unsubstituted ZnO. This observation suggests that ZnO:Cu films grown at higher temperatures will tend to crystallize with less disorder and strain. The high temperatures ($\geq$ 700°C) used to grow high-quality crystalline films of undoped ZnO on sapphire [24], support this empirical observation. It is worth to mention, however, that films grown in Ar and O_2 atmosphere have a small shift in the (0002) c-axis reflections, which lead to a c-axis parameter shift of around 1pm. The substrate temperature has still a dominant influence.

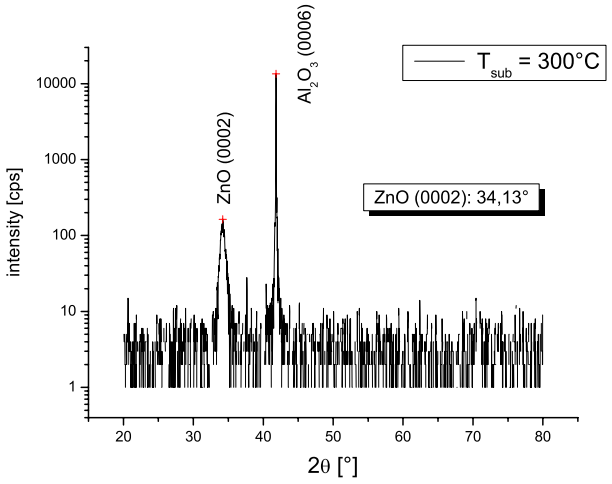

Figure 4.10: ω-2θ scan of sample AR4, deposited at T_{sub}=300°C. The (0002)-peak of ZnO is shifted 0,3° in comparison to sample AR1, grown at T_{sub}=450°C, and otherwise identical conditions.

The choice of sapphire as a substrate is on the one hand favourable for structural characterization, since the (0002)-peaks of ZnO can be clearly observed (see Fig.4.9 and 4.10) thus enabling a more precise analysis of the lattice parameters, in contrast to doped ZnO films deposited in ZnO substrates, where is difficult to distinguish the substrate and film reflections. On the other hand, the use of ZnO-substrates will support quasi-epitaxial growth, since there is no lattice mismatch between substrate and film, while for sapphire the mismatch in the a-b plane is about 18 %[25]. Although the growth can be c-axis oriented by choosing the proper growth conditions, the film will always posess a mosaicity, which means that the crystal planes are tilted in relation to each other. Diaconu *et al.*[26] found that Mn-doped ZnO thin films on sapphire, tend to grow in a columnar structure, hence showing a mosaicity which depends on the column diameter. In [26], the columnar structure was visualized, in

addition, by cross-sectional TEM (Transmission Electron Microscopy) imaging. The presence of straight dislocations, aligned parallel to the c-axis, as well as mixed-type dislocations in the vicinity of the substrate-film interface, could be evidenced. For the present work, TEM faciliites were not available, but the rocking curves of the samples showed for moderate substrate temperatures a FWHM around 2,5°, confirming the mosaicity of ZnO when deposited on sapphire substrates, as observed in Fig (4.11).

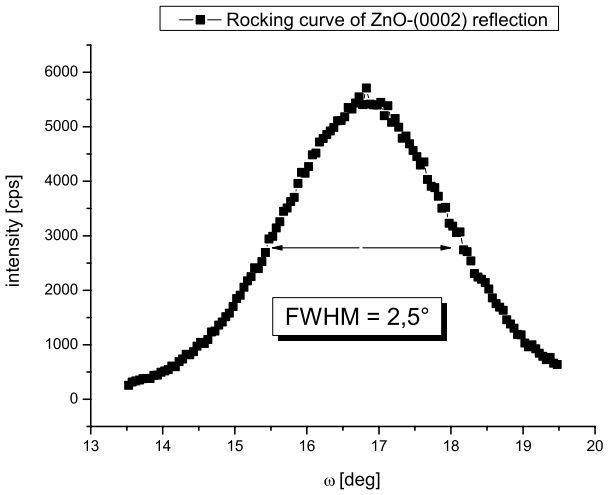

Figure 4.11: Rocking curve of ZnO:Cu film deposited at T_{sub}=300°C on sapphire.

The FWHM of the rocking curves lie typically between 2 and 2,5° for samples grown at T_{sub}=(300°C, 450°C). The mosaicity decreases with increasing substrate temperature, reaching a lowest FWHM value of 0,6° for films deposited at 650°C. Wakano *et al*. [27] found a drastical decrease around 500°C in the FWHM of Ni-doped ZnO films deposited at temperatures ranging from 300°C to 700°C, behaviour which is in agreement with our results. In the standard ω-2θ scans, a similar trend could be observed: the FWHM of the (0002) peak of ZnO was found to be lower at high temperatures, indicating better crystallinity [25]. Figure 4.12 shows the influence of the substrate temperature on the mosaicity of the samples.
Since the structural characterization results presented here match with the crystallinty studies of ZnO thin films doped with Mn[26] and Ni[27], it can be concluded that the dopant itself does not play a crucial role on the crystalline properties of the material, as the choice of the substrate does.

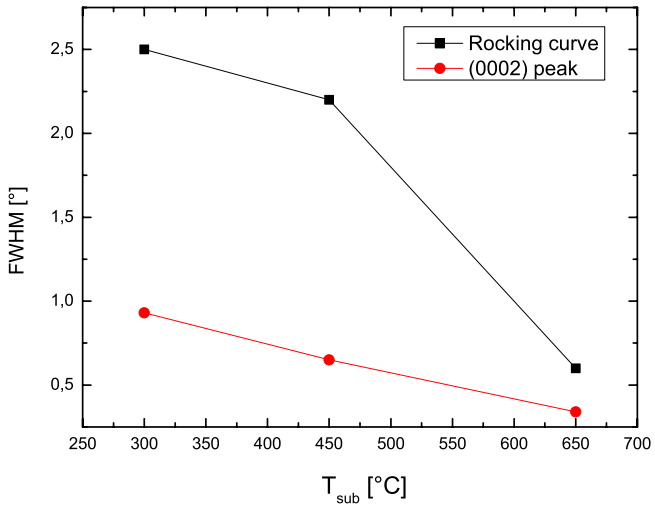

Figure 4.12: Role of substrate temperature on the crystalline properties of Cu-doped ZnO thin films deposited on sapphire. FWHM values of the rocking curves, as well as of the main (0002) ZnO reflection in the ω-2θ scan, decrease with increasing growth temperature.

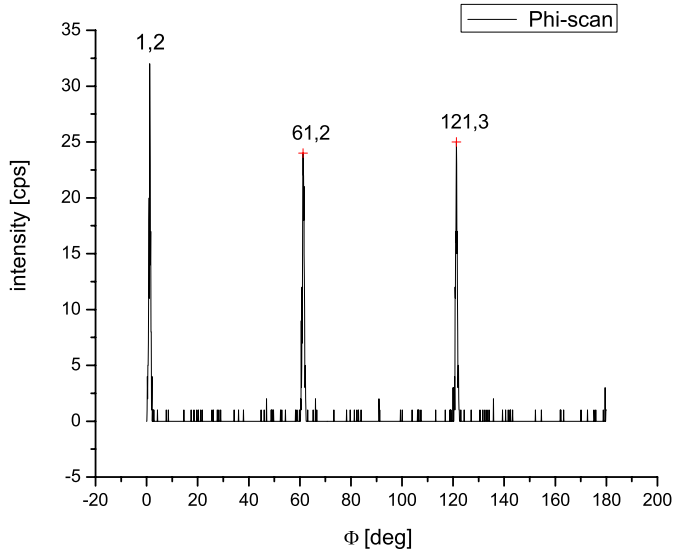

Figure 4.13: Typical Phi-scan of ZnO:Cu thin films at the $(2\bar{1}\bar{1}1)$-plane. The peaks are slightly shifted, but the 60° periodicity is clearly observed.

The hexagonal structure of Cu-doped ZnO thin films could be verified by Phi-scans, by rotating the sample from 0 to 180° in the $(2\bar{1}\bar{1}1)$-plane. The intensity reflexes, as observed in Fig 4.13, are detected in regular steps of 60°, near 0°, 60°, and 120°, respectively, confirming that the samples have indeed crystallized in wurtzite structure, as expected from ZnO-crystals.

4.2.2 X-ray Reflectometry

For the determination of several important material properties, such as resistivity or magnetization per atom unit, an accurate knowledge of the sample dimensions is required. In the case of thin films, the surface dimensions are already well-determined through the substrate area, so that thickness determination becomes very important. The X-ray reflectometry (XRR) technique has been used to determine the thickness of the samples with t$\leq$ 200nm, with a resolution up to 0,1nm for samples which show interference fringes in a bigger angular range. In addition, making profit of all the advantages of the XRR technique, values for surface roughness and film density have been estimated.

Sample	Pulses	Thickness [nm]	Roughness [RMS]	Density (g/cm^3)
AR 1	1200	18,2	1,31	5,33
AR 4	1800	37,4	0,22	5,38
OX 1	1800	32,4	1,70	5,36
OX 3	1800	34,1	2,13	5,32
OX 5	1800	31,7	2,62	5,45
OX 1R	3600	58	2,32	5,73
AR 1R	5400	103	3,56	5,28
OX 3R	5400	90	2,68	5,35
AR 4R	9000	180	3,9	5,62

Table 4.2: Thickness, roughness and density values of ZnO:Cu thin films, listed with increasing pulse number. The labels AR and OX correspond to the background atmosphere used during growth.

How to determine thickness, and estimate roughness and film density from a typical XRR-plot is explained in section (2.2). The most representative sample plots will be shown to elucidate the differences between thick and thin, rough and smooth, and

dense and less dense thin films. The latter will be more difficult to show since the estimated density of the samples lie in a narrow range (see Table 4.2)
Since the frequency of the oscillations and the decay in the measured intensity will determine the thickness and the roughness, respectively, the results are plotted in the same angular and intensity range: from 0,5° to 3° in 2θ, and from 0.1 to 10^6 in intensity counts, to enable a faster and more clear comparison. The inset in Fig.4.14 shows the range where the oscillations take place at higher angular resolution. Since the samples AR 1 and AR 4R have a thickness ratio of 1:10, it would be expected that the oscillation period has the same dependence. The periods which could be estimated from the plots are

$$\Delta\theta(AR1) = 0,36^\circ \tag{4.2}$$

$$\Delta\theta(AR4R) = 0,03^\circ \tag{4.3}$$

which have a ratio of 1:12. This discrepancy can be understood taking into consideration following relation

$$d = \frac{\lambda}{2}\frac{1}{\sqrt{\theta_{m+1}^2 - \theta_c^2} - \sqrt{\theta_m^2 - \theta_c^2}} \approx \frac{\lambda}{2}\frac{1}{\theta_{m+1} - \theta_m} \tag{4.4}$$

where the last approximation, which implies a linear dependence between oscillation period and thickness, is only valid for $\theta_m \gg \theta_c$. In order to get this linear dependence, one has to consider the oscillations which are further away from the critical angle θ_c, the angle where the intensity drops for the first time. This is, in fact, a difficult task, since the oscillations will be „lost“ with increasing scan angle, due to diffuse scattering produced by surface and interface roughness. Therefore, the calculations were performed by means of a simulation software, taking into account equation (4.4) to ensure an accurate thickness determination.

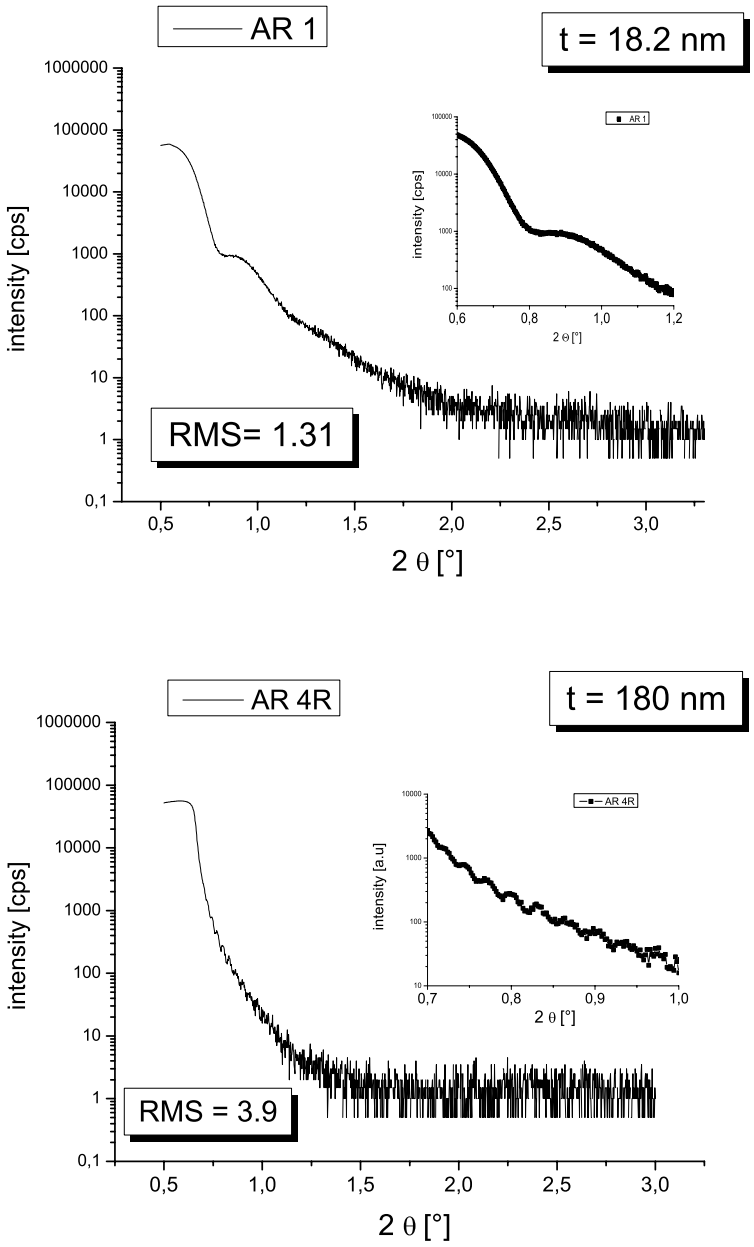

Figure 4.14: XRR-scans of samples AR 1 and AR 4R, which represent the extreme cases (thinner and thicker), respectively. Thickness and roughness values are shown in the plots, as well as the oscillations in a zoomed scale.

Samples AR 1 and AR 4R are indeed representative, since their thickness lie near the detection capability of the XRR-technique. Below 15nm, the oscillation period will be so long that it could hardly be detected with a typical intensity decrease (roughness), and, on the other hand, a sample with thickness greater than 200nm will have very short oscillation periods, being hard to distinguish within the measurement resolution. Surface roughness, is also a quantity which can be estimated with good accuracy, since it produces diffuse scattering and has a big impact on the intensity decay: having a quick look on the intensity behaviour in the measured scans is enough to determine qualitatively which samples are smoother than others. In the case of sample AR 4R, the measured intensity will decrease very fast: above 1° the interference fringes could not be further detected, and around 1,3° the total intensity decreases under 5 counts, falling in the measurement detection limit. Therefore, a high roughness RMS-value is expected (=3.9). For AR 1, the collapse of the total intensity happens around 2°, and the estimated RMS-value of 1.31 agrees with the observable intensity behaviour. In order to bring an example of a very smooth film, the XRR-scan of sample AR 4 is shown in Fig(4.15).

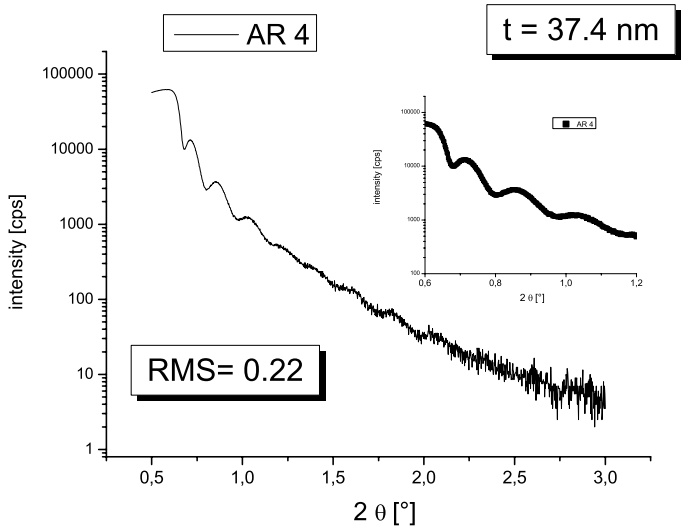

Figure 4.15: XRR-scan of the smoothest sample AR 4. Note that the oscillations appear in a bigger angular range.

As it can be seen from Fig (4.15), the oscillations can be detected up to 2,2°, and the intensity shows a slower decay, falling first around 3,0° into noise signal. To elucidate the impact of the film density on the intensity of the XRR-signal, samples AR 1R (5.28 g/cm^3) and AR 4R (5.62 g/cm^3), are shown in one plot (Fig 4.16).

As mentioned in section (2.3), the film density will depend on the critical angle θ_c: a higher critical angle will imply a higher density. Both roughness and density calculation were performed by software analysis.

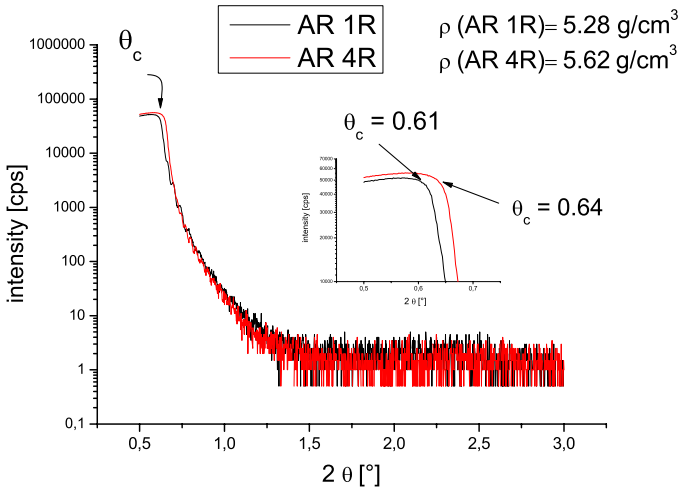

Figure 4.16: XRR-scan of samples AR 1R/AR 4R, which show a different critical angle θ_c and thus a different density.

The role of growth parameters on the roughness of the samples has been investigated. At low pulse numbers, samples grown in Ar seem to have a smoother surface than the ones grown in oxygen, fact which could not be confirmed when increasing the pulse number. The roughness seems to be rather thickness dependent, since for the samples grown in Ar, the highest values by far were found at thicknesses greater than 100nm (Table 4.2). In addition, comparing sample AR 4 with AR 4R, grown under identical conditions but with different thicknesses, AR 4R (t=180nm) is almost 20 times rougher than AR 4 (t=37.4nm). Considering that ZnO films grown on sapphire have a columnar structure and posess a mosaicity, the higher average roughness can be explained in terms of increasing column diameter [26, 28]. Kishimoto et al.[28] studied the strucutral and morphological properties of undoped ZnO as a function of thickness, and found that the column diameter increased with thickness, as the samples which are not in the early stage of growth tend to form bigger grains. This fact is in agreement with the high roughness values obtained for the samples AR 1R (103nm) and AR 4R (180nm).

4.2.3 Energy dispersive X-ray analysis(EDX)

The aim of the sample characterization through Energy Dispersive X-ray Analysis was the determination of the copper concentration in thin film samples. The stochiometrical transfer between target and film, known as one of the advantages of the PLD technique, should be confirmed. Since the EDX-method identifies the elements by detecting their characteristic x-ray radiation, only samples with thicknesses over 200nm could be analyzed with reasonable accurracy. The x-ray radiation, in contrast to the secondary and backscattered electron radiation, is not produced near the surface of the specimen. In the Scanning Electron Microscope (SEM) described in Section (2.4), the secondary electrons used for imaging are produced close to the surface to analize the topography, while the characteristic X-ray radiation used to quantify the chemical composition is produced deep in the sample. For films thinner than t≥200nm, the collected x-ray radiation will be rather from the substrate, thus producing an enormous error margin. Due to this fact, only three samples could be investigated. Table 4.3 shows the copper concentration for the films with thicknesses around 1μm.

Sample	Cu-concentration (%)
WMI 03	2,19
WMI 05	1,76
WMI 08	2,35

Table 4.3: EDX-results for samples with a thickness around 1μm.

Since the thickness of this set of samples could not be determined by X-ray reflectometry, cross sectional-SEM imaging was used as an alternative, as observed in Fig (4.17). However, cross sectional SEM-imaging will loose accuracy as the film thickness decreases. Therefore, using the appropriate technique for a given thickness range will enable the thickness determination of all thin film samples with t≥15nm. The lower limit is set by the resolution of x-ray reflectometry.
The experimental results revealed a short deviation of the copper concentration from its nominal value (2 percent), which confirmed an accurate stochiometric transfer during the PLD-process in this set of samples. Unfortunately, this relation could not be investigated for the thinner films presented in Tab 3.2, whose characterization is the main issue in the present work.

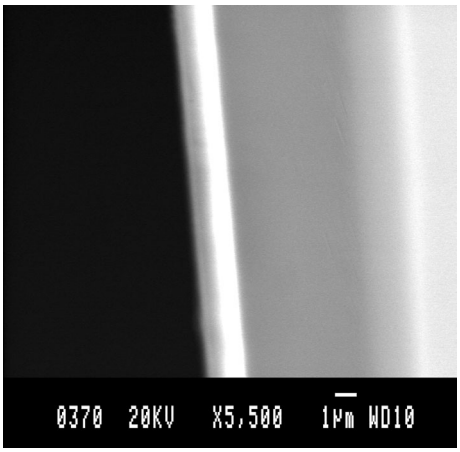

Figure 4.17: Cross-sectional SEM image of sample WMI 05. The white stripe at the edge corresponds to the conducting thin film, while the darker part to the right represents the insulating substrate.

4.2.4 SQUID-Magnetometry

As stated in the introduction, the magnetic characterization of DMS, aiming the identification of room-temperature ferromagnetism, is of great importance. In the present work, thin films of Cu-doped ZnO have been charatcterized by means of SQUID-magnetometry. The role of the growth parameters on the magnetic properties of the samples was particularly investigated. For each set of samples deposited in Ar and O_2 atmosphere, two substrate temperatures were chosen (300°C, 450°C) at a constant pressure of 1 x 10^{-2}mbar. The samples were submitted to a standard measurement procedure: the field dependence of the magnetization was measured in the range -7T$\leq \mu_0 H \leq$+7T with the MPMS-XL and in the range -1T$\leq \mu_0 H \leq$+1T with the MPMS-2 SQUID- magnetometers. It is worth to mention that the magnetic moment detection resolution of the MPMS-XL device is one order of magnitude better than the MPMS-2 (10^{-7} vs 10^{-6} emu). The field dependence was measured in both cases at a constant temperature of 5K and 300K. In addition, the temperature dependence of the magnetization M(T) was measured from 5 to 350K. In all the field dependence measurements, a diamagnetic contribution of the form

$$M_{dia}(H) = -c \cdot H \tag{4.5}$$

was substracted. In squid magnetometry, the magnetic moment coming both from substrate and film are detected, as well as from other materials which are under the detection range of the pick-up coils (see Fig (2.7)), such as the glue used to mount the samples in the straw.

Both substrate (Al_2O_3) and glue are expected to be diamagnetic, so that they will

not interfere with the ferromagnetic signal expected from the film at first stage. Nevertheless, substrates even prepared under high-purity conditions will have an small amount of impurities, which could be para-or ferromagnetic. Since the volume ratio from substrate to film is about 10000:1 for a 50nm thin film, and further considering that the ferromagnetism on the films arises from diluted (2%) magnetic ions, the contribution of possible impurities build into the sapphire structure is not negligible. After characterizing the plane Al_2O_3-substrate, it has been found out that they do show a weak ferromagnetic signal, after substracting its diamagnetic contribution. The saturation magnetization has been estimated to be of the order $M_s = 8\times10^{-6}$emu at room temperature. Remanence and coercivity could not be detected, since the values lie in the detection limit of the MPMS-2 squid magnetometer. This result was not encouraging at all, but it suggested that measuring very thin films with SQUID magnetometry will lead to an interpretation problem: if the total moment of substrate and film lies in the range of the ferromagnetic background, the uncertainty to know whether the magnetization is coming from the substrate alone or from the film, or to which extent contribute one or the other to the total ferromagnetic signal, will disqualify the measurement. The ferromagnetic background was assumed to be of the same order in all the cases, since the samples were grown on substrates coming from the same charge.

Sample	**Thickness** [nm]	T_{sub} [°C]
AR 1	18,2	450
AR 4	37,4	300
AR 1R	103	450
AR 4R	180	300
OX 1	32,4	450
OX 3	34,1	300
OX 1R	58	450
OX 3R	90	300

Table 4.4: Set of samples characterized by SQUID-Magnetometry. Samples with equal name have been deposited under the same conditions. The name extension „R“(repeat) just denotes that the samples have been grown with more laser pulses to gain thickness.

In order to find out the critical film thickness, where the ferromagnetic signal coming from the films lies well above the substrate background, the samples ranging from t=18,2nm (AR 1) and t=180nm (AR 4R) have been investigated. An overview

is shown in Table 4.4. On the one hand, thicker films will increase the signal-to-background (film to substrate) ratio in SQUID-magnetometry, but on the other hand, it would be disadvantageous for its preparation for magnetotransport measurements (recommended thickness for sample preparation with optical litography and ion-beam-etching: t≈ 100nm), so that samples between 20 and 200nm have been investigated.
Starting with the field dependence of the magnetization at room-temperature (300K), as observed in Fig (4.19), films with thicknesses typically under ≈ 60nm fall in the range of the substrate background. No quantitative conclusion of the magnetic nature of these samples can be drawn from this point of view. Therefore, the magnetic characterization of the films will concentrate on the samples with t≥90nm (Tab 4.4). Comparing AR 1R with AR 4R, the influence of substrate temperature can be studied, while comparing AR 4R with OX 3R will give information about the role of growth atmosphere.

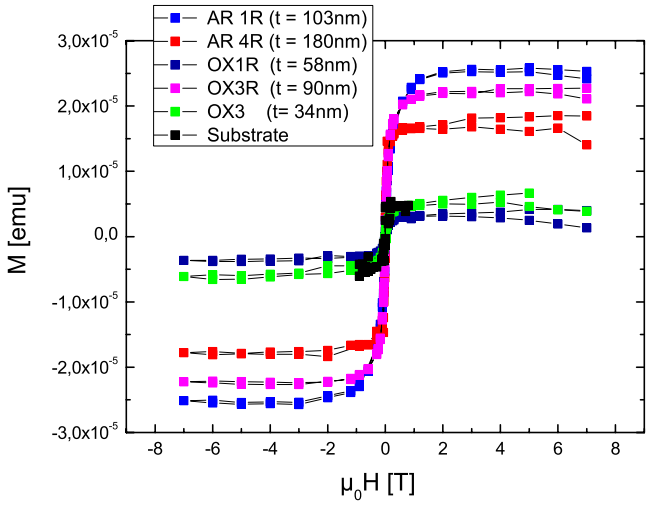

Figure 4.18: M(H) behaviour of ZnO:Cu samples, at 300 K. The substrate data is highlighted in black. Note that the thinner films fall under the substrate background.

However, some qualtitative information can be extrapolated from the plots which merge with the substrate background. Looking at the magnetization curves of OX 1R and OX 3, very qualitative comparisons can still be made. If we assume that both samples have the same magnetic moment per dopant atom, and that the substrate contribution is equal for both, we will expect a higher magnetization for sample OX 1R, as the thickness is almost two times greater. The experimental results show even a lower M_s value for the sample OX 1R, which implies that films deposited under

OX 1R conditions may have a very weak ferromagnetism at room-temperature, if any. Regarding the M(H) behaviour at 5K, a similar picture could be observed. The signal of samples OX 1R and OX 3 is comparable with the one of the substrate. At 5K, the difference between both samples (OX 1R/OX3) is not noticeable, in contrast the room-temperature hysteresis loop. Still, the ferromagnetic nature of the films cannot be proved, since the signals merge with the substrate background.

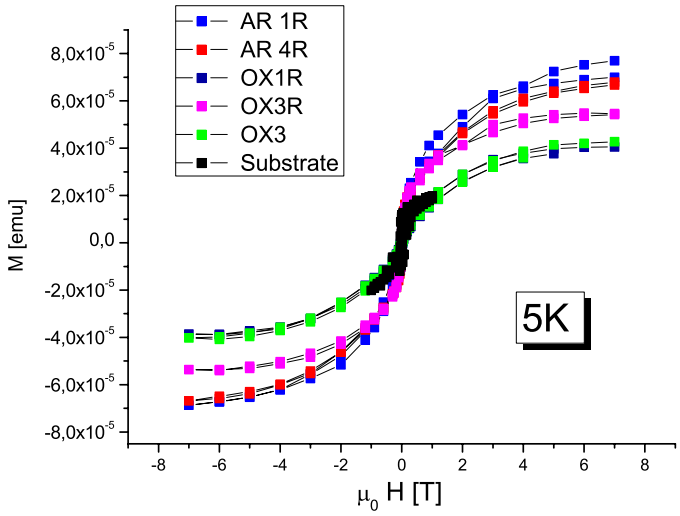

Figure 4.19: M(H) behaviour of ZnO:Cu samples, at 5K. The substrate data is highlighted in black.

The role of substrate temperature, as well as background gas on the magnetic properties of ZnO:Cu thin films, will be described next. For this purpose, field and temperature dependence of the samples with signal well above the ferromagnetic substrate contribution, will be analized and interpreted, and values for coercivity, remanence and saturation magnetization will be calculated in order to quantify the ferromagnetism in the samples.

- To find out the influence of T_{sub} on the magnetic properties of the studied system, we will concentrate on samples AR 1R and AR 4R, grown at 300°C and 450°C, respectively, and otherwise under identical process conditions:

  Neglecting the substrate background contribution, and assuming that the ferromagnetic signal is only due to the incorporation of the dopants, the saturation magnetization of the sample AR 1R would be greater than $1\mu_B/Cu^{2+}$,at 300K. The hysteresis loops are plotted in Fig (4.20).

  Since copper in its Cu^{2+} state has one unpaired spin in its electronic configuration ([Ar]$3d^9$), the maximum expected moment per atom is $1\mu_B$. That means,

Sample	**Thickness** [nm]	**T_{sub}** [°C]	**Pressure** [mbar]	**Background gas**
AR 1R	103	**450**	1 x 10^{-2}	Ar
AR 4R	180	**300**	1 x 10^{-2}	Ar

Table 4.5: Process parameters of AR 1R / AR 4R. They just differ by the substrate temperature.

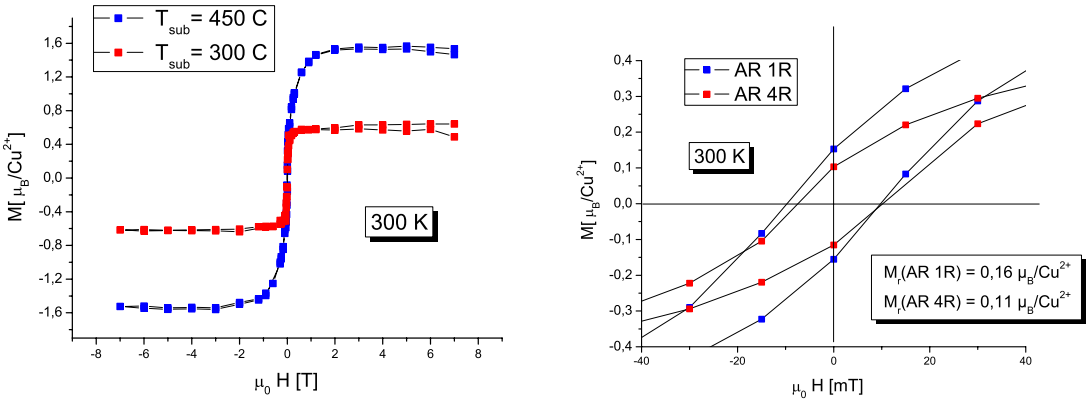

Figure 4.20: M(H) loops at 300K, without considering the ferromagnetic contribution of the substrate.

the ferromagnetic substrate contribution has to be corrected, in order to get reasonable results. Table 4.6 shows the corrected values for saturation magnetization, remanence and coercivity at 5 and 300K. The corresponding M(H) and M(T) curves after the substrate correction are presented as well. For the calculation of the magnetic moment per dopant atom, the thickness of the samples and the dopant concentration is needed. The thickness was determined with good precision by means of X-ray reflectometry, while for the dopant concentration, it was assumed that all the doped ZnO films contain 2 atomic percent of Cu, since the EDX technique could not be performed for samples in this thickness range.

Sample	$\mathbf{T}_{sub}$ [°C]	$\mathbf{M}_s$ [μ_B/Cu^{2+}]	$\mathbf{M}_r$ [μ_B/Cu^{2+}]	$\mathbf{B}_c$ [mT]
AR 1R at 5K	**450**	2,5	0,18	20
AR 4R at 5K	**300**	0,95	0,07	13,5
AR 1R at 300K	**450**	0,65	0,06	10
AR 4R at 300K	**300**	0,25	0,04	8,5

Table 4.6: Magnetic parameters of ZnO:Cu thin films, grown in Ar-atmosphere. Note that the saturation moments for AR 1R at 5K are not realistic.

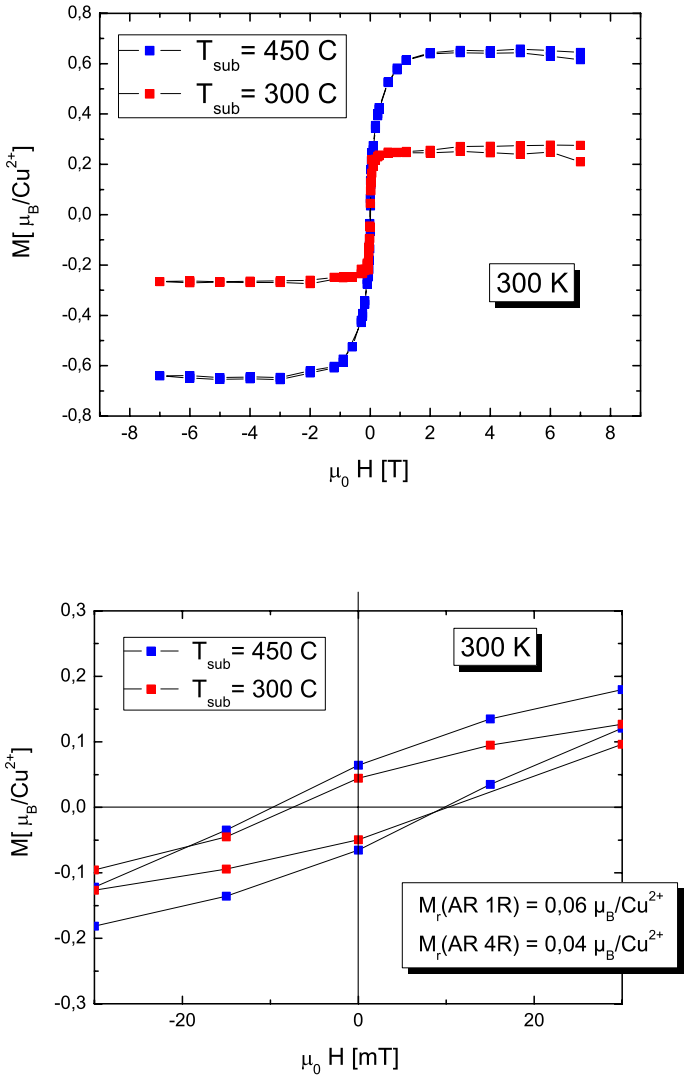

Figure 4.21: M(H) loops at 300K, background-corrected and normalized in units of μ_B per dopant atom.

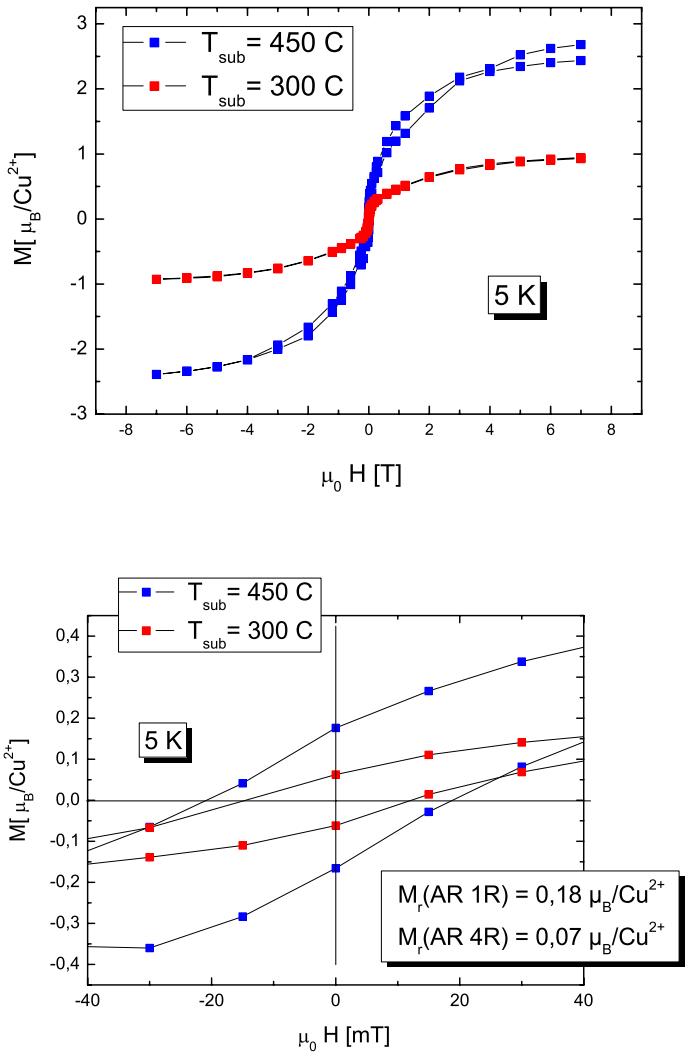

Figure 4.22: M(H) loops at 5K, normalized in units of μ_B per dopant atom.

Regarding the field dependence at 300K, the sample grown at T_{sub}= 450°C shows by far the largest saturation magnetization. Nevertheless, remanence and coercive field have very similar values. In the 5K loop, on the contrary, the remanence of the samples diverge almost by factor three. This behaviour is confirmed by comparing the temperature dependence of the magnetization (4.23). Since the field is quenched down to 0 Tesla for a typical M(T) measurement, the signal describes how the *remanent* magnetization changes with temperature. It is clearly observed that the temperature has a higher impact on the remanence for the sample grown at T_{sub}= 450°C. This M(T) behaviour

agrees with the remanence values obtained from the hysteresis loops.

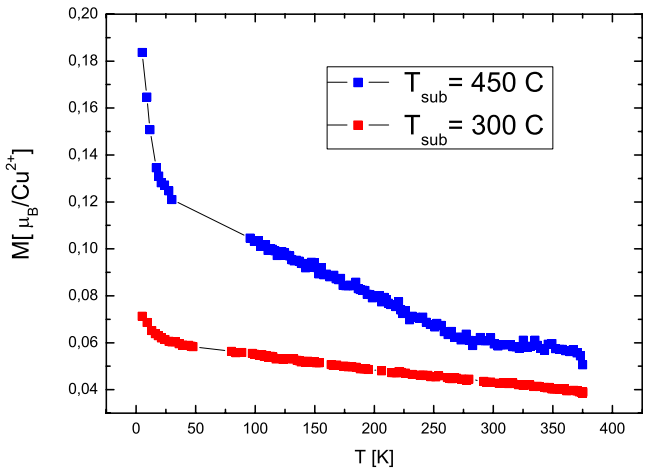

Figure 4.23: M(T) behaviour of samples grown in Ar-atmosphere, after correcting the ferromagnetic background coming from the substrate.

Another interesting observation is that the saturation moment, at 5K, exceeds the theoretical value of $1\mu_B/\mathrm{Cu}^{2+}$, and that the magnetization saturates with a much slower rate than in the 300K loop. Both facts lead to the suspicion, that an additional contribution might be involved in the process. In fact, following the bound magnetic polaron model (Section 1.2) as the collective state of long-ranged ferromagnetism in DMS, it is also possible that magnetic dopants which are not under the range of the magnetic polarons, couple either paramagnetic (isolated) or antiferromagnetic (forming pairs). The probability, that two Cu-atoms lie next to each other in the host structure (that they replace two Zn atoms which are adjacent), is much lower than 0,1 %, considering that there are only 2 Cu- for every 100 Zn-atoms. As a consequence of this statistical estimation, an antiferromagnetic coupling of dilute magnetic atoms can be neglected. The atoms which are not under the range of magnetic polarons will therefore produce a paramagnetic contribution, given by the relation

$$M_{para} = M_s \cdot B_J(y) \tag{4.6}$$

where M_s is the paramagnetic saturation magnetization of the Cu-atoms and $B_J(y)$ is the Brillouin-function defined as

$$B_J(y) = \frac{2J+1}{2J} coth(\frac{2J+1}{2J} \cdot y) - \frac{1}{2J} coth \frac{y}{2J} \tag{4.7}$$

with the argument $y = \frac{g_J \mu_B B}{kT} \cdot J$. The quantity J is the quantum number which considers both spin (S) and orbit (L) momentum for a determined electronic configuration. Following Hunds rule, the electronic configuration of Cu^{2+} ($[Ar]3d^9$), having the orbital (d) more than half filled, implies a positive coupling between spin and orbit momentum, as

$$J = L + S \tag{4.8}$$

Since the Cu-atoms are supposed to be embedded in the host structure, they are regarded as quasi-bound and hence the orbit interaction can be neglected. Then J will be equal to S=(1/2) for the Cu^{2+} electronic structure. With the determination of J, the calculation of the paramagnetic contribution to the magnetization can be performed, since all the other quantities present in the Brillouin-function and its argument are well-defined. The Lande-factor will be g_J=2 for J=S.

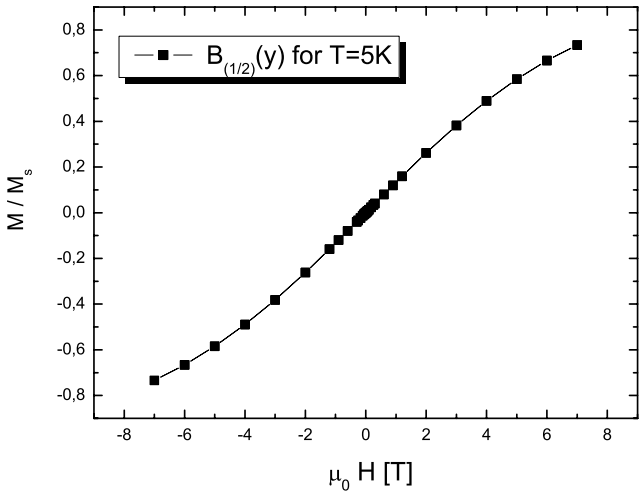

Figure 4.24: Brillouin-function at 5K, for S=(1/2) Cu-atoms. The maximum value is reached at 7 Tesla and is around 0,75.

Taking into account eq.(4.6), the maximum value of the Brillouin function is 1, when M reaches saturation ($M_{para} = M_s$). For the used parameters of

T and B (5K, 7T), the Brillouin function does not reach the value of 1 at maximum field. Either a higher field or a lower temperature is needed, so that the contribution of the paramagnetic Cu-atoms reaches saturation. At 300K, however, the paramagnetic contribution is negligible, since the argument y in the Brillouin-function will have 50 times a lower value. That means, what has been measured in the M(H) dependence at 300K is only due to the ferromagnetic contribution of the sample.

However, the contribution of the Cu-atoms, which do not couple ferromagnetically, is not sufficient to explain the large moments observed at 5K. Assuming that there is indeed 2% Cu-concentration in the samples, the sum of para- and ferromagnetic moments caused by the dopant Cu should not exceed the value of $1\mu_B$ per Cu^{2+}, after normalizing the absolute values. Therefore, either the Cu-concentration was underestimated or there is another effect which is taking part. In fact, the form of the Brillouin-function describing the paramagnetic contribution of spin-(1/2) Cu-atoms which do not contribute to ferromagnetic ordering, does not match with the measured 5K-loop. This behaviour suggests that there is another source of paramagnetism which contribute to the SQUID-signal, and the most reasonable explanation is that there might be not only ferromagnetic, but also paramagnetic impurities diffused in the substrate in the preparation stage, which may have a higher spin quantum number. As a result, the M(H) signal at 5K is product of following contributions (after substraction of $M_{ferro}^{substrate}$):

$$M_{total} = M_{para}^{Cu(2+)} + M_{ferro}^{Cu(2+)} + M_{para}^{substrate} \tag{4.9}$$

The situation at 5K turns complicated due to the paramagnetic contributions of Cu-atoms and substrate impurities. The former could be estimated, but the latter is very difficult to quantify. Nevertheless, the large moments observed at 5K, exceeding the theoretical expected values could be explained in terms of paramagnetic substrate impurities. It should be mentioned, that an underestimation of the Cu-concentration may also be involved, but the magnitude and form of the M(H) signals at 5K suggest that the substrate impurities are the dominant factor. At 300K, the calculation of the net magnetic moment of the sample is more accurate, since there is only the one contribution ($M_{ferro}^{substrate}$) which has to be substracted.

Concerning the influence of T_{sub} in samples deposited under O_2-atmosphere, quantitative conclusions could not be drawn, since the sample with T_{sub}=450°C showed a very weak signal, falling in the range of the ferromagnetic background

of the Al_2O_3-substrate. It is true that the sample had half of the thickness, but assuming that it has the same moment as the sample with T_{sub}=300°C, a higher value would be still expected, lying well above the substrate background. As a qualitative observation, a lower process temperature might favour ferromagnetism in samples grown in oxygen environment.

- Role of background gas: Interestingly, the samples grown in oxygen follow a different trend than the ones in grown in Ar, since the optimal substrate temperature which favour ferromagnetism is T_{sub}=300°C and not T_{sub}=450°C. Due to this fact, it is more convenient to compare the samples which show optimal ferromagnetic ordering in each background atmosphere, since the aim is to find the most suitable process parameters which favour a ferromagnetic ordering.

Sample	**Thickness** [nm]	**T_{sub}** [°C]	**Pressure** [mbar]	**Background gas**
AR 1R	103	450	1 x 10^{-2}	Ar
OX 3R	90	300	1 x 10^{-2}	O_2

Table 4.7: Process parameters of AR 1R/OX 3R, samples which show the best ferromagnetic properties.

Starting with the field dependence of the magnetization at 5K, the sample grown in Ar-atmosphere show a clearly higher remanence and coercivity. Again, a qualitative comparison of the saturation moments cannot be made due to the paramagnetic contribution of substrate impurities. However, taking into account the form of the M(H) loops, it is evident that there are less paramagnetic substrate impurities in the sample grown in oxygen.

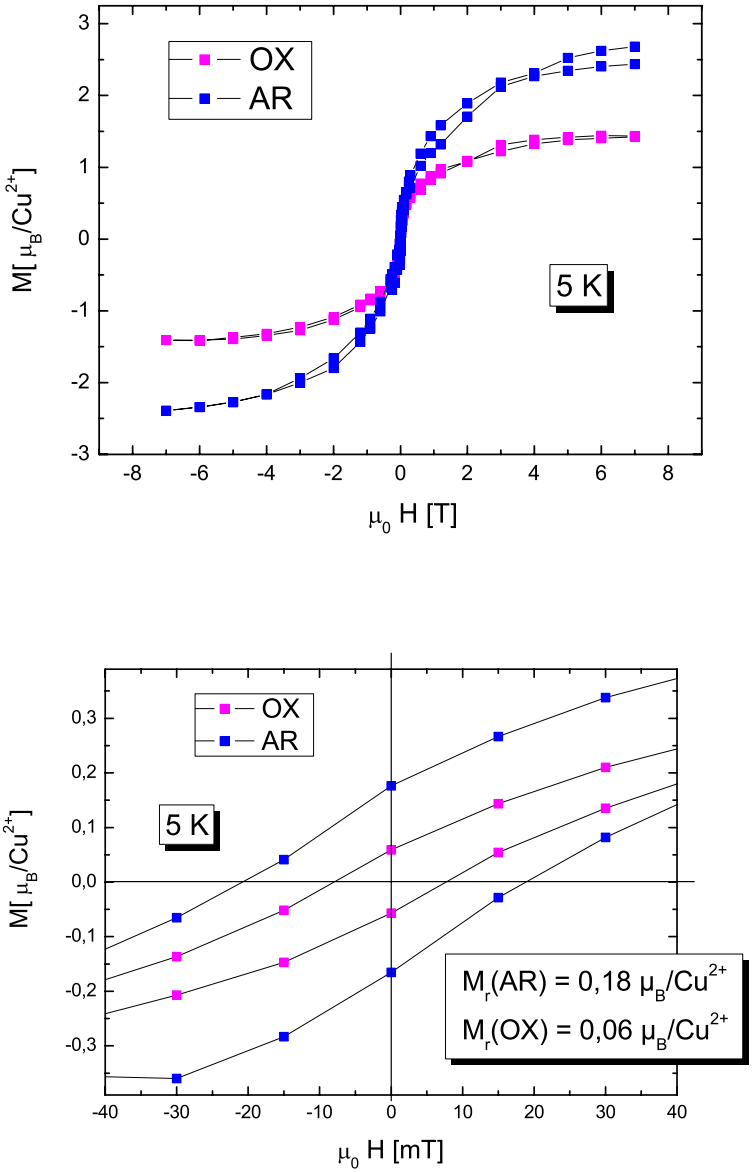

Figure 4.25: Hysteresis loops at 5K, after substracting the ferromagnetic substrate background. Paramagnetic substrate impurities give rise to large saturation moments. Remanence and coercivity can be observed in the inset at low fields.

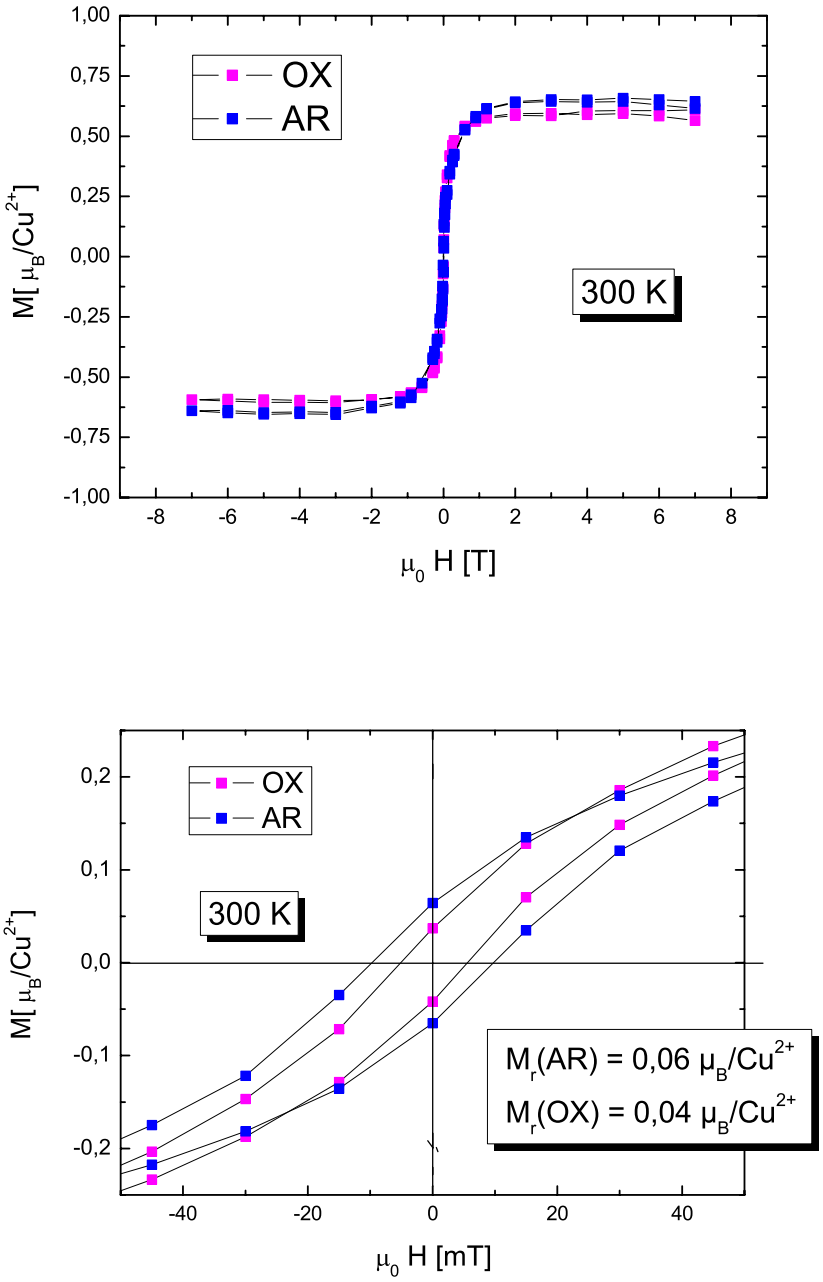

Figure 4.26: Hysteresis loops at 300K, after substracting the ferromagnetic substrate background. Remanence and coercivity can be observed in the inset at low fields.

The remanence at 5K is three times greater for the sample grown in Ar-atmosphere, while at 300K, both remanence values lie very close (Fig 4.26). This could be confirmed by measuring the temperature dependence of the remanence M(T). Once again, it could be observed that the sample AR 1R has a very strong temperature dependence of the remanence in comparison to the rest of the samples (AR 4R,OX 3R). This behaviour will be pointed out again when discussing the anomalous Hall-Effect measurements (Section 4.2.5). The saturation moments of both samples are, in contrast to 5K, nearly equal at room-temperature, but remanence and coercivity show still greater values for the sample grown in Ar.

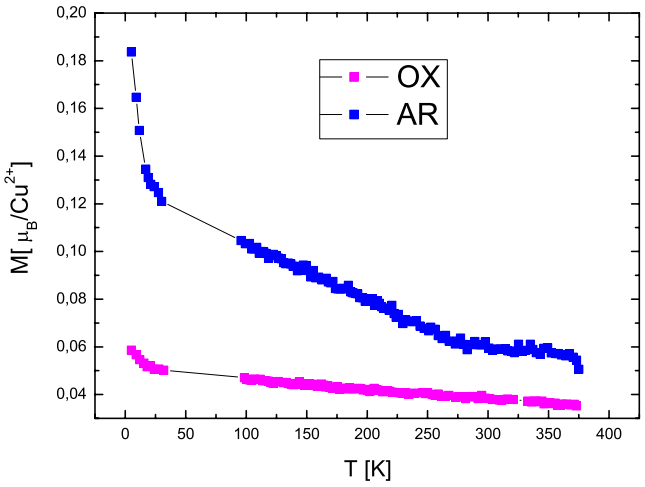

Figure 4.27: M(T) behaviour of samples grown in different background atmospheres.

Sample	$\mathbf{M}_s$ $[\mu_B/\mathrm{Cu}^{2+}]$	$\mathbf{M}_r$ $[\mu_B/\mathrm{Cu}^{2+}]$	$\mathbf{B}_c$ [mT]
AR 1R at 5K		0,18	**20**
OX 3R at 5K		0,06	**9**
AR 1R at 300K	0,65	0,06	**10**
OX 3R at 300K	0,6	0,04	**5,5**

Table 4.8: Influence of the background gas on the magnetic parameters of ZnO:Cu thin films. Note the particular difference in the coercivity. The saturation moment at 5K could not be obtained in terms of μ_B/Cu^{2+} due to the paramagnetic substrate contribution.

The background gas has a clear influence in the coercivity of the samples, since the one grown under oxygen has by far the lowest coercive field. As discussed

in the theory chapter (Section 1.2), the coercivity depends strongly on the structural defects of crystalline materials. Samples grown in oxygen atmosphere will have a better stochiometry and therefore less defects and vacancies in the crystal structure. The best crystalline quality was found at the sample grown in oxygen, at the highest pressure. Resuming, the fact that the structural defects and vacancies indeed influence the coercivity of Cu-doped ZnO films, could be confirmed by using different background gases in the film preparation.

In the work of Diaconu *et al.*[26], a clear correlation between mosaicity and coercivity could be found in Mn-doped ZnO films grown on sapphire, where the coercivity passes through a maximum at a critical column diameter, as a result of anisotropy and exchange energy balance with increasing grain size. This model is thus only applicable for systems which show uniaxial anisotropy, as is the case of the columnar growth of ZnO on sapphire. Taking into consideration the relation between surface morphology and column diameter pointed out in [28], it can be concluded that the films grown in Ar, which show by far the largest RMS-roughness values, tend to grow in columns with bigger diameter. The surface roughness is proportional, in a columnar growth mechanism, to the column diameter [26, 28].

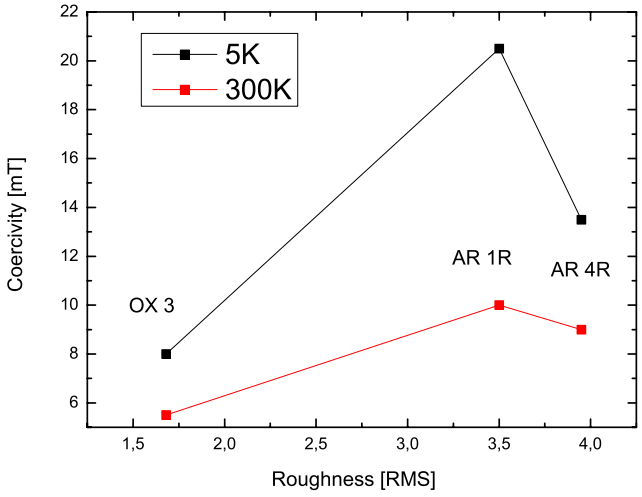

Figure 4.28: Relation between coercivity and surface roughness, proportional to the column diameter, at three different samples. Note that the coercivity passes through a maximum, in agreement with [26].

Fig 4.28 shows the relation between coercivity and surface roughness of the investigated samples. As a result, the fact that the coercivity passes through a

maximum by increasing the column diameter in Cu-doped ZnO films, suggests that the coercivity can be controlled, indeed, by the film preparation conditions, in agreement with [26]. In addition, this result confirms the columnar growth of Cu-doped ZnO on sapphire, property which could not be visualized due to the lack of Transmission Electron Microscopy (TEM) facilities.

Summarizing, ferromagnetic ordering at room-temperature could be observed by proper choice of process parameters. In Ar-atmosphere, ferromagnetism appears both at T_{sub}=(300,450°C), while in oxygen environment, a ferromagnetic signal which lies well above the substrate background was found only at T_{sub}= 300° C. The most robust ferromagnetism was clearly observed at the sample with T_{sub}= 450°C grown in Ar-atmosphere (AR 1R), reaching room-temperature values of 0,65 and 0,07 μ_B/Cu^{2+} for M_s and M_r, respectively, and a coercivity of 10mT. In general, the coercivity has a particular low value (≈ 5-20mT), classifying the ZnO:Cu system as a very soft magnetic material. The coercivity is clearly linked to the structure of the thin film samples, and can be tuned by choosing the proper growth conditions. At low temperatures (5K), paramagnetic substrate impurities have been found to be the main reason for the observation of saturation moments which lie over the theoretical expected value of $1\mu_B/Cu^{2+}$. The presence of ferromagnetic impurities in the films can be ruled out, since the magnetization is correlated with the film thickness and hence with the total amount of Cu-dopants which are supposed to be the responsibles for ferromagnetic ordering. Only films with a thickness t≥ 60nm show a total magnetization which could be distinguished from the ferromagnetic substrate background. The presence of external ferromagnetic impurities like Fe or Co particles would lead to a strong ferromagnetic signal in the samples, taking over the intrinsic contribution from the Cu-doping, regardless of the film thickness. This experimental observations point towards a intrinsic nature of ferromagnetism in the Cu-doped samples characterized by SQUID-magnetometry, supported by the fact, that a potential formation of Cu-clusters will not contribute to the ferromagnetic signal.

4.2.5 Magnetotransport

Regarding magnetotransport measurements, only samples prepared under the lowest background gas pressure could be characterized both at high (room-temperature) and low (5K) temperatures. Since the resistivity of semiconductors generally increases exponentially with decreasing temperature, samples which show high insulating behaviour at room-temperature will increase their resistivity by decreasing temperature to such point, that the values will escape to the measurement detection capability (≈GΩ), especially if the dimensions of the sample are small. In this case, neither

magnetotransport nor Hall-effect measurements could be performed. The role of Cu-doping, as well as the process pressure used to grow the thin films will have an interplay on the conductivity. It is well known that Cu-doping in ZnO was performed in order to increase the resistivity of unintentionally doped n-type ZnO [29, 30], which suggested that Cu-doping will introduce deep levels in the bandgap of ZnO. On the other hand, the n-type character of ZnO can be intensified by the formation of donor levels, originated by intentionally introduced defects, such as Zn-interstitials (shallow donors) [31] or oxygen vacancies (deep donors)[16]. Regarding the material preparation, the donor defects will be created at oxygen-poor conditions. Therefore, Cu-doped ZnO with both unintentionally and intentionally introduced donor defects, will be a compensated semiconductor. The challenge is to identify the transport mechanism in the system and to find out the role of parameters like background gas type, pressure and substrate temperature. In presence of an external magnetic field, the field dependence of the resistivity in both longitudinal and hall configuration will be discussed, in order to find possible relations between magnetic and transport properties, fact which would help to go one step closer to understand the question of the origin of ferromagnetism in TM-doped ZnO.

Sample	$\mathbf{T}_{sub}$ [°C]	**Pressure** [mbar]	**Background gas**
AR 1	450	1 x 10^{-2}	Ar
AR 4	300	1 x 10^{-2}	Ar
AR 1R	450	1 x 10^{-2}	Ar
OX 1	450	1 x 10^{-2}	O_2
OX 3	300	1 x 10^{-2}	O_2
OX 5	500	5 x 10^{-2}	O_2
OX 7	650	5 x 10^{-2}	O_2

Table 4.9: Samples which could be investigated regarding transport properties. Only the samples prepared at p= 1 x 10^{-2}mbar could be characterized in terms of magnetoresistance and hall-effect.

Temperature dependence of the resistivity

As stated above, the background gas pressure will have a crucial influence on the resistivity of Cu-doped ZnO films. For the present study, only films grown at p$\leq$0.05mbar could be characterized down to low temperatures. The effect of high oxygen pressure in pure [24, 32] as well as in doped [33] ZnO, which is supposed to increase the resistivity and decrease the number of free carriers, could be verified in Cu-doped ZnO

films, as observed in Fig 4.29.

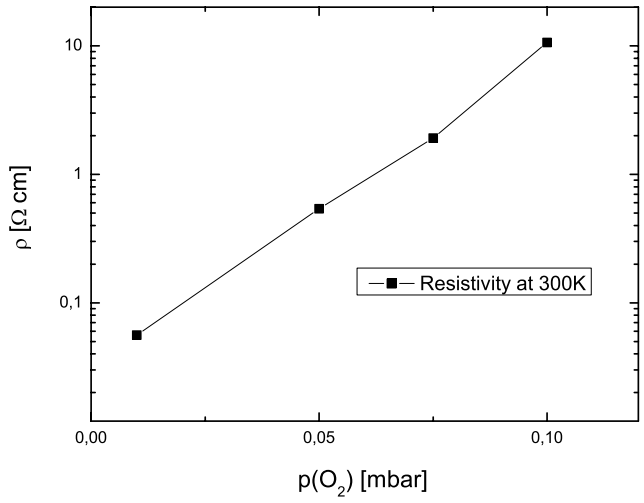

Figure 4.29: Change in the room-temperature resistivity of Cu-doped ZnO films at different oxygen pressures.

A huge disadvantage, however, arises for Cu-doped ZnO in terms of transport measurements, since the Cu-dopants will act as compensating centers, which are supposed to reduce the carrier density and thus increase the resistivity up to values which escape from the measurement capability. Tab 4.10 compares room-temperature values of undoped n-type ZnO measured by Tiwari *et al.*[32] and Cu-doped ZnO prepared in the present work, at high oxygen pressures, elucidating the role of the Cu-dopants on the resistivity.

Pressure (mbar)	**Resistivity at 300K** [Ωcm] (ZnO)[32]	**Resistivity at 300K** [Ωcm] (Cu-doped ZnO)
100	0,243	≥15
0.1	0,167	10,6

Table 4.10: Role of Cu-doping in the resistivity of ZnO thin films.

The study of the temperature dependence of the resistivity will therefore concentrate mainly on samples grown under 0.05 and 0.01 mbar pressure, which in the most cases show measurable resistance down to 5K. The measurement range was typically from 5 to 300K. The substrate temperature will also have an important influence on the conductivity and in the transport mechanism.

Starting with the samples prepared at higher oxygen pressure (0.05mbar), the substrate temperature plays a crucial role not only for the resistivity values, but also for the transport behaviour. As pointed out in the theory chapter, the energy gap can be estimated plotting the ρ(T) measurement as ln ρ(1/T) and using the Boltzmann equation

$$ln\rho(T) = ln\rho_0 + \frac{\Delta E}{2k_B T} \tag{4.10}$$

where the energy gap ΔE is obtained from the slope of the curve. The sample grown at higher substrate temperature (650°C) shows two linear ranges where an energy gap could be calculated, namely from 100 to 300K and from 5 to 20K. The latter is still a fit with quite high error margin, since the curve does not follow a strictly linear relation, but it is useful to provide a rough idea of the activation energy at low temperatures.

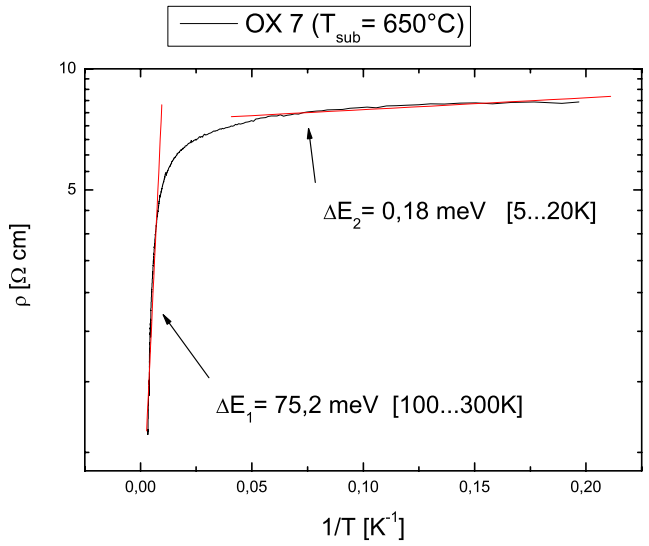

Figure 4.30: Energy gap calculation of the sample grown at high temperature (650°C). Two activation ranges could be clearly observed.

The energy gap value at high temperatures ($T \geq$100K) of OX 7 is 75.2 meV, energy which could be explained in terms of activation of a shallow level. The native shallow donors, Zn-interstitials, have an energy around 30meV below the conduction band [31], so that the observed activation, which starts around 100K, is a little bit too high to be adressed to native shallow donors in the sample grown at T_{sub}=650°C. However, it is worth to point out that this activation calculations have an error margin, since

there is a big transition range between 20 and 100K, where the bandgap activated transport changes drastically.
Regarding the sample grown at 500°C, the transport behaviour was completely different, and a energy gap calculation could not be performed because the Arrhenius plot (lnρ vs 1/T) did not show a linear behaviour in the whole temperature range, as seen in Fig 4.31.

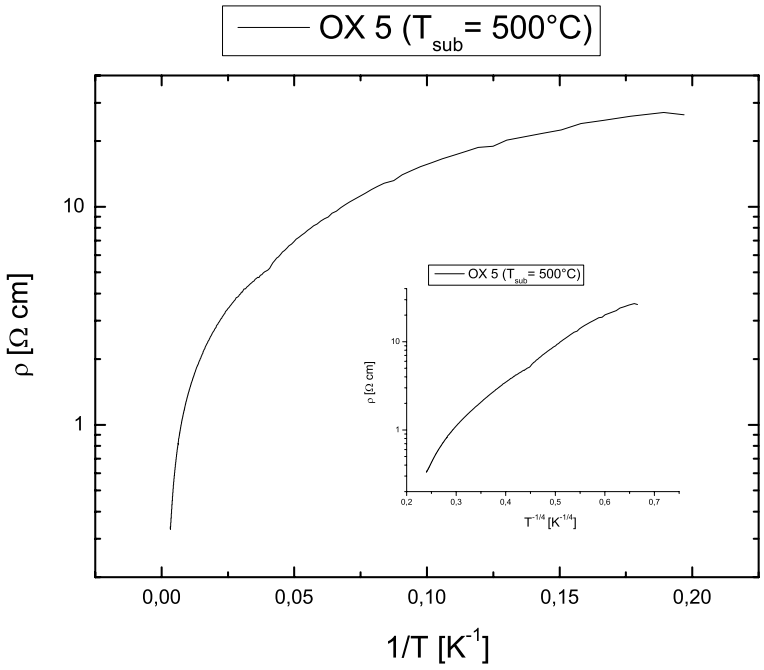

Figure 4.31: At T_{sub}=500°C, no linear relation could be found in the standard plot for energy gap estimation. Inset shows the relation to $T^{-1/4}$, which is closer to linear.

Since a band-gap transition could not be observed, it remains the possibility of other transport mechanisms. The insulating (semiconducting) behaviour could be influenced by lattice disorder (Anderson-localized insulators) or by electron correlation (Mott-insulators)[34, 35, 36]. For Mott-insulators, however, a large donor electron concentration is needed, so that electron-electron phenomena become dominant.
Mott-insulators [37] and Anderson localized insulators [32, 36, 38] follow the relation ln $\propto T^{(-1/3)}$ and ln$\rho \propto T^{(-1/4)}$, respectively. In the case of the sample grown at 500°C, the best fit could be achieved in the case lnR $\propto T^{(-1/4)}$ (inset in Fig 4.31), so that the sample is „closer“ to the Anderson-localized state, however, a clear linear relation could be neither observed, so that the transport mechanism of the sample grown at 500°C (OX 5) could not be determined with certainty. It is worth to underline that

the substrate temperature is the only parameter which differences both samples, fact which suggests that the reason of this different behaviour is one of the consequences produced by T_{sub} on the films. As discussed in the structural characterization (Section 4.1), the substrate temperature has an influence on the crystalline properties of the films: the FWHM of the rocking curve from the sample at T_{sub}=650 C showed the lowest value (Fig.4.12), suggesting a better crystallinity and less lattice disorder in the structure. Since the lattice disorder, caused by the mosaicity (columnar structure, grain boundaries) as well as by vacancies and native crystal defects, will favour the localization of electronic states, a transition might be observed between a band-gap insulator and an Anderson-localized insulator. Such transition was observed by Tiwari *et al.*[32] by just changing the oxygen stochiometry in undoped $ZnO_{[1-\delta]}$ thin films. In the present work, samples grown under lower pressure will be also analized in terms of identifying the dominant transport mechanism. From our observations, it can be stated as an early qualitative result, that not only oxygen nonstochiometry, but also the crystalline quality and grade of structural disorder of the films will have a strong impact on the transport properties of doped and undoped ZnO thin films. It should be pointed out that the localization of the electronic states in an Anderson-localized insulator may occur independently of the impurity levels induced by the 3d-TM dopants, which means that is not a characteristical feature of dilute magnetic semiconductors.

Continuing with the sample characterization, the temperature dependence of the resistivity was measured for the remaining five samples, grown at moderate substrate temperatures and lower background gas pressures. In fact, the samples prepared under this conditions (with one exception: OX 1/OX 1R) could be successfully characterized by SQUID-magnetometry. Tab 4.11 shows an overview of the deposition conditions.

Sample	**T_{sub}** [°C]	**Pressure** [mbar]	**Background gas**
AR 1	450	1 x 10^{-2}	Ar
AR 4	300	1 x 10^{-2}	Ar
AR 1R	450	1 x 10^{-2}	Ar
OX 1	450	1 x 10^{-2}	O_2
OX 3	300	1 x 10^{-2}	O_2

Table 4.11: Overview of the process parameters of the samples from the last series.

All the samples have a thickness around 30nm (see Section 4.2), excepting sample AR 1R which is the replique of AR 1, but 103nm thick. Since the lattice defects have

a strong influence on the conductivity, as seen at the samples from the first series, it would be also interesting to see how the transport properties behave by increasing the film thickness. It is well known that a finite amount of structural defects will be induced at the substrate-film interface, especially if there is a mismatch between substrate and film, which is our case, so that the thickness might also play a role in this game. Thus, the characterization of AR 1R should be taken into special consideration.

Continuing with the characterization of the samples grown under oxygen atmosphere, the ρ(T) curves of the last two samples (OX 1/OX 3) are presented in Fig 4.32 showing values for room-temperature resistivity.

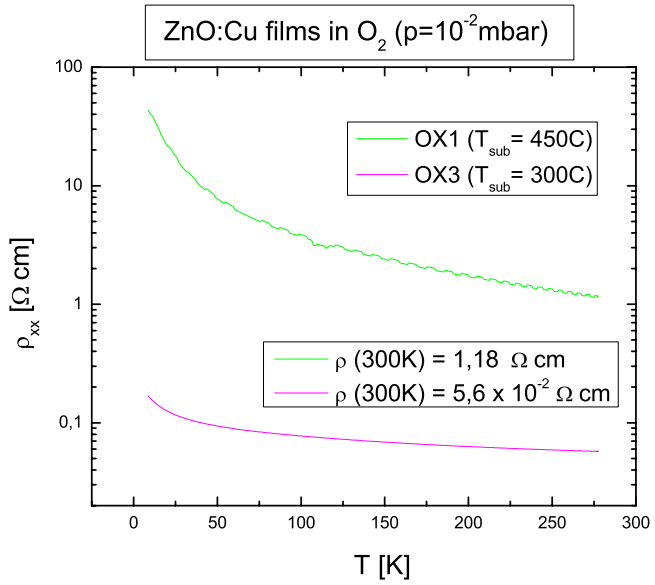

Figure 4.32: R(T) behaviour of samples grown in oxygen atmosphere. Note that the only difference between both samples is T_{sub}.

Once again, the substrate temperature has a strong influence on the conductivity. But in this case, since both samples have the same oxygen stochiometry, similar thickness, and the substrate temperature has not much influence on the crystalline properties by changing from 300° to 450°C, the reason for such different behaviour could not be clarified. It is worth to mention, however, that there is a correlation between magnetic and transport properties, since the film with higher conductivity (OX 3) exhibits the strongest magnetic properties. In fact, the ferromagnetic ordering in the high resistive sample grown under OX 1 conditions was so weak, that it could not be distinguished from the ferromagnetic background coming from the substrate

(Section 4.4). The same correlation could be observed at the samples prepared in Ar-atmosphere, as observed in Fig 4.33. Interestingly, the substrate temperature which favours ferromagnetic ordering in Ar-atmosphere is 450°C and not 300°C like in oxygen, and again, the better conducting properties were found at the sample which exhibits a higher magnetic moment.

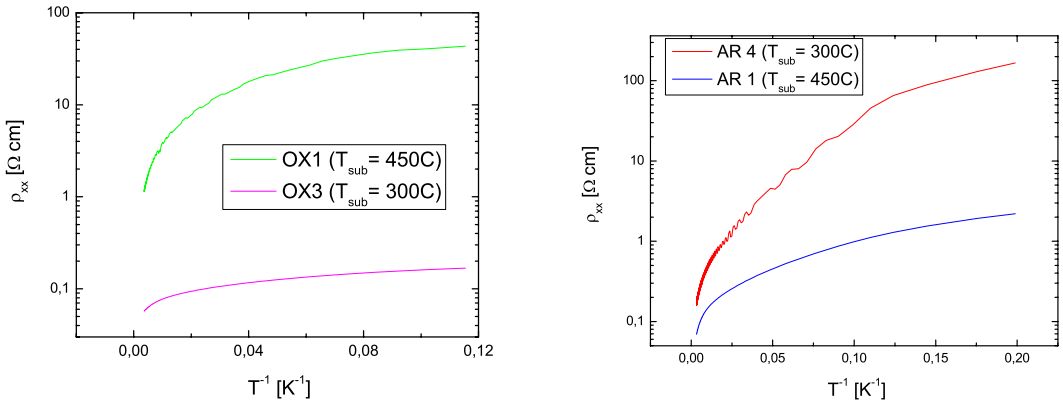

Figure 4.33: Arrhenius plots for the energy gap calculations. Neither in Ar nor in O_2 atmosphere, a linear relation could be identified in the whole temperature range.

According to Fig.4.33, none of the samples showed clear band-gap semiconducting properties, at least in the range of temperatures (5 to 300K) where the resistivity has been measured. However, the „knick“ of the Arrhenius-plots at high temperatures, especially observed in the samples grown in Ar, could be a hint for band-gap activated transport at higher temperatures ($\geq$300K). Searching for another transport mechanisms, the less resistive samples (OX 3,AR 1), which are at the same time the ones with best ferromagnetic properties, showed a clear linear relation when plotting $\ln\rho$ against $T^{-1/4}$, as observed in Fig.4.34, suggesting that ferromagnetism will be favoured when the semiconductor is in the Anderson-localized state. Such correlation points towards the spin-split impurity band model of Coey et al.[10], which infers that the existance of a donor-derived impurity band is crucial for ferromagnetic ordering.

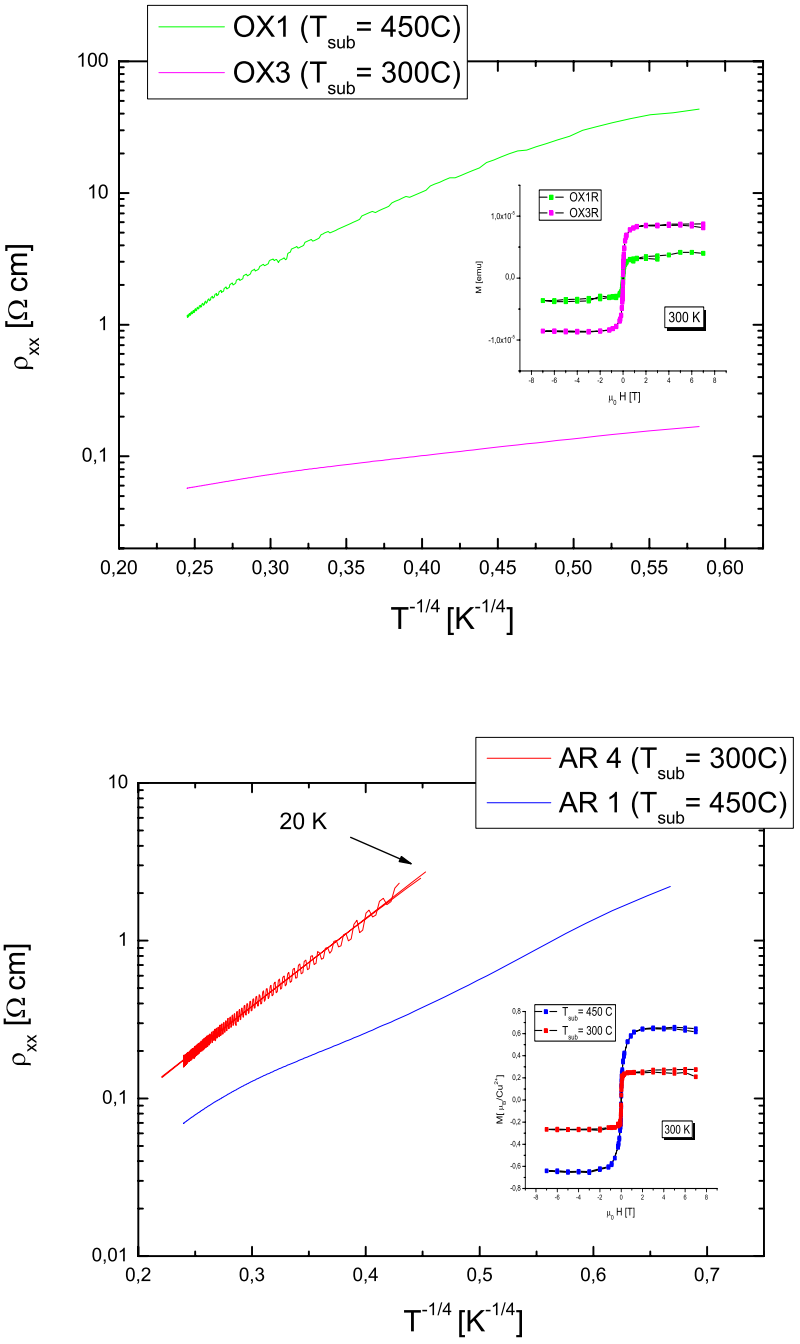

Figure 4.34: lnρ vs $T^{-1/4}$ plots, showing a better linear relation for samples in the low-resistive range. The high-resistive sample in Ar showed a large noise signal below 20K (not plotted). To highlight the correlation between magnetic and transport properties, the respective magnetization curves are shown as insets.

All the samples considered up to this point have a thickness of around 30nm. In order to study if potential defects induced at the substrate-film interface have a contribution to the transport behaviour, the sample AR 1R, prepared under identical conditions as AR 1, but with a thickness of 103nm, will be analized with the same procedure. Fig (4.35 shows that the linear relation is not homogeneous across the temperature range, when plotting lnρ vs $T^{-1/4}$. A „knick“ is observed around 100K, which divide the curve in two linear ranges. This behaviour is difficult to interpret. A linear relation suggests that the semiconductor is in the Anderson-localized-state, where the transport is governed by variable-range hopping between the strongly localized electronic states. So that the two clear linear ranges which can be distinguished in Fig.4.35, may point towards a mixed-type hopping, which can be caused by the presence of two defect bands with strongly localized states, which come to an overlap to generate a broader range of „hopping“ energies. It should be mentioned that this kind of behaviour has not been reported yet in TM-doped ZnO.

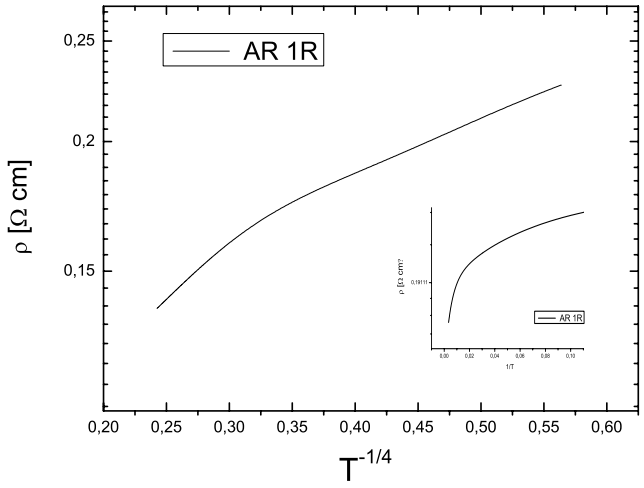

Figure 4.35: lnρ vs $T^{-1/4}$ behaviour of the sample AR 1R (103nm thickness). A continuous linear relation was not observed, as in the sample with 30nm thickness (AR 1) prepared under the same conditions. Inset shows the Arrhenius plot (lnρ vs T^{-1}).

Tiwari *et al.*[32] observed a sharp transition between band gap insulator and Anderson-localized insulator, where the measurement curves in both states (ln$\rho \propto T^{-1}$ and $T^{-1/4}$,respectively) showed perfect linear relations. However, it should be underlined that his work referred to ZnO thin films with no transition metal doping. Therefore, the suggestion that another defect band may be involved in the transport mechanism, is not that unlikely. In the case of Cu-doped ZnO samples, the deviation of

the linear behaviour by plotting lnρ vs $T^{-1/4}$ could be presumably adressed to the influence of the Cu-impurities. Another interesting observation which could be extracted from the temperature-dependent transport measurements, is the variation of the absolute values of the resistivity. The less resistive samples in each growth atmosphere (AR 1,OX 3) and especially the sample AR 1R, show a very small change of the resistivity values when decreasing the temperature from 300 to 5K (not even factor 2 in the case of AR 1R, as observed in Fig4.35), fact which support the idea of Anderson-localization in a defect band with hopping transport, at least in the temperature range under discussion. In contrast to band-gap activated semiconductors with flat defects, the carrier concentration will not depend exponentially on the temperature. The results regarding carrier density will follow in Section 4.2.5.
Summarizing, for a quantitative description of the charge transport in Cu-doped ZnO thin films, four different aspects have to be considered:

- the intentionally introduced defect levels, such as oxygen vacancies, tuned through the background gas type and pressure during growth,
- the structural defects related to the crystal growth, tuned through the substrate temperature used for preparation, and influenced by the choice of the substrate (substrate-film mismatch),
- the residual native defect levels, such as Zn-interstitials, present in the crystal structure of undoped ZnO and responsible for the unintentional n-type conductivity,
- the partially filled Cu-3d spin-down states which will introduce energy levels located in the bandgap of ZnO.

From this four factors, only the first two can be really controlled by choosing the proper process parameters. The residual native defects are shallow donors and responsible for the n-type character of undoped ZnO[31]. Up to now, only one recipe with high reproducibility has been reported, which eliminates or compensates this native shallow donors in order to produce p-type ZnO [17]. The location of the Cu-3d states in the bandgap of ZnO is up to now a controversial issue, since several ab-initio calculations of the density of states (DOS) deliver totally different results [39, 40, 41, 42]. It has been even predicted that the spin-down Cu 3d-states may lie near the conduction band [39], while other reports calculated energies near 0.8eV [42] below the conduction band, and further calculations adress the location of the 3d-states near the valence band and point out a possible p-d hybridization with the O-2p states [40, 41]. This discrepancies do not help to interpret the complex defect structure of Cu-doped ZnO

films. In addition, it is worth to point out this ab-initio calculations only consider one defect source: the doping through Cu-impurities. According to the experimental results, the samples grown at moderate substrate temperatures (300°C,450°C) and lower pressures (p=1 x 10^{-2}mbar), are found to be in the Anderson-localized insulating state, where the localization of electronic levels is due to structural disorder. In fact, both T_{sub} and growth pressure have an impact on the structure of Cu-doped ZnO films: the lower pressure will increase oxygen non-stochiometry, causing strain in the ZnO-lattice [16] and the moderate growth temperatures will lead to high mosaicity and less crystalline quality (see Section 2.2). Tiwari *et al.* [32] found a transition between band-gap insulator and Anderson-localized insulator with increasing oxygen nonstochiometry, suggesting that the strain produced by oxygen vacancies plays an important role for the localization of the electronic levels. According to [32], electrical transport in oxygen deficient Anderson-localized ZnO films is thus dominated by the variable-range hopping conduction of charge carriers between the localized states, matching with our experimental observations, since the $\ln\rho \propto T^{-1/4}$ relation could be well confirmed for samples grown at low pressures both in oxygen and Ar-atmosphere. It is worth to mention that the only sample which showed band-gap activated transport is the one with the best crystallinity (T_{sub}=650°C) and less oxygen vacancies, which means less structural disorder. Unfortunately, films with higher oxygen pressure could not be measured due to its high insulating character, supported, in addition, by the effect of Cu-dopants, which are known to increase the resistivity of unintentionally doped n-type ZnO.

In addtion, a clear correlation between conductivity and magnetic properties could be confirmed both in samples grown in Ar and O_2 atmosphere. These empirical observations suggest that ferromagnetic ordering in Cu-doped ZnO will be favoured by the formation of an impurity band with localized electron states, created by either structural or intentionally introduced donor defects, or a mixture of both. The fact that the samples with the highest magnetic moments (AR 1(R), OX 3) are the ones which have a linear relation when plotting $\ln\rho \propto T^{-1/4}$, support this intepretation. The Anderson-localized insulator state, implies the existance of an impurity band, where the transport is dominated by variable-range hopping. According to the spin-split impurity band model [10], the key for achieving high Curie temperatures is the hybridization and charge transfer from the partially filled 3d-TM states with the impurity band at the Fermi-level.

Coey *et al.* also suggested that there is growing evidence for another source of magnetism in diluted magnetic oxide films, besides the cations with 3d-electron character, pointing out that defects at the substrate-film interface may also be involved, forming an impurity band which could be polarized by the exchange with 3d cations.

Taking into consideration the experimental results and the theory models, a feasible picture of the origin of ferromagnetism in Cu-doped ZnO would be the hybridization of the Cu-3d spin-down states with the donor-derived impurity band created by oxygen vacancies at $\approx$ 1.0eV [16] below the conduction band, or with the impurity band created by the crystallographic defects. In any case, the impurity band will not be located at shallow levels, so that the hybridization with the Cu-3d-states, which are supposed to lie well below the conduction band, is indeed possible. A shallow level is not necesarilly required for conduction, since the electrical transport will be governed by variable-range hopping within the impurity band(s). Further tests on the ferromagnetic nature of Cu-doped ZnO films will be carried out by magnetotransport and hall-effect measurements, topics which will be discussed in the next sections.

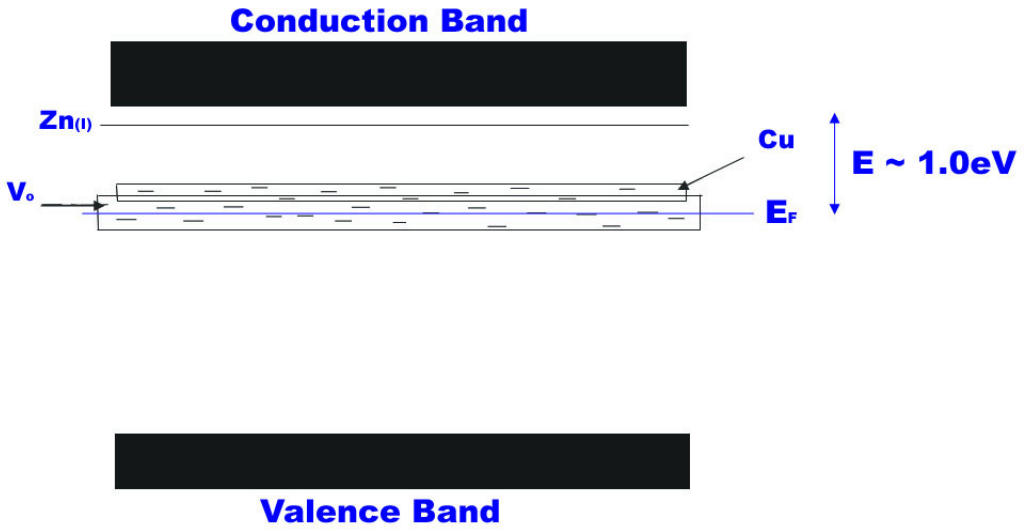

Figure 4.36: Possibility of hybridization between the band formed by donor defects (in this case oxygen vacancies) and the Cu 3d-spin-down band, at approximately 1.0eV below the conduction band [16, 42]. The localized electronic states are represented by the short dashed lines in the bands. The charge transport will be governed by variable range hopping within the localized electronic states of the hybridizing bands. The Fermi-level is within the bands, so that the shallow Zn-interstitial will not contribute to the electronic transport. The spin-split impurity band model [10] is only applicable in this scenario.

In conclusion, a correlation between structural defects and transport mechanisms could be found in this study, as well as a tentative picture based on the spin-split impurity band model, which attempts to explain the origin of ferromagnetism in Cu-doped ZnO system according to the empirical observations.

Magnetoresistive(MR)-effect

In general terms, the dependence of resistivity on an external applied field is associated with the change of collision times (free mean paths) of the free carriers. A positive magnetoresistive effect is attributed to the Lorentz-force (eq.(1.18)), which will bend the trayectories of the free carriers and reduce their effective free mean paths, so that higher external fields will cause an increase in the resistivity. The negative magnetoresistance, which implies a decrease in the resistivity with increasing magnetic field, is attributed to spin-scattering. High fields will align the spins of ferromagnetic materials, reducing the spin-disorder and hence reducing the resistivity.
In order to investigate the magnetoresistive properties of Cu-doped ZnO, the resistivity of the films was measured by changing the field from 14T to -14T and back, at a constant temperature. Not all samples could be measured down to low temperatures, since the high-resistive samples showed a large noise-to-signal ratio. The films grown at moderate temperatures (300,450°C) and lower pressure (10^{-2}mbar) could be investigated in a wide range of temperatures.
Starting with the films grown in oxygen, they exhibit in general a negative magnetoresistance which decrease with increasing temperature. The sample grown at T_{sub}=450°C, delivered large noise signals at $T \leq$25K, due to its high resistivity (see Section 4.5.1), but the low resistive one (T_{sub}=300°C) showed a large negative MR-effect (≈15 percent) at low temperatures. The magnetoresistive MR-effect is defined as

$$MR = \frac{\rho(H) - \rho(0)}{\rho(0)} \tag{4.11}$$

Comparing the MR-values from both samples at different temperatures, the larger effect will always happen at the sample with lower resistivity, which lies well in the Anderson-localized state and has among both the highest magnetic moment (OX 3), determined through SQUID-magnetometry. Since the negative MR is attributed to the decrease of scattering rate through spin order, its correlation to the ferromagnetic properties is expected.

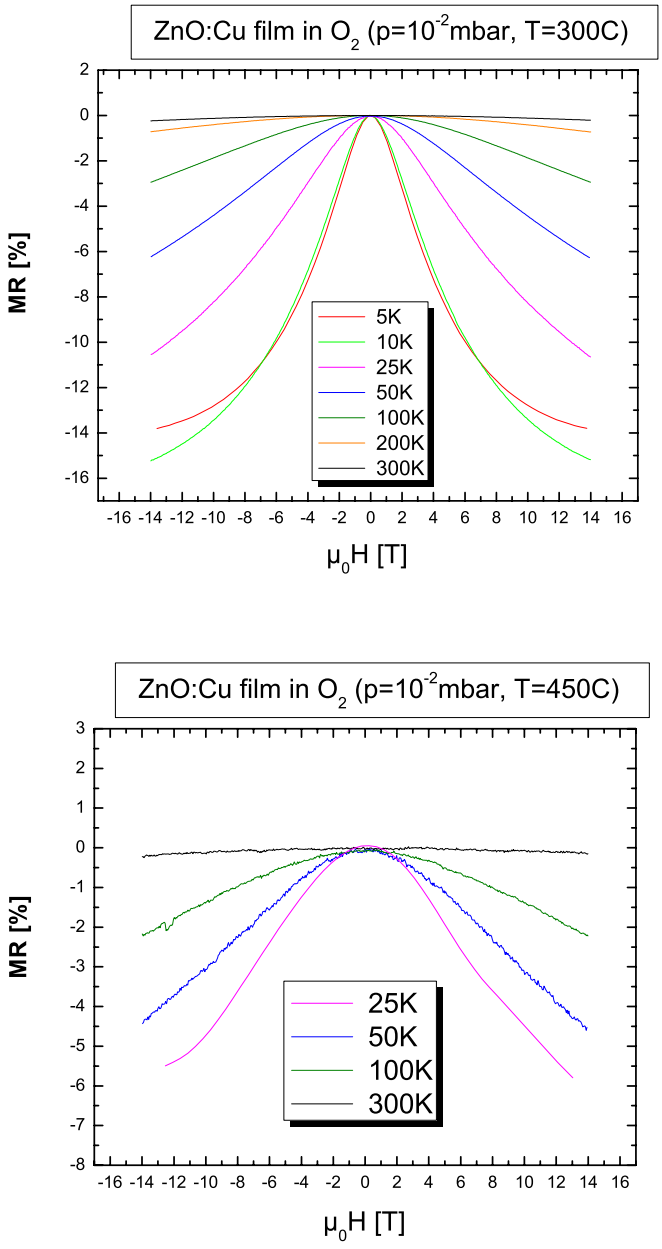

Figure 4.37: Magnetoresistance in samples grown in oxygen atmosphere. Note that the high resistive sample could not be measured down to 5K. Interestingly, the sample with the larger MR has the higher conductivity and at the same time, the better magnetic properties.

Andrearcyzk *et al*. studied the magnetoresistance of n-type ZnO:Al and ZnMnO:Al, and assigned the observation of a large negative MR-effect in TM-doped ZnO to the formation of bound magnetic polarons, while a positive MR was explained in terms of s-d coupling between the partially filled 3d-states of the transition metals and the s-states of Zn which lie in the conduction band. This model described by [43] was suggested for systems in the weakly localized regime, close to the metal-insulator (MIT) transition, since in his work, ZnO was doped with Al to increase the number of carriers. On the other hand, for DMS which are in the strongly localized regime, a negative MR points to the presence of a coupling between localized spins and charge carriers. In a DMS at the localization boundary, there is a coexistance of spin-related positive and negative MR: the former coming from the s-d splitting of the conduction band and the latter tentatively coming from the formation of bound magnetic polarons [43]. Considering our experimental results, as observed in Fig (4.37), the largest negative MR-effect will be observed at the sample in the Anderson-localized state. This finding is consistent with the interpretation described above about the significance of positive and negative MR-effect in the several localization stages.

Regarding the samples grown in Ar-atmosphere, the same correlation was found as in the oxygen case: the strongest MR-effect was found in the sample with better conductivity and higher magnetic moment (AR 1 /AR 1R). But the MR-behaviour in the sample AR 1 at low temperatures was quiet surprsing: a large positive MR-effect was observed at 5K, with a negative component at low fields (Fig 4.38). The positive component decreased at 10K, not being able to overcome the negative one, which extended to higher fields. Such an interplay was observed by Andrearczyk *et al*., and attributed to the competition between s-d coupling and weak localization effects of n-type ZnO. The field range in which the „hump“ is overcome, is quiet different: around 5T for Cu-doped ZnO and around 0,8T for Mn-doped ZnO in [43]. Since the sample AR 1 shows to be in the Anderson-localized state according to ρ(T) measurements, it is questionable in how far the model should be considered.

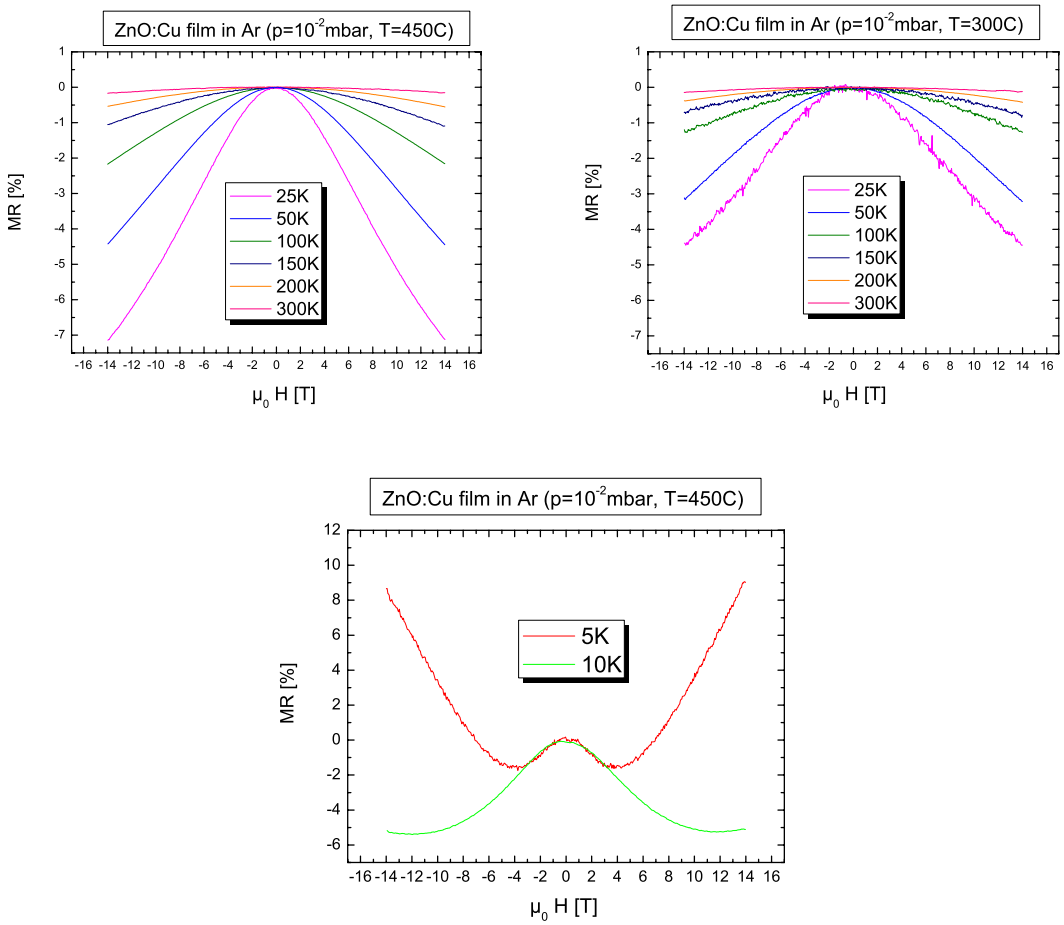

Figure 4.38: MR-effect in samples grown in Ar, plotted in the same scale. Note that the high-resistive sample AR 4 could not be measured down to low temperatures, and that its MR-effect is clearly shorter. The less resistive sample AR 1 showed a large positive MR at 5K, plotted separately for better observation.

Reuss et al.[44] studied the magnetoresistance of unintentionally doped ZnO at various carrier concentrations, measuring both a positive (2-10K) and negative MR-effect up to large fields (15T), presented in Fig.4.39. This suggested that both positive and negative MR may occur at undoped ZnO as well. By increasing the n-type carrier concentration, he found that the positive contribution present at low temperatures was suppressed at large fields. For the interpretation of his findings, he used a semi-emprical model which considered a third-order s-d Hamiltonian [45] to describe the negative MR contribution observed all over the temperature range. The conclusions of this work were that a positive MR only appears in undoped ZnO at high fields and low temperatures ($T \leq$10K) and vanishes with increasing carrier concentration ($n \geq$1 x 10^{19}), as observed in Fig.4.39 According to this model, the „hump“ seen in

the sample AR 1 at 5K could be identified as a feature of undoped ZnO, but not the large positive MR ranging up to 8%. As a result, the origin of the large positive MR-effect of AR 1 at 5K, could not be clarified, taking into account both models. Nevertheless, it has been shown that positive MR is not necesarilly a characteristic of ferromagnetic semiconductors.

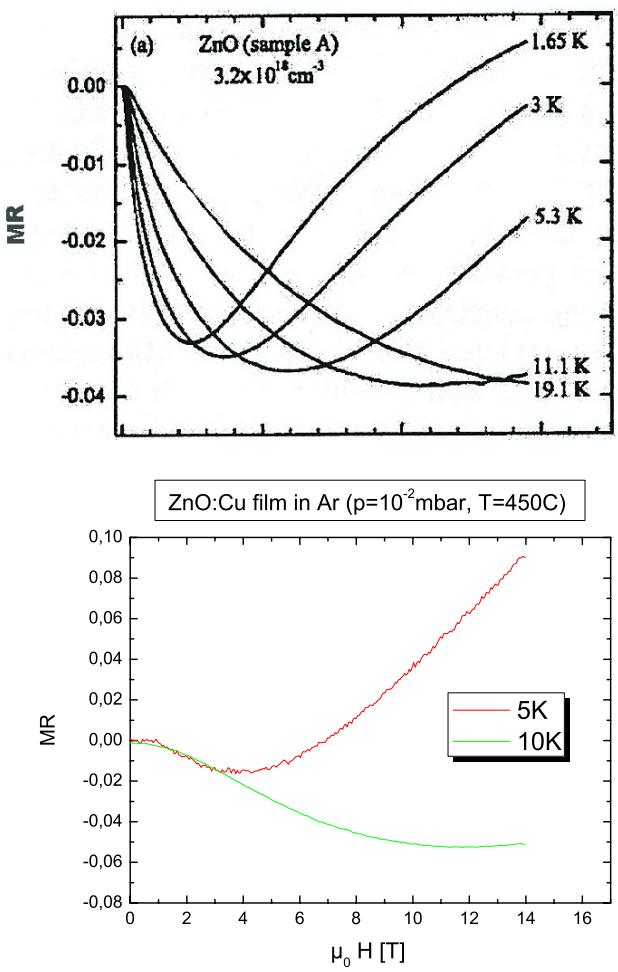

Figure 4.39: Comparison between the positive MR-effect measured by Reuss *et al*[44] at undoped ZnO (up) and the lone Cu-doped thin film sample (AR 1) which showed positive MR at low temperatures (down). The field range is the same for both measurements.

Neglecting the lone sample which showed a large positive MR at 5K, the qualitative comparison of the magnitude of the negative MR-effect in undoped ZnO [44] and the Cu-doped samples presented here, shows another clear evidence that a much larger negative contribution (% 15 against % 4) is due to the ferromagnetism induced by Cu-doping, reducing the scattering rate and hence the resistivity through spin order. At temperatures T$\geq$ 25K, all the samples, regardless of its preparation conditions,

show a negative MR, which decreases with increasing temperature. The magnitude of the MR-effect, as stated before, is correlated with the strength of the magnetic moments of the samples.

In summary, the common feature of Cu-doped ZnO is to exhibit a large negative MR-effect at low temperatures, decreasing gradually as the temperature rises. The MR-effect at room-temperature is substantially weaker ($\leq$0,5%). In the low temperature regime, a very weak positive contribution arises at high fields, flattening the dominant negative component. The sample AR 1 was the exception, since the positive contribution appears at intermediate fields (4T) and dominates as the field is increased, resulting in large positive MR, magnitude which could not be really explained by the two models which were discussed [43, 44] It is worth to mention that the sample AR 1R, grown under the same conditions, but five times thicker, did not show the large positive contribution (see Fig.4.40) suggesting that the substrate-film interface defects and their role on the early stages of growth may be involved.

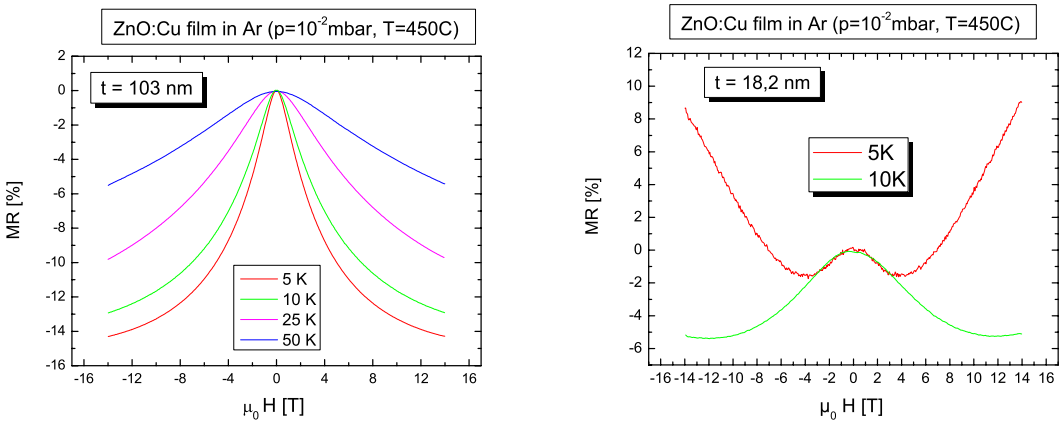

Figure 4.40: From samples AR 1 and AR 1R, grown under identical conditions, the one with less thickness (t=18,2nm) showed a large positive MR at 5K.

A study of the magnetoresistance as a function of structural disorder in Anderson-insulators was done by Vaknin et al.[46]. In that work, a quantitative study of the magnetoresistance of In_2O_3 thin films as a function of thickness was performed, and a positive MR was observed as the structural disorder increases (as the thickness decreases). However, the models used in [46] are applicable for undoped Anderson-insulators, which means that this effect has rather to do with carrier transport than with the ferromagnetism induced by the Cu-substitution. Still, it provides useful information about the role of strucural disorder on the magnetoresistive effects, and suggests a tentative explanation why the positive MR-effect is present just in the

sample with less thickness. About the magnitude of the effect observed in AR 1, there is still uncertainty. A quantitative study could not be performed due to the reduced items (1) which showed that kind of behaviour.

Hall-effect

The Hall-effect in pure semiconductors has been discussed in Section (4.2.5). But the situation changes, if there are magnetic atoms introduced in the lattice of the host semiconductors: the mobile carriers will not only bend their trajectories due to the external applied field, but also due to their interaction with the polarized atoms (spin-spin and spin-orbit interactions). Crucial for the observation of the hall effect due to the interaction of carriers with magnetic impurities, is that the magnetic moments of the introduced impurities are aligned in the same way, so that a homogeneous spin-orbit interaction sets in, as depicted in Fig (4.41). In other words, an intrinsic ferromagnetic ordering is needed to macroscopically observe the spin-orbit interaction, so-called „anomalous hall-effect“.

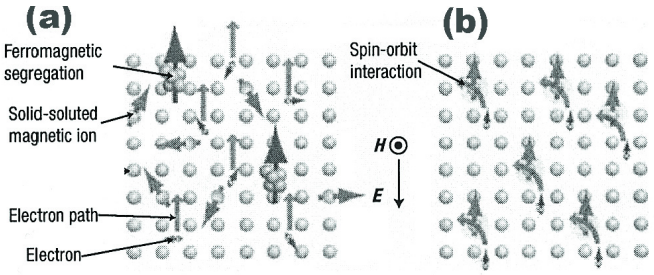

Figure 4.41: Picture describing the origin of the anomalous hall effect, through spin orbit interaction, taken from [19]. (a) shows a semiconductor with extrinsic ferromagnetic sources, and (b) intrinsic ferromagnetism.

That means, there are two separate contributions to the hall-voltage (and hence to the hall-resistivity ρ_{xy}) in a ferromagnetic semiconductor, which are described through following equation:

$$\rho_{xy}(H) = R_0 \cdot H + R_{ahe} \cdot M(H) \tag{4.12}$$

where R_0 and R_{ahe} are the ordinary and the anomalous hall-effect coefficient, respectively. Since the anomalous contribution is proportional to the magnetization M(H) of the sample, the effect will be rather observed at low fields, when there is a strong change in the magnetic moment, as observed in the hysteresis loops M(H) obtained by SQUID-magnetometry (Section 4.2.4). To be able to observe the aimed anomalous contribution, however, was not an easy task. The first problems arised due

to a superposition of the ρ_{xx} and ρ_{xy} components when measuring the Hall-voltage. The reason was a slight tilting between the two U_H contacts in respect to the perpendicular current stripe (Fig 2.9), leading to a diagonal path to be covered by the carriers. The magnitude of the superposition component was around 1/100 of the absolute ρ_{xx} value, which corresponds a distance of 3,5μm, difficult to control by the standard optical litography methods used to pattern the structure. Fig 4.42 sketches the as-obtained R_{xy} Hall-curves and the absolute values of R_{xx}. The superposition can be clearly observed since the shapes of R_{xy} and R_{xx} are clearly correlated. As the sheet resistance decreases, the Hall-slope will be less influenced, fact which confirms that this phenomena is due to the superposition and not due to any contact failure, cross-over or substrate effects.

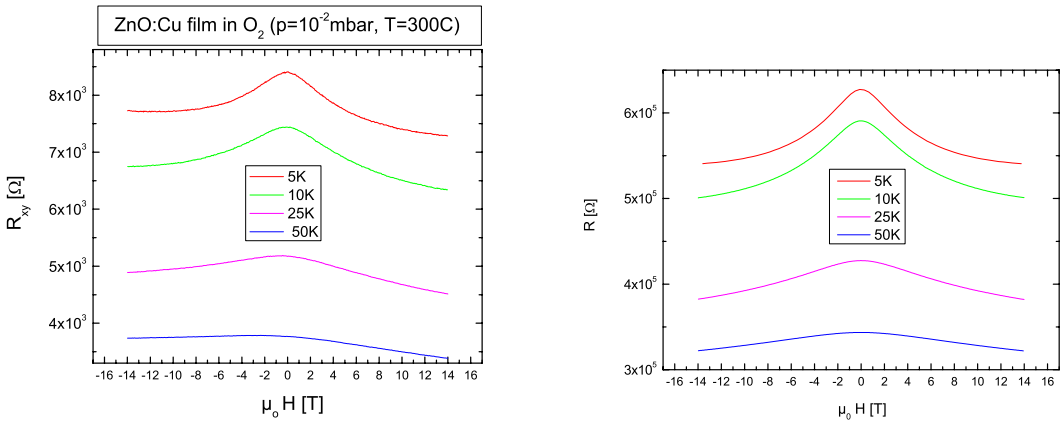

Figure 4.42: Example of the superposition of the R_{xx} component in the Hall-resistance in the sample OX 3. The effect was identified mainly through the shape and the magnitude of the sheet resistance. Note that the scaling factor is around 1/100.

Having identified the first problem, the as-obtained Hall-curves were separated in even and odd components, since the even part corresponds the contribution of the sheet resistance, which is an even function of the magnetic field. The remaining odd part will be then the real ρ_{xy} Hall-resistivity.

Apart from giving information about the intrinsic ferromagnetic nature of a dilute magnetic semiconductor, measuring the hall-effect is a versatile method to determine the carrier density in a conducting material. The carrier concentration will depend directly from the ordinary hall coefficient, as

$$R_0 = \frac{1}{ne} \tag{4.13}$$

That means, the slope of the ordinary hall-contribution, according to (eq 4.15) will

determine both carrier type and density. In the present work, the carrier density of all the samples under discussion could be determined at room temperature, even the ones grown at high pressure. Electrons have been found to be the majority carriers in the Cu-doped ZnO samples. Since the pressure used for growth has found to be critical in terms of conduction, only the samples grown at the lowest oxygen pressure (and in Ar-atmosphere) could be investigated in a wider range of temperatures. The pressure dependence of the carrier density is shown in Fig (4.43) for the samples grown in oxygen.

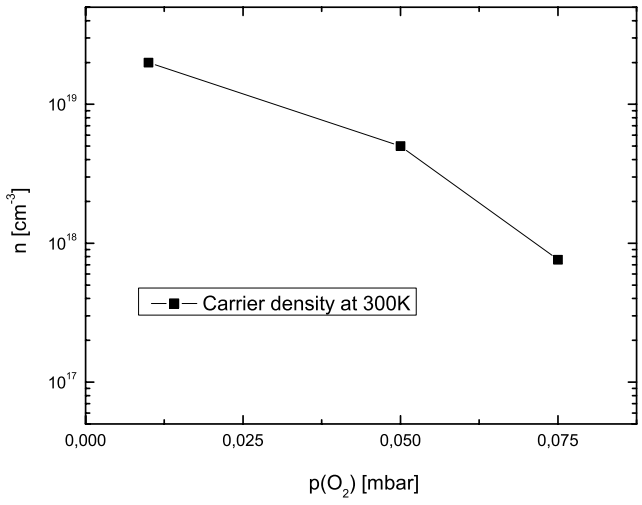

Figure 4.43: Variation of the room-temperature carrier density with the oxygen pressure used for film growth.

For the less resistive samples, the carrier density could be obtained down to low temperatures. Above temperatures $T \geq 50$K, the carrier density increases very slow with increasing temperature. This behaviour confirms again that the transport in the conducting samples is not governed by band-gap activation, and rather by hopping within the impurity band. Assumming a transport between a flat defect level and the conduction band, an exponential growth of the carrier concentration would have been expected, as n $\propto \exp(\frac{\Delta E}{2k_B T})$. The n(T) behaviour of the Cu-doped ZnO samples is depicted in Fig 4.44. The determination of the carrier density at low temperatures was not that accurate for the samples where anomalous and ordinary contribution were competing. The less resisitve sample grown in oxygen (OX 3) is the only one which could be characterized in terms of carrier concentration down to low temperatures, since the anomalous contribution was very weak. An extensive study of the anomalous

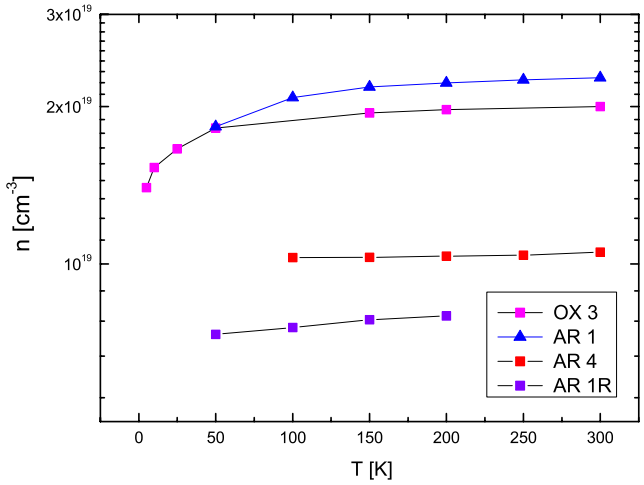

Figure 4.44: Carrier density vs temperature in the less resistive Cu-doped ZnO thin films. Note that the absolute range and the behaviour do not vary critically with the preparation conditions.

contribution will follow later.

All the samples which were found to be in the Anderson-localized state, showed a very small increase in the carrier concentration with increasing temperature. The range of carrier densities vary from 7 x 10^{18} to 2 x 10^{19}. Interestingly, the samples AR 1 and AR 1R, grown under identical conditions but with different thicknesses, showed a very similar behaviour but different absolute values of the carrier density. This suggests that in thin films (AR 1: t= 18,2nm), which are stronger influenced by induced substrate-film interface defects, a higher amount of carriers will be available for hopping conduction.

Taking into account the resistivities, it can be concluded that the sample AR 1 which has the highest carrier density and the highest resistivity at low temperatures, results to be the one with less carrier mobility. In the low temperature regime, the scattering of carriers through lattice vibration can be neglected, as the scattering with impurities or structural defects become dominating. Since the film AR 1 crystallizes in the early stage growth of Cu-doped ZnO on sapphire, the first layers will experience strain forces thus inducing a certain aperiodicity of the crystal potential. In that case, the electron waves will increase their scattering rate, producing a decrease in the average mobility. However, the critical thickness, where the the film relaxation occurs, could not be determined in Cu-doped ZnO. Chen *et al.*[25] could visualize this transition by means of RHEED(Reflection High Energy Electron Diffraction) characterization, observing

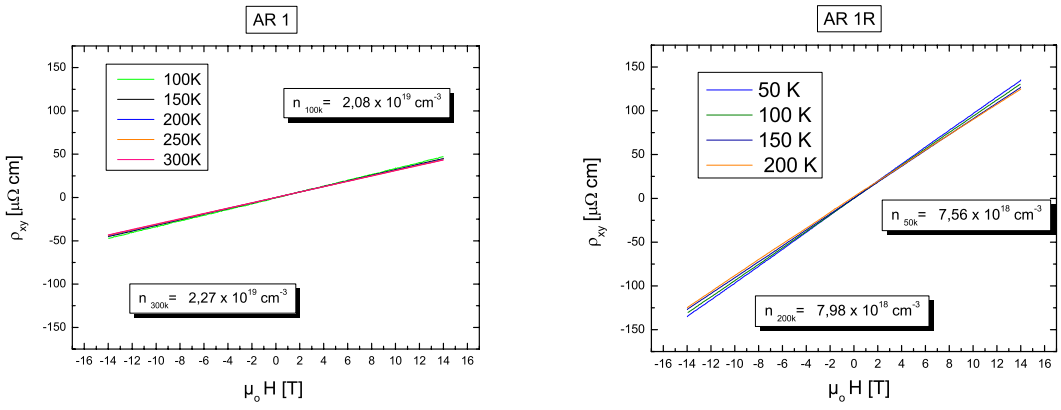

Figure 4.45: Comparison of samples grown under the same conditions but with different thicknesses (AR 1: 18.2nm, AR 1R: 103nm). The same scale is used for the Hall-resistivity, to enable a better comparison.

a shift in the reflection patterns. He found the growth of ZnO on sapphire consists of a region with high density of structural defects near the interface, which extends up to 5nm. There is another structural factor which may affect the mobility, which has to do with the columnar growth of ZnO on sapphire, namely the scattering at the defects produce by column boundaries. As the film thickness increases, two factors have to be considered: First, the subsequent crystal layers are less influenced by substrate-film interface defects, and the crystal potential will recover their periodicity, decreasing the electron scattering rate and hence increasing the average mobility. Second, the columnar grains will collect together and form c-axis oriented columns with bigger diameter [28], decreasing the number of column boundaries. This turns out to be a reasonable explanation for the observed phenomenology. In addition, it is supported by the work of Kishimoto et al., who studied the mobility dependence of the film thickness for undoped ZnO thin films[28], concluding that the carrier concentration will not vary critically, whereas the mobility increases with increasing thickness up to a critical value (≈130nm) for samples grown under the identical conditions.
As observed in Fig.4.46, the carrier mobility, defined as

$$\mu(T) = \frac{1}{n(T) \cdot e \cdot \rho(T)} \tag{4.14}$$

will depend on the carrier density and the resistivity in the same way, as ($\propto 1/x$). The constant e is the elementary charge. Thus, the mobility will be dominated by the product of carrier density and sheet resistivity. In the studied Cu-doped ZnO films, the mobility will increase with temperature due to the decrease of the resistivity,

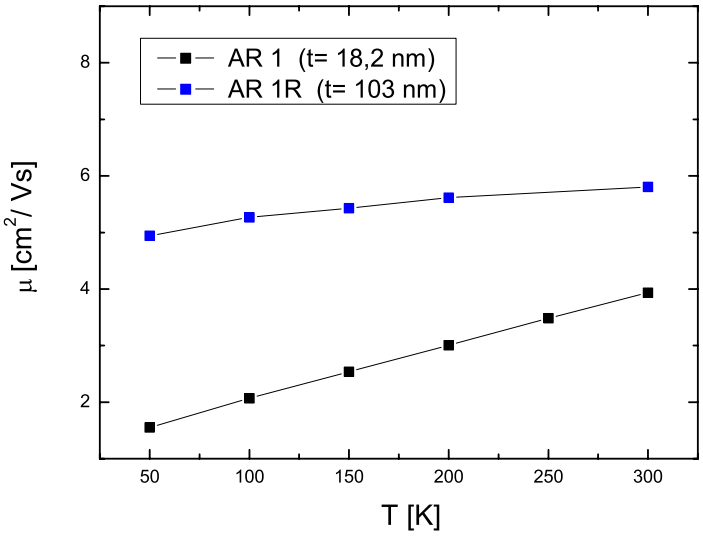

Figure 4.46: Electron mobility of samples with different thicknesses but grown under identical conditions. Note that the thinner sample will always have a lower average mobility in the presented temperature range. The mobility will increase with temperature due to the decrease of the sheet resistivity, which dominates against the weak temperature dependence of the carrier density between 50 and 300K.

since the carrier concentration remains nearly constant in the temperature range from 50 to 300K. At temperatures (T$\leq$50K), the presence of a strong anomalous hall-effect signal did not permit the calculation of the carrier densities with good accuracy in the sample AR 1R (t=103nm), while for the sample AR 1 a larger noise-to-signal ratio arised at low temperatures, due to the higher sheet resistivity values and reduced thickness. The correlation between ordinary and anomalous hall effect will be presented next. Since the samples presented in Fig.4.46 have been found to be in the Anderson-localized state, where the transport is governed by hopping between the localized electronic states, the carrier concentration is not expected to increase exponentially with temperature, as in the case of a band-gap activation.

The anomalous hall-effect contribution was observed at the three samples which could be measured down to 5K (AR 1, AR 1R, OX 3). As a general feature of this Cu-doped ZnO film series, the anomalous contribution could be hardly detected above 50K, falling into the noise of the measurement signal (ρ_{xy} $\approx$1$\mu\Omega$cm). To trace after an anomalous contribution at room-temperature, was quite hopeless.

Starting with the lone film grown in oxygen, which could be measured down to low

temperatures, a weak anomalous contribution was observed at 5 and 10K. Unfortunately, the signal-to-noise ratio was too low to proceed with a quantitative analysis. This weak anomalous hall-effect was not detectable at 25K any more, as observed in Fig (4.47). Nevertheless, an evidence of intrinsic ferromagnetism was found in the sample OX3 at low temperatures.

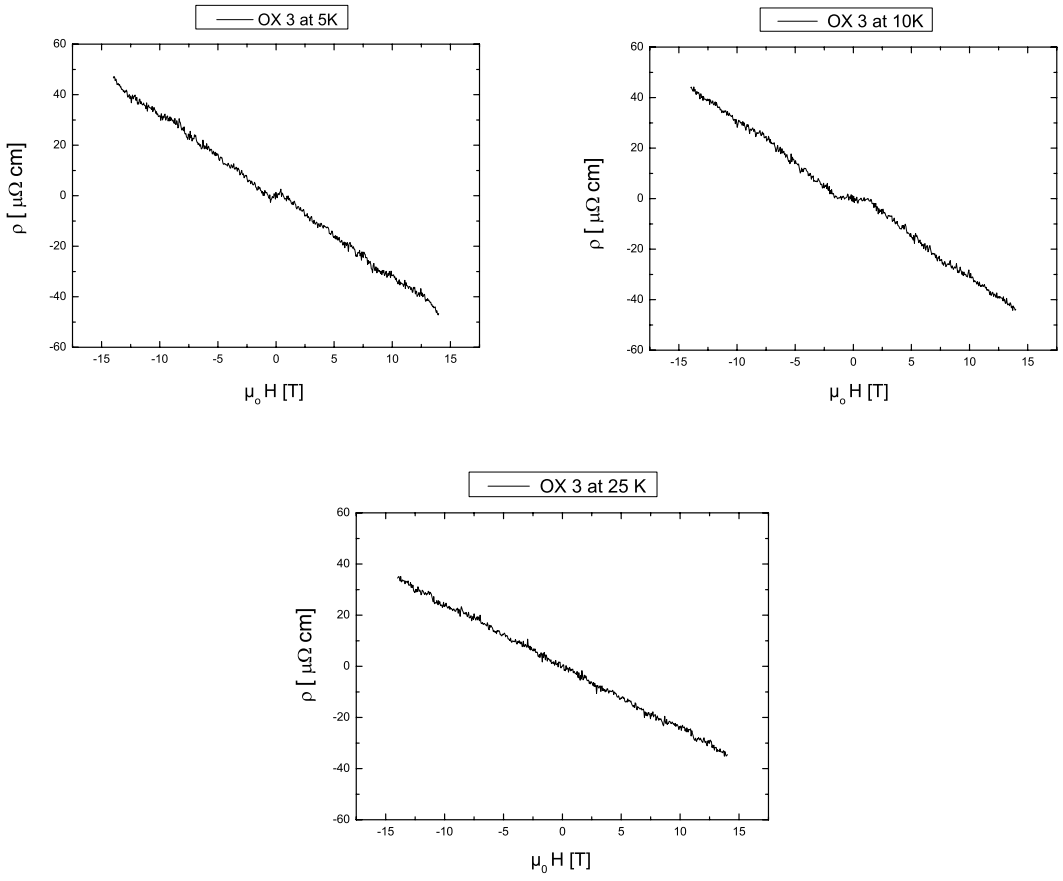

Figure 4.47: Weak anomalous hall-effect in the conductive sample grown in oxygen.

Regarding the Cu-doped ZnO films grown in Ar-atmosphere, the story was different. A large anomalous signal was detected in the sample with greater thickness (AR 1R) up to 25K, while in the thinner sample AR 1, a moderate anomalous contribution was observed only at 10K, but with large noise. Since the resistivities of both samples are in the ratio 1:4, and considering that the thicknesses are in relation 1:5, the applied current has to be 20 times larger for the sample AR 1 to achieve a relative noise-free signal. This resolution problem arised, as discussed before, because of the superposition of the sheet resistivity ρ_{xx} in the ρ_{xy} component. An acceptable signal-to-noise ratio was achieved at 10K, enough to identify the anomalous hall-effect

contribution. The signal was much better at 25 K, but the anomalous contribution decreased to the point where a further analysis was not worth. But the most surprising results were achieved at the sample AR 1R. A very large anomalous contribution appear at 5, 10 and 25K, clearly dominating over the ordinary hall-effect at low fields. At first, the results were taken with sceptisism because of its magnitude and behaviour: the anomalous contribution changed its sign between 5 and 10K. It should be underlined that the ρ_{xy} curves shown in Figs (4.49-4.51) is not the as-measured data, since it has been submitted to correction due to the superposition of the sheet resistance component. To check the validity of the data analysis, a Lorentz-function L(H) has been fitted for the as-obtained R_{xy} data at low fields, and was taken instead of the real measurement points to proceed with the symmetrization. The odd part of the function L(H) is shown in Fig(4.48), showing the same behaviour as the data taken directly from the measurement.

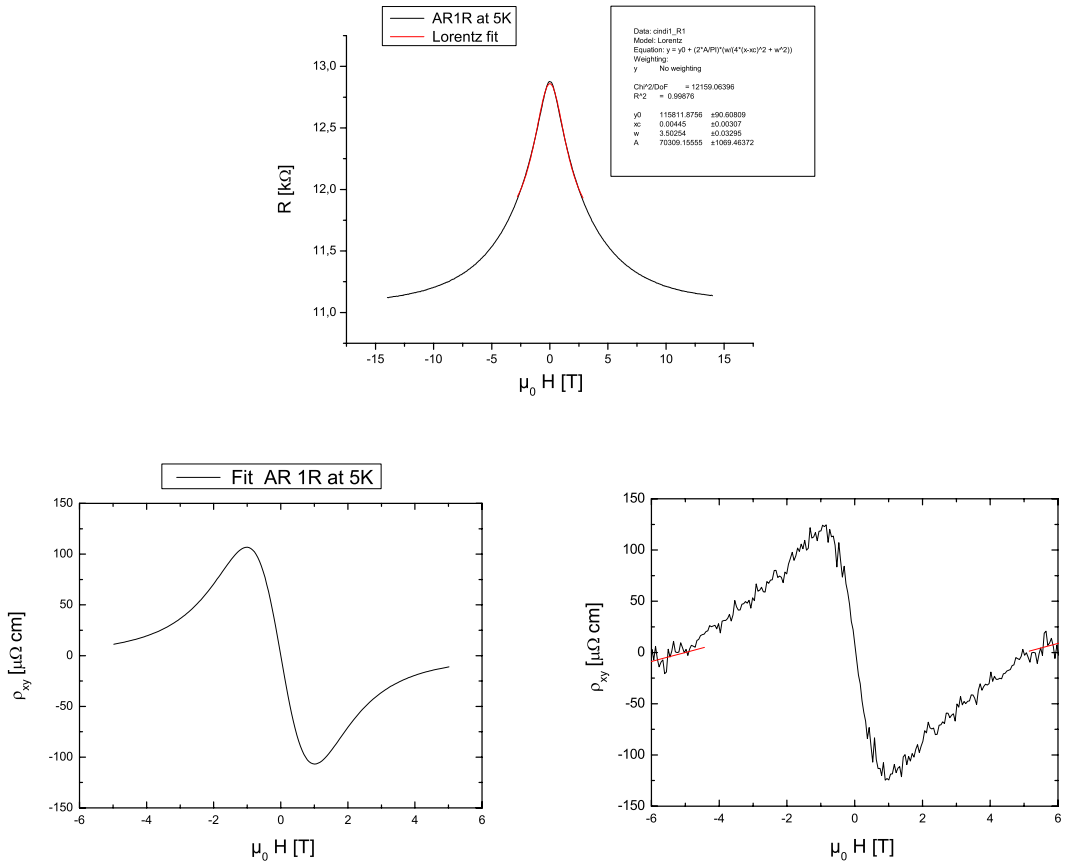

Figure 4.48: Odd part of the as-obtained R_{xy} data, once taking the measurement values (right) and once taking the Lorentz fit function (left). The as obtained data and the fit are shown above.

The strong AHE-signal at low temperatures enables a quantitative analysis. As seen in equation (4.15), the anomalous part is proportional to the magnetization M(H), which has been already characterized by SQUID-magnetometry. It is widely known that the anomalous hall-effect is origined by the interaction between spin-polarized carrier and magnetic impurity, and the two current mechanisms which aim to explain this phenomena are known as skew-scattering and side-jump [14]. The former scales with the sheet resistance as $R_{ahe} \propto \rho_{xx}$, while the latter does it as $\propto \rho_{xx}^2$, so that we could write equation (4.15) as

$$\rho_{xy}(H) = R_0 \cdot H + c \cdot \rho_{xx}^n \cdot M(H); n = 1, 2 \tag{4.15}$$

where the exponent is n=1 for skew-scattering and n=2 for side-jump, and the constant c is field independent and has dimensions of mobility [20]. For a better overview, three panels have been sketched to elucidate how the Hall-resistivity ρ_{xy} depends on the magnetization M(H) and the sheet resistivity ρ_{xx} at different temperatures and different samples. The samples to be focused on are AR 1 (t=18.2nm) and AR 1R (t=103nm), grown under identical conditions. The comparison is in such way useful, since it provides information about the role of thickness (stages of growth) on the observation of the anomalous hall-effect. The message of each panel should be the following:

- the temperature dependence of ρ_{xy} and the scaling factor ρ_{xx} in both samples (Panel 1)
- the variation between two samples with different thicknesses, at a constant temperature; and the evaluation if skew-scattering or side jump is more applicable for the observed results (Panel 2)
- the confirmation if skew-scattering or side jump phenomena suits for the anomalous hall-effect over the whole temperature range (5-25K), taking into consideration sample AR 1R (Panel 3)

Starting the discussion with Panel 1, the temperature dependence of the sheet resistivity, both in the absolute value $\rho(0)$ and the MR-effect, is clearly observed for sample AR 1R, since exactly the same scale was used to present the results. The ratio 1:4 in the absolute resistivity values between both samples could be confirmed, agreeing with the transport measurements R(T). Interestingly, the influence of the negative MR on the anomalous contribution is evident: the bending of the curve after reaching saturation at around 1T will be more pronounced, as the negative MR-effect increases. This behaviour will be discussed later refering to Panel 2. As expected, the anomalous contribution will dominate at low fields, while at high fields the ordinary

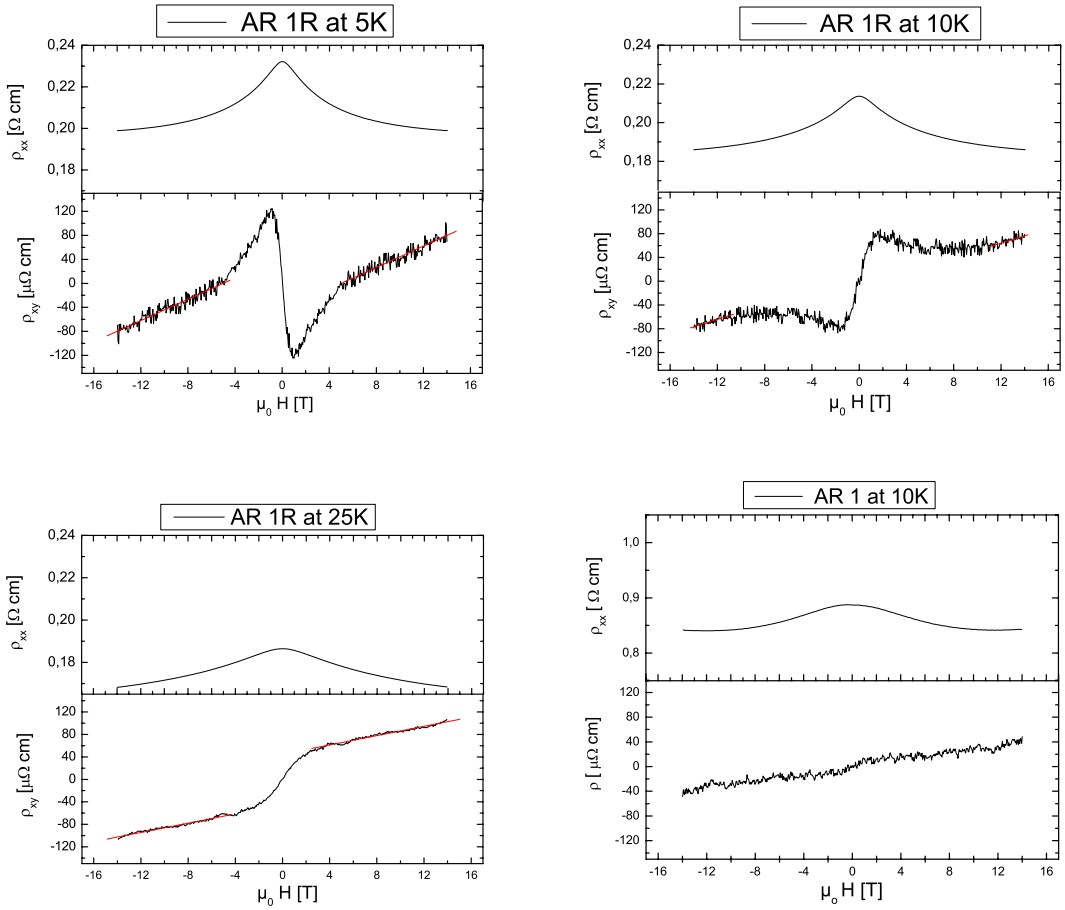

Figure 4.49: Panel 1, highlighting the temperature dependences of ρ_{xx} and ρ_{xy}. At 10K, a sample comparison can be made.

contribution becomes dominating. However, there is a region at intermediate fields where both contributions compete strongly. This effect is observed more clearly in AR 1R at 10K. As stated before, this is the reason why the carrier density determination was not that accurate at low temperatures, especially when there is a large region where the interplay takes place. In the higher resistive sample AR 1, no such ρ_{xx} dependence could be detected in the hall-resistivity, due to both the small anomalous signal and lower magnitude of the negative MR.

The most surprising result of this study is, undoubtly, the sign change of the anomalous coefficient at 5K. There are reasons which speak in favour to the validity of the measurement, such as the data-analysis check through the fit-function, depicted in Fig(4.48), and the fact, that the ordinary contribution do not change sign in the studied temperature range, as expected. A change in the sign of the ordinary contribution would mean a change of carrier type (electrons $\rightarrow$ holes) with increasing temperature

In panel 2, the magnitude of the anomalous contribution in the samples AR 1/AR 1R should be discussed, as well as a deeper look in the ρ_{xx} and M(H) dependence of the Hall-resistivity. For that purpose, the samples have been plotted in different field scales, to enable a better appreciation of the anomalous contribution in the higher resistive sample. Comparing both samples qualitatively, it can be observed that the slope of the anomalous part is broadened in the sample AR 1, matching with the broader feature of the sheet resistivity. The bending of the hall-resistivity after saturation in the sample AR 1R seems to have relation with its large negative MR-effect. For a more exact analysis, the products M(H) x ρ_{xx} and M(H) x ρ_{xx}^2, related to skew-scattering and side-jump, respectively, are shown below. It should be mentioned that, for the M(H) relations, the room-temperature hysteresis was considered, since the 5K showed a large paramagnetic contribution. As a result, for the sample AR 1R, the anomalous component is better described by the second case, where the the effect of the sheet resistivity is stronger. Regarding AR 1, the quadratic dependence seems to fit better as well, but fails to explain the slow saturation of the anomalous hall component. In the M(H) x ρ_{xx}^2- plot, the saturation is slower as in the linear case, but sets in already at 2T, while the anomalous contribution stretches up to 3-4 T, and a sharp saturation could not be observed.

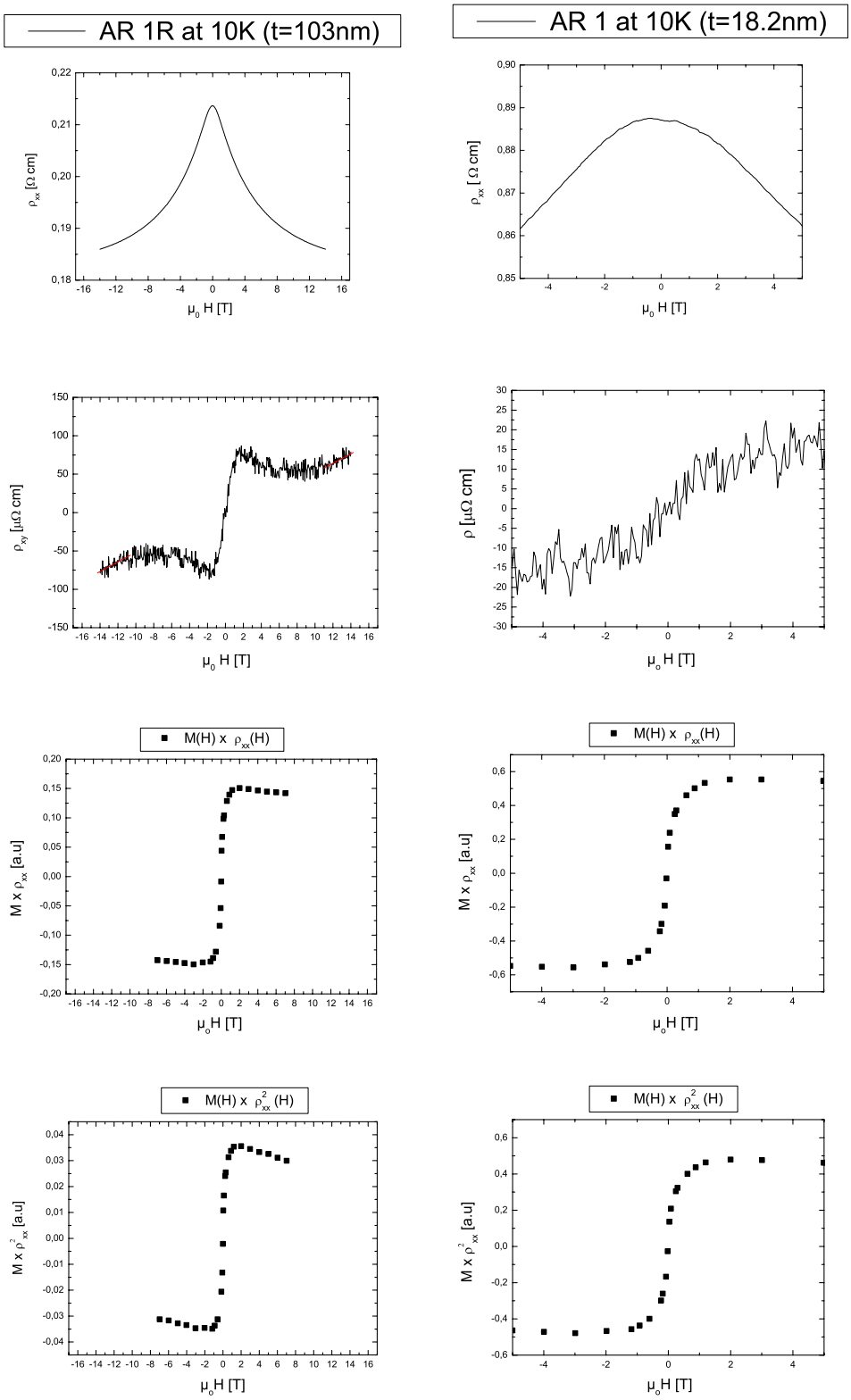

Figure 4.50: Panel 2, which compares the two samples with different thicknesses (AR 1: 18.2nm, AR 1R: 103nm) grown under identical conditions, and evaluates the scaling of the sheet resistivity considering the classical models (skew-scattering or side-jump).

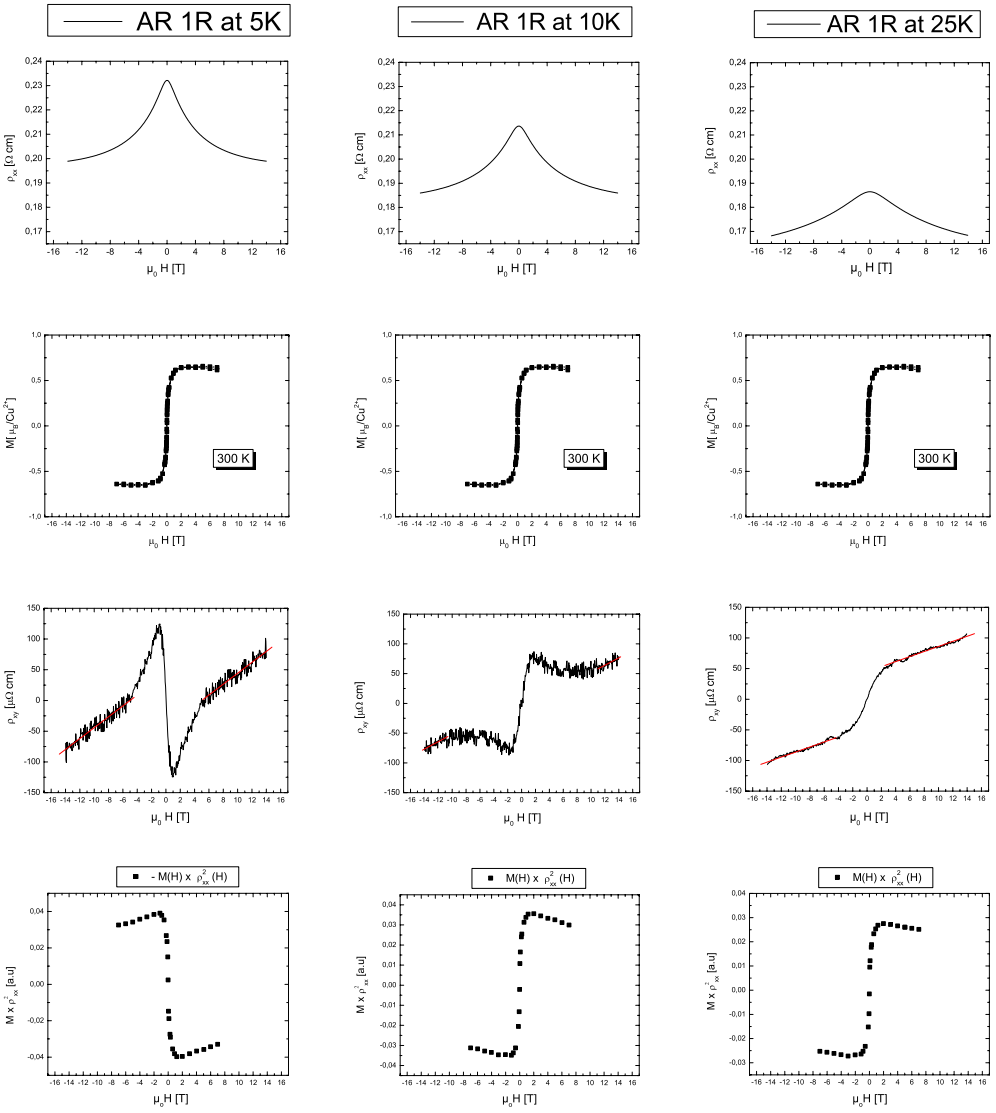

Figure 4.51: Panel 3, describing schematically how ρ_{xx}, ρ_{xy} and the product M $\times\rho_{xx}^2$ develops with temperature in the sample AR 1R (t=103nm). Each column belongs to the temperature mentioned at the top. The accuracy of the side-jump mechanism to describe the phenomenology, can be judged by comparing the last two rows.

Panel 3 concentrates on the sample AR 1R, providing a better overview of the phenomenology as the temperature increases from 5 to 25K. The quadratic dependence of the sheet resistivity has been assumed to be the best fit, and the M(H) x ρ_{xx}^2 curves are shown in the last row. The advantage of panel 3 is that all the quantities have been plotted in the same scale range, enabling a much better direct comparison. The quadratic dependence of ρ_{xx} seems to be a good fit for the 10K and 25K hall-resistivities, but fails to explain by far the strong curvature of the 5K-ρ_{xy} plot at 5K. From panel 2, it is clear that the curvature increases as the order n of the sheet resistivity dependence increases. Actually, a fit of higher order (n≥2) will match better with the anomalous contribution at 5K. However, no theory model of high-order influence of the sheet-resisitivity has been proposed so far, which could explain these experimental results. The other interesting phenomena at 5K, which is in fact the sign change of the anomalous hall-coefficient, has not been experimentally reported up to now.

Fig.4.52 shows how the absolute value of the anomalous hall-resistivity scales with the sheet resistivity, from 5 to 25K. The slope on the double logarithmic scale is the exponent n in equation (4.15), which describes how ρ_{xx} influences the anomalous contribution. As observed in the comparison panels, the quadratic relation is the one which is able to explain, at least a part of the observed phenomenology.

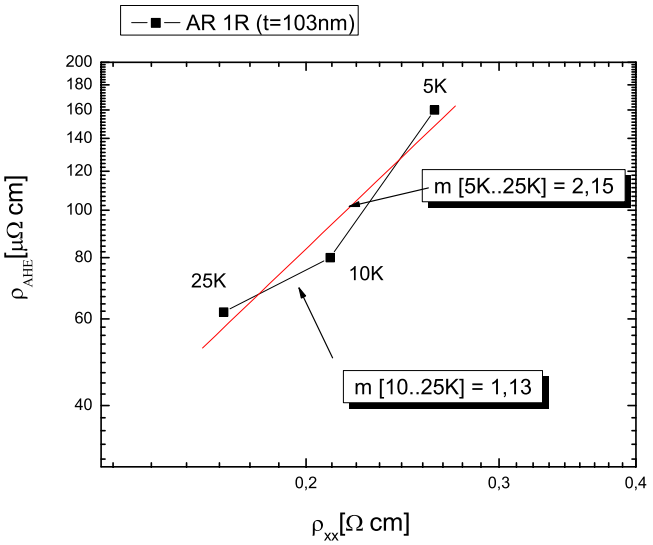

Figure 4.52: Scaling of the absolute value of the anomalous-hall resistivity ρ_{AHE} with the sheet resistivity ρ_{xx}, in double-logarithmic scale.

However, since Fig.4.52 considers only the absolute values and not the field dependance (shape) of the anomalous signal, it provides limited information. Just considering these absolute scaling, a side-jump scattering would be the best fit for the whole temperature range (5-25K) and a skew-scattering mechanism between 10 and 25K. It is worth to mention that the investigated range of temperatures and points (3) is not enough to draw conclusions.

Coming back to the interpretation problem of the sign change of the anomalous contribution, although not experimentally, there is one report concerning the anomalous hall effect in DMS in the hopping regime. A theoretical study [47], based on the anomalous hall-effect of p-type dilute magnetic semiconductors (GaMnAs) in the hopping regime, attributes a sign change of the anomalous hall coefficient when the Fermi-level crosses the density of states maximum in the impurity band. According to this model, the ordinary hall-contribution conserves the same sign everywhere in the impurity band, as temperature increases and impurity band filling changes. This behaviour is also observed in the present work, suggesting that a sign change of the AHE with constant sign of the OHE could be also realized. Burkov et al. derived a relation between anomalous and ordinary hall-conductivity, given by

$$\frac{\sigma_{ahe}}{\sigma_{ohe}} \propto \frac{dln\rho_0}{d\epsilon} \cdot (\frac{1}{T})^{1/4} \tag{4.16}$$

where ρ_0 is the zero-field resistivity and ϵ the density of states. This relation suggests that the anomalous hall contribution will decrease with $T^{1/4}$ in relation to the ordinary hall effect. If we consider that model, the strong decrease of the anomalous contribution in comparison to the ordinary part, as temperature rises, could be qualitatively understood. This dominating behaviour of the ordinary against the anomalous contribution with increasing temperature is evident in the 10-25K transition of sample AR 1R, depicted in Panel 3. The question is, in how far this model is applicable to the situation of Cu-doped ZnO. First of all, there is only one impurity band in GaMnAs, which is formed by the Mn-atoms, with a well-defined energy above the valence band. In the case of Cu-doped ZnO, at least two defect bands are present: one introduced through Cu-doping itself, and the other provided by donor defects. It could be shown that the transport mechanism is governed by variable-range hopping (Section 4.5.1), but the grade of localization of the electronic states, as well as the energy of the defect bands in the ZnO-bandgap, has just started to be studied. At present, there is only one model which deals with the anomalous hall effect in the hopping regime. With all this uncertainties, it would be definitely too early to apply the model described by [47] straight forward. However, it is of great interest to have a deeper look in the transport mechanism and the defect structure of the system with further experiments. This would help, in addition, to the creation of a consistent

picture which links charge transport and ferromagnetism.
Since it took time to optimize the process parameters of Cu-doped ZnO thin films to get conducting films and be able to observe this phenomena, the preparation of further sets of samples in this regime was not possible. In terms of anomalous hall effect, a clear evidence was just observed at one sample, and although there are facts and relations which confirm its validity, there are still phenomena which are not understood according to the present theories. Definitely, the standard characterization was not enough to be able to find a general picture which could explain the whole phenomenology; further studies are needed to be able to reproduce this results and to look deeper into what is really happening. A special issue of much concern is the sign change of the anomalous contribution. Further temperature dependent measurements (between 5 and 10K) will be needed to find and describe the suggested transition, as well as the evaluation of further samples in the low temperature regime. The other big question, is, undoubtly, why the anomalous component decreases so fast above 25K. The only fact, which presumably could have an influence on this effect, not considering the model of Burkov *et al.*, would be the observed quick decrease of the remanence at low temperatures in this sample, but still, the magnitudes are not consistent. Although not fully understood, there is experimental evidence of intrinsic magnetism in the Cu-doped ZnO system, supported by the magnetic characterization of the bulk samples (VSM) and the thin films through SQUID-magnetometry.

5. Summary and Outlook

In summary, Cu-doped ZnO bulk materials and thin films have been prepared under different conditions and characterized by the presented characterization methods. The polycrystalline bulk-materials have been prepared by solid-solid reaction, showing the absence of secondary phases and precipitates as well as evidence of ferromagnetism at room temperature. A deeper study has been done in the case of thin films, grown by the PLD-technique. The role of process parameters like substrate temperature, background gas and pressure, on the structural, magnetic and transport properties has been studied and discussed. An optimization of the process parameters lead to the realization of (0002)-oriented, conducting, transparent and ferromagnetic Cu-doped ZnO thin films. In the present work, three samples (AR 1, OX 3, AR 1R) were found to fulfill this criteria, having following common features:

- similar crystalline properties, conditioned through the moderate substrate temperatures used for growth (300 and 450°C), and the evidence of high mosaicity due to the substrate-film interface defects and columnar growth (Section 4.1)
- grown under oxygen-deficient conditions, factor which is crucial for increasing the conductivity (Section 4.5.1)
- a transport behaviour which is characteristic from Anderson-localized insulators (variable-range hopping) showing small changes in both carrier density and resistivity with increasing temperature
- a clearly stronger magnetic moment, e.g a magnetization signal which was strong enough to be distinguished from the ferromagnetic substrate background (SQUID-magnetometry- section 4.4)
- the largest MR-effect both at low and high temperatures (Section 4.5.2)
- electrons as majority carriers, with a carrier density of the order 10^{19}, which do not change much with temperature (no activation energy observed) and the observation of anomalous-Hall effect at low temperatures (Section 4.5.3)

According to the results, a clear evidence of ferromagnetism was found in the thin film samples, supported by anomalous Hall effect measurements. Unfortunately, the

anomalous hall-effect could not be evidenced at room-temperature within the measurement detection limit, although a magnetic moment was detected by SQUID-magnetometry. This discrepancy is one of the important issues to be outlooked, since the certainty to have room-temperature ferromagnetism in a system is absolutely necessary to think about possible technical applications. It should be mentioned, however, that no room-temperature anomalous hall effect was reported for any TM-doped ZnO material so far. The origin of ferromagnetism in Cu-doped ZnO is still unclear. From the phenomenological point of view, the Zener-model is not applicable. Assuming that the Cu 3d-states lie in the vicinity of the valence band of ZnO (as extracted from some ab-initio calculations [41, 40]) enabling a p-d hybridization, Cu-doped ZnO would be p-type conducting without the need of oxygen nonstochiometry. But the experiments did not deliver these results: the formation of a defect band was crucial for conduction. Therefore, the experimental results pointed towards the spin-split impurity band model postulated by Coey *et al*. However, a hybridization between the 3d-states of Cu and the impurity band is required to achieve high Curie-temperatures, according to this model. Since the Cu 3d-states are not shallow impurities, they must lie deep in the energy gap of ZnO. A possible hybridization could be considered, if the defect band and the Cu 3d-states lie energetically close to each other, deep in the gap. The only deep donor known up to now in ZnO, is the oxygen vacancy, so that only one possibility can be regarded as feasible: that the 3d-states of Cu lie in the vicinity of the defect level produced by oxygen vacancies, at around 1.0eV below the conduction band[16]. Taking as a reference the work of Chien et al.[42], who calculated energy gaps of Cu-doped ZnO close to 1.0eV, the hybridization seems indeed possible. The existance of a defect band has been confirmed by transport measurements, which recognized the hopping conduction within the band. Assuming that the Cu-level is not flat, forming an energy band, another question arises: why does not hopping conduction happens within the Cu-band in the oxygen-rich samples? As we can see, an important piece missing in the puzzle, is the experimental confirmation of the location of the Cu 3d-levels (and eventually the Cu-band width) in the studied samples. Optical measurements should be considered for this purpose. Another experiment which may provide useful information, is the codoping of the ferromagnetic ZnO:Cu samples with Al, since Al-doping will introduce a shallow impurity band which could even merge with the conduction band, producing a metal-insulator transition. In this case, the carrier transport will be shifted to the shallow region. The idea of the experiment is to see how the ferromagnetism develops, when the transport regime is far away from the Cu 3d-spin down states. If the samples are still ferromagnetic, the spin split impurity band model cannot be applied any more: the challenge will be to search for another possible source

of ferromagnetism.

As motivated in the introduction, to achieve ferromagnetic ordering in ZnO through Cu-doping, which is itself not ferromagnetic, is a good example to illustrate the intrinsic nature of a dilute magnetic semiconductor. In the field of DMS, the major sceptisism was due to the uncertainty, if the ferromagnetism comes from external sources like ferromagnetic clusters, segregates or secondary phases. According to this point of view, Cu-doped ZnO is an unambiguous DMS.

Since there are evidences, but still unsolved questions, this Diploma thesis should stimulate to carry further experiments on this unambiguous DMS, as well as related theoretical studies, to come a step closer to decipher the origin of ferromagnetism in dilute magnetic semiconductors.

Acknowledgments

First of all, i would like to thank Prof. Rudolf Gross, who gave me the oportunity to start the Diploma Thesis in this fabuolous research field, and the opportunity to interact with other research groups abroad, fact which was for me an invaluable experience. I learned a lot from his vast knowledge and i would like to thank him for the time he invested on our discussions.

I would like to thank Dr.Mathhias Opel and Dr.Sebastian Goennenwein, for their valuable advices, which gave me a better overview to find solutions and identify problems.

I wish to express my sincere gratitude to Karl-W. Nielsen, for his excellent guidance and supervision, and for his patience on teaching me the diverse experimental techniques. His critical comments and suggestions made me a more confident person. Without his help, i would not have been able to complete the thesis on time.

I am grateful to Petra Majewski and Andrea Boger, for their disposition, patience and help concering the magnetotransport measurements. I wish to thank also Sebastian Bauer for his help in critical situations.

For the time i was in Sweden, i want to express my sincere gratitude to Prof. K.V.Rao, who gave me constant support and freedom for doing innovative research. Under his guidance, i discovered my deep interest for science. I want to thank Dr. Lyuba Belova, Dr. Valter Stroem, Dr.Chandra Sudakar and Dr. Ziyan Gu for teaching me experimental techniques and for their help on any problem. I learned a lot from their expertise.

My sincere thanks are to Dr.Hong Tao Cao, Dr.Amita Gupta and Mukes Kapilashrmi for valuable discussions and for the team work during my time at the Royal Institute of Technology, and to all the TMFY-Group for the friendly atmosphere in- and outside the lab.

Last but not least, I want to dedicate this thesis to my parents, who invested a lot of efforts for my education, giving me the possiblity to go abroad to search for better opportunities. In spite of the long distance which divides us, their constant moral support and encouragement was always a motivation to complete the goal i started on my own, five years ago. „No hay palabras para agradecer lo que han hecho por mi, todo lo que soy es gracias a ustedes. Poner punto final a mi carrera es lo menos que puedo hacer para retribuir vuestros esfuerzos. Los amo.“

Bibliography

[1] H. Ohno. Making nonmagnetic semiconductors ferromagnetic. *Science*, 281:951–956, 1998.

[2] S. Das Sarma. *American Scientist*, 89(6):516, 2001.

[3] T. Dietl, H. Ohno, F. Matsukura, J. Cibert, and D. Ferrand. Zener model description of ferromagnetism in zinc-blende magnetic semiconductors. *Science*, 287:1019–1021.

[4] P. Sharma, A. Gupta, K.V. Rao, J.F. Owens, R. Sharma, R. Ahuja, J.M. Guillen, B. Johannson, and G.A. Gehring. Ferromagnetism above room-temperature in bulk and transparent thin films of mn-doped zinc-oxide. *Nature Materials*, 2:673, 2003.

[5] J.M.D. Coey, A. Douvalis, C.B. Fitzgerald, and M. Venkatesan. Ferromagnetism in fe-doped sno2 films. *Applied Physics Letters*, 84(10):1332–1334, 2004.

[6] S.Y. Wu. Synthesis, characterization and modeling of high-quality ferromagnetic cr-doped aln thin films. *Applied Physics Letters*, 82:3047–3049, 2003.

[7] S.J. Han. Magnetism in mn-doped zinc-oxide bulk samples prepared by solid-solid reaction. *Applied Physics Letters*, 83:920–922, 2003.

[8] P.V. Radovanovic and D.R. Gamelin. High-temperature ferromagnetism in ni-doped zinc-oxide aggregates prepared from coloidal diluted magnetic semiconductor quantum dots. *Physical Review Letters*, 91:157202, 2003.

[9] J. Philip, N. Thedoropolou, G. Berera, and J. Moodera. High-temperature ferromagnetism in manganese-doped indium-tin oxide films. *Applied Physics Letters*, 85:777–779, 2004.

[10] J.M.D. Coey, M. Venkatesan, and C.B. Fitzgerald. Donor impurity band exchange in dilute ferromagnetic oxides. *Nature Materials*, 4:173, 2005.

[11] K. Kopitzki. *Einfhrung in die Festkoerperphysik*. Teubner-Verlag, 2003.

[12] C. Kittel. *Solid State Physics*. Oldenbourg, 1999.

[13] B. Sapoval and C. Hermann. *Physics of Semiconductors*. Springer-Verlag, 1995.

[14] R. Gross and A. Marx. *Skript zu Spinelektronik*. 2005.

[15] D.P. Norton, Y.W. Heo, M.P. Ivill, S.J. Pearton, M.F. Chrisholm, and T. Steiner. Zinc-oxide: Growth, doping and processing. *Materials Today*, Review Feature:34, 2004.

[16] A.Janotti and C.Van de Walle. Oxygen vacancies in zinc-oxide. *Applied Physics Letters*, 87:122102, 2005.

[17] A. Tsukasaki, A. Ohtomo, T. Onuma, M. Ohtani, M. Sumiya, S. Fuke, Y. Segawa, H. Ohno, H. Koinuma, and M. Kawasaki. Repeated temperature modulation epitaxy for p-type doping and light-emitting diode based on zinc-oxide. *Nature Materials*, 4:42, 2005.

[18] P. Sharma, K. Sreenivas, and K.V. Rao. *Journal of Applied Physics*, 93:3963, 2003.

[19] H. Toyosaki, T. Fukumura, Y. Yamada, K. Nakajima, T. Chirykow, T. Hasegawa, Koinuma.H, and M. Kawasaki. Anomalous hall-effect governed by electron doping in a room-temperature transparent ferromagnetic semiconductor. *Nature Materials*, 3:221, 2004.

[20] J. He, S. Xu, and I. Takeuchi. Room temperature ferromagnetic n-type semiconductor in $(in_{1-x}fe_x)_2o_{3-\sigma}$). *Applied Physics Letters*, 86:052503, 2005.

[21] M. Opel. *Magnetismus*. Skipt zur Vorlesung WS 2004/2005.

[22] Amita Gupta. *Doctoral Thesis*. Royal Institute of Technology (KTH), Stockholm,Sweden, 2004.

[23] W. Buckel. *Supraleitung*. Springer, 1996.

[24] S. Choopun, R.D. Vispute, W. Noch, A. Balsamo, R.P Sharma, and T. Venkatesan. Oxygen pressure-tuned epitaxy and optoelectronic properties of laser-deposited zinc-oxide films on sapphire. *Applied Physics Letters*, 75:25, 1999.

[25] Y. Chen, D.M. Bagnall, H. Koh, K. Park, K. Hiraga, Z. Zhu, and T. Yao. Plasma asisted molecular beam epitaxy of zno on c-plane sapphire: Growth and characterization. *Journal of Applied Physics*, 84(7):3912–3918, 1998.

[26] M. Diaconu, H. Schmidt, H. Hochmuth, M. Lorenz, G. Benndorf, D. Spemann, A. Setzer, P. Esquinazi, A. Pppl, H. von Wenckstern, K.-W. Nielsen, R. Gross, H. Schmid, W. Mader, G. Wagner, and M. Grundmann. Room-temperature ferromagnetic mn-alloyed zinc-oxide films obtained by pulsed laser deposition. *submitted to Elsevier Science*, 2005.

[27] T. Wakano, N. Fujimura, Y. Morinaga, N. Abe, A. Ashida, and T. Ito. Magnetic and magneto-transport properties of zno:ni films. *Physica E*, 10:260–264, 2001.

[28] S. Kishimoto, T. Yamamoto, Y. Nakagawa, K. Ikeda, H Makino, and T. Yamada. Dependence of electrical and structural properties on film thickness of undoped zinc-oxide thin films prepared by plasma-asisted electron beam deposition. *Superlattices and Microstructures*, 39:306–313, 2006.

[29] X.B. Wang, D.M. Li, F. Zeng, and F. Pan. Microstructure and properties of cu-doped zinc-oxide films prepared by dc reactive magnetron sputtering. *J.Phys.D:Appl.Phys.*, 38:4104–4108, 2005.

[30] A Hartmann, M.K. Puchert, and R.N. Lamb. Influence of copper dopants on the resistivity of zinc-oxide films. *Surface and Interface Analysis*, 24:671–674, 1996.

[31] D.C. Look, J.W. Hemsky, and J.R. Sizelove. Residual native shallow donor in zinc-oxide. *Physical Review Letters*, 82(12):2552, 1999.

[32] A. Tiwari, C. Jin, J. Narayan, and M. Park. Electrical transport in $zno_{1-\delta}$ films: Transition from band-gap insulator to anderson localized insulator. *Journal of Applied Physics*, 96(7):3827–3830, 2004.

[33] S. Lee, H.S. Lee, S.J. Hwang, Y. Shon, Y.K. Deuk, and E.K. Kim. Effects of oxygen partial pressure during sputtering growth on physical properties of $zno_{0.93}mn_{0.07}o$ thin films. *Journal of Crystal Growth*, 286:223–227, 2006.

[34] R. Resta. Why are insulators insulating and metals conducting. *Europhysics News*, 34:3, 2003.

[35] O. Madelung. *Festkoerpertheorie III - Lokalisierte Zustaende*. Springer-Verlag, 1973.

[36] C.F. Klingshirn. *Semiconductor Optics*. Springer-Verlag, 1995.

[37] K.C Beverly, J.F. Sampaio, and J.R. Heath. Effects of size dispersion disorder on the charge transport in self-assembled 2d-silver nanoparticle arrays. *J.Phys.Chem.B*, 106:2131–2135, 2002.

[38] P.W. Anderson. Absence of diffusion in certain random lattices. *Physical Review*, 109(5):1492, 1958.

[39] X. Feng. Electronic structures and ferromagnetism of cu- and mn-doped zinc-oxide. *J.Phys:Condensed Matters*, 16:4251–4259, 2004.

[40] L.H. Ye, A.J. Freeman, and B. Delley. Half metallic ferromagnetism in cu-doped zno: Density functional calculations. *Physical Review B.*, 73:033203, 2006.

[41] L. Huang, A. Gupta, F.J. Owens, A. Rosa, R. Ahuja, and K.V. Rao. Experimental and theoretical evidence for unusual room temperature ferromagnetism in cu-doped zno semiconductor. *submitted to Physical Review Letters*, 2006.

[42] C. Chien, S. Chiou, G.Y. Guo, and Y.D. Yao. Electronic structure and magnetic moments of 3d transition metal-doped zinc-oxide. *Journal of Magnetism and Magnetic Materials*, 282:275–278, 2004.

[43] T. Andrearczyck, J. Jaroszynski, G. Grabecki, T. Dietl, T. Fukumura, and M. Kawasaki. Spin-related magnetoresistance of n-type zno:al and $zn_{1-x}mn_x$o:al thin films. *Physical Review B.*, 72:121309, 2005.

[44] F. Reuss, C. Frank, C. Kirchner, R. Kling, and T. Gruber. Magnetoresistance in epitaxially grown degenerate zinc-oxide thin films. *Applied Physics Letters*, 87:112204, 2005.

[45] R.P. Khosla and J.R. Fischer. *Physical Review B.*, 2:4804, 1970.

[46] A. Vaknin, A. Frydman, Z. Ovadyahu, and M. Pollak. High-field magnetoconductance in anderson-insulators. *Physical Review B.*, 54(19):13604, 1996.

[47] A.A. Burkov and L. Balents. Anomalous hall effect in ferromagnetic semiconductors in the hopping transport regime. *Physical Review Letters*, 91(5):057202–1, 2003.